# DISSIPATION AND NONLINEAR MECHANICS IN ULTRAHIGH QUALITY FACTOR MEMBRANE RESONATORS

A Dissertation

Presented to the Faculty of the Graduate School

of Cornell University

in Partial Fulfillment of the Requirements for the Degree of

Doctor of Philosophy

by

Srivatsan Chakram Sundar

January 2015

© 2015 Srivatsan Chakram Sundar

ALL RIGHTS RESERVED

DISSIPATION AND NONLINEAR MECHANICS IN ULTRAHIGH QUALITY FACTOR MEMBRANE RESONATORS

Srivatsan Chakram Sundar, Ph.D.

Cornell University 2015

The quantum control of mechanical resonators requires the realization of exceptionally low dissipation in conjunction with strong nonlinear interactions. In this thesis, we demonstrate the simultaneous realization of both these features in ultrahigh quality factor silicon nitride membrane resonators, a promising new optomechanical platform in the emerging field of cavity optomechanics.

The mechanical properties of the silicon nitride resonators are studied through a combination of spectroscopic and interferometric imaging techniques. We demonstrate ultrahigh quality factors of $5 \times 10^7$ and frequency-quality factor products of $1 \times 10^{14}$ Hz corresponding to the largest values yet reported for mesoscopic membrane resonators, and an order of magnitude larger than what is required for room temperature quantum control. We perform a study of the limiting dissipation mechanisms as a function of resonator and substrate geometries and identify radiation loss through the supporting substrate as the dominant loss process. We proceed to alleviate radiation loss through the engineering of substrates with phononic bandgaps and present preliminary demonstrations of increased quality factors for a wide range of membrane modes.

We also realize a two-mode parametric nonlinear process, and use it to demonstrate nondegenerate mechanical parametric amplification and two-mode thermomechanical noise squeezing. The observed phenomena show excellent agreement, over five orders of magnitude in displacement, with a two-mode model with the parametric

coupling between the modes mediated by an excitation of the supporting substrate platform. The realization of a strong nonlinear interaction in a mechanical platform that is compatible with optomechanical cooling, room temperature quantum control and quantum limited detection is an important step towards the realization of non-classical mechanical states, the observation of entanglement between macroscopic mechanical degrees of freedom and quantum enhanced metrology.

The last chapter of this thesis is unrelated to the rest of the work presented in it. This chapter discusses the coupling between the underlying elastic medium and electronic nematic order in high temperature cuprate superconductors and suggests the use of acoustic phonons as a probe of nematic order.

[1] Dissipation in Ultrahigh Quality Factor SiN Membrane Resonators,
S. Chakram, Y.S. Patil, L. Chang, and M. Vengalattore, Phys. Rev. Lett. 112, 127201, (2014).

[2] Thermomechanical two-mode squeezing in an ultrahigh Q membrane resonator,
Y. S. Patil, S. Chakram, L. Chang and M. Vengalattore, arXiv:1410.7109, (2014).

[3] Multimode phononic correlations in a nondegenerate parametric amplifier,
S. Chakram, Y. S. Patil, M. Vengalattore, arXiv:1412.8536, (2014).

[4] Nondestructive imaging of an ultracold lattice gas,
Y. S. Patil, S. Chakram, L. M. Aycock, and M. Vengalattore, Phys. Rev. A 90, 033422, (2014).

[5] Quantum Control by Imaging : The Zeno effect in an ultracold lattice gas,
Y. S. Patil, S. Chakram, M. Vengalattore, arXiv:1411.2678, (2014).

## BIOGRAPHICAL SKETCH

Srivatsan grew up in the town of Kalpakkam in Tamil Nadu, India, a small coastal town in south eastern India, famous for its nuclear reactors and a pristine beach. His parents, Bharathi and Sundar, both physicists, encouraged and inculcated a love for the sciences, physics in particular, from an early age and allowed him the freedom to pursue his dreams. He has fond memories of studying mathematics and the sciences with his high school friends, Aneesh, Chinni, Janani and their favorite Murthy uncle, in the pristine environs of Kalpakkam. On completing his schooling, he went on to obtain an undergraduate degree in physics at the Indian Institute of Technology, Kanpur. He has been a graduate student at Cornell since 2006 and a member of the Vengalattore group since 2010.

To

My Family

## ACKNOWLEDGEMENTS

This thesis has come together with the help and support of numerous people. First and foremost, I thank Mukund Vengalattore for allowing me the unique opportunity of being a first generation student in an ultracold atom lab. I have learnt more from him than any one person on this planet. The range of things he has patiently taught me covers atomic physics, building experiments, electronics, machining, data analysis and presentation, not to mention soccer and tennis skills. His work ethic, passion for physics, his ambition and originality, have been inspirational.

I am lucky to have come to know the many other gifted people who have been part of the Vengalattore group over the past years. I particularly thank Yogesh Patil and Laura Chang, my colleagues in the mechanical resonator studies, which constitutes the bulk of the work described in this thesis. The work that is described in this thesis is as much theirs as mine. I thank Harry Cheung, Airlia Schaffer, Chandler Kemp, Eli Fox, Scott Flanz, John Lombard, Sam Roland, Shannon Harvey, Collin Reynolds, Lauren Aycock, Amulya Bhagat, Ben Nosarzewski, Seong-Oh and Ivaylo Madjarov for their help at various times, over the last four years and the comic relief that they have provided.

Prior to joining the Vengalattore group, I was lucky to have had the opportunity to work with Eun-Ah Kim, Michael Lawler and Chris Henley. I thank them for exposing me to theoretical condensed matter physics and adding to the richness of my research experience at Cornell. I thank Eun-Ah and Michael for letting me include the work I did with them as part of this thesis, and for their help at various times.

I particularly thank Erich Mueller for all that I have learnt from him over the years, through his courses and group meetings, for always having the time to answer questions and for first sparking my interest in the beautiful field of ultracold

atoms.

My switch to cold atom research group would have also not happened without numerous discussions with Kaden Hazzard, Stefan Baur and Stefan Natu. I thank them for their infectious enthusiasm for physics and for all that they have taught me, including how to maintain an office space.

I thank Dan Ralph for being part of my Ph.D. committee, and for an excellent solid state physics course, one of my first classes at Cornell.

I thank Deb Hatfield, Kacey Acquilano and all the people in the physics office for being so incredibly helpful, during pressing times. Many thanks are due to Nate Ellis for advice on machining and on life.

I thank my friends in Ithaca, Justin Vines, Ben Machta, Phil Kidd, Vikram Gadagkar, Praveen Gautham, Levon and Gaia Azizyan, Anisse Dobson, Daniel Kolbin, Saugata Mohapatra, Yoav Kallus, Alisa Blinova, Sumiran Pujari, Rajendran Narayanan, Saikat Ghosh, Sharvari Nadkarni, Madhusushan Venkadesan, Soumya James, the list goes on, without whom my life over the last nine years would have been far less interesting and fulfilling.

I thank fellow Kanpuriyas, for shaping the way I think and making me the person I am. They are far too numerous to list, but particular thanks are due to Amar, Archis, Tom, Subhojoy, Sid, Saksham, Avinash and Aman.

Lastly I thank my parents, my brother Deepak and my aunt Jayanthi, for their constant encouragement and support.

## TABLE OF CONTENTS

## LIST OF FIGURES

CHAPTER 1

# QUANTUM CONTROL OF ULTRAHIGH Q MECHANICAL RESONATORS

Decades ago, pioneering interferometric experiments performed by Braginsky[1], resulted in the coming together of a highly influential group of scientists with the goal to realize an ambitious aim, the direct detection of gravitational waves, as postulated by Einstein. This collaborative effort, now known as LIGO, attempted to realize a great challenge, requiring a displacement sensitivity of $10^{-21}\mathrm{m}/\sqrt{\mathrm{Hz}}$. Undeterred by this, these scientists went ahead to do precisely that. As has always been the case, the goal of realizing precise measurements not only resulted in new technologies, it also led to progress in fundamental physics. One of the first realizations that came out of this was, that quantum mechanics can have an influence on the dynamics of massive objects, captured succinctly by Carlton Caves in [2]:

*" The interferometers now being developed to detect gravitational waves work by measuring small changes in the positions of free masses. There has been a controversy whether quantum-mechanical radiation-pressure fluctuations disturb this measurement. This Letter resolves the controversy: They do. "*

The ensuing developments have brought together a wide spectrum of physicists in optics, atomic physics, material science and engineering, culminating in the birth of the emerging field of cavity optomechanics[3]. Cavity optomechanics studies the influence of electromagnetic radiation on mechanical objects, using it to probe, detect and control mechanical motion. Building upon an effort to control, trap, manipulate and probe atomic systems, recent years have seen rapid progress in this field, culminating in the use of the radiation pressure from light, in conjunction with cryogenic cooling, to realize mesoscopic mechanical resonators in the quan-

tum ground state of vibration[4][5]. Along with an earlier realization of ground state cooling purely through conventional cryogenics[6], this has set the stage for addressing fundamental questions regarding the classical to quantum divide[7], enabling quantum enhanced metrology and promising a rich bounty of technological advances, such as improved global positioning systems.

Notwithstanding this success, cavity optomechanics is faced with extreme technological challenges, the foremost among them being the issue of dissipation. Mechanical systems, unlike pristine atomic systems, are plagued by this issue. This is a challenging problem, arising from the fact that its study involves many different systems and many disparate mechanisms. The preparation of a mechanical system in a quantum state and the observation of quantum effects in a mechanical degree of freedom require overcoming the deleterious effect of thermal decoherence. Thermal decoherence can be overcome either by reducing the temperature of the ambient bath or by reducing the coupling between the mechanical degree of freedom and the environment. Observing quantum effects in a mechanical degree of freedom, at room temperature, requires exceptionally low dissipation. As a result, ground state cooling[4][5][6] of mechanical degrees of freedom has to date only been demonstrated in conjunction with cryogenic cooling to reduce the thermal coupling to the environment.

Additionally, the high degree of isolation required for cooling a mechanical system to the quantum regime, typically precludes the presence of strong nonlinear interactions involving the mechanical degree of freedom, necessary for the creation of interesting quantum states and essential for the manipulation of the engineered states. Therefore, while the mechanical degrees of freedom must be isolated from sources of dissipation, it must also be possible for there to be strong coherent

interactions, either between distinct mechanical degrees of freedom or between the mechanical degrees of freedom and other auxiliary quantum systems, such as atomic systems.

This thesis describes the realization of an optomechanical platform that addresses both these issues. Chapter 2 of this thesis describes the realization of silicon nitride membrane resonators with the lowest dissipation measured to date, with quality factors of $50\times10^6$ and $f\times Q$ products approaching $10^{14}$ Hz[8] and dissipation that is an order of magnitude lower than that required for room temperature quantum control of the mechanical resonator. This along with the low optical absorption of silicon nitride[9] results in the realization of an optomechanical platform that is compatible with ground state cooling, room temperature quantum control and quantum limited detection when integrated with a Fabry-Perot Cavity[10]. We perform studies of a host of limiting dissipation mechanisms in these membrane resonators, identifying radiation loss from the resonator to the surrounding substrate[11] as the dominant source of loss for a wide range of membrane parameters, pointing the way towards further decrease in the dissipation through the engineering of substrates with a phononic bandgap that prevent energy loss into the surrounding substrate. In Chapter 3, we proceed to engineer resonators on bandgapped substrate and present preliminary demonstrations of reduced radiation loss, through increased quality factors for a wide range of membrane modes.

Chapters 4 through 5 of this thesis address the second issue, regarding strong nonlinear interactions. We demonstrate a form of reservoir engineering[12] through an excitation of the supporting substrate platform to realize a strong two-mode parametric nonlinearity between distinct modes of the membrane resonator. We demonstrate an understanding of this nonlinear interaction through a two-mode

model that accurately captures the observed phenomena over five orders of magnitude in displacement. We demonstrate the use of this nonlinearity for mechanical parametric amplification and two-mode thermomechanical noise squeezing[13].

We have thereby realized an optomechanical platform that simultaneously preserves the high degree of isolation required for ground state cooling and room temperature quantum control and also simultaneously possesses the strong nonlinearities that are required for the useful manipulation of quantum states of the mechanical degrees of freedom.

CHAPTER 2

# DISSIPATION IN ULTRAHIGH QUALITY FACTOR SILICON NITRIDE MEMBRANE RESONATORS

## 2.1 Introduction

Among the primary tasks of optomechanics are the preparation of one or more modes of a mechanical resonator in a well-defined quantum state, coherent manipulation of the engineered state, and quantum-limited measurements of the displacement or the energy. Typically, this is done by coupling the mechanical resonator to the electromagnetic field either at optical or at microwave frequencies, by placing the resonator in an optical cavity. This results in both optomechanical cooling[14, 15] of the mechanical modes of interest, and quantum-limited measurement and control of their motion.

The inevitable coupling to the surrounding bath results in an open system, with the coherent coupling always competing with thermal decoherence. This results in stringent constraints on the mechanical properties of the resonator. For observing quantum coherent effects, the lifetime of a single phonon must exceed the time scale for coherent dynamics, which is set by the mechanical oscillation frequency. This translates to the condition that the frequency-quality factor product exceed $k_B T/h$ for the mechanical mode of interest[3]. The observation of quantum coherent behavior in a mechanical resonator coupled to a room temperature bath therefore requires frequency-quality factor products exceeding $k_B T/h = 6 \times 10^{12}$ Hz ($T = 300$ K). For this reason, and for a host of other applications such as in sensing, communication and precision measurements, there has been a flurry of

research in producing resonators of higher quality and in the study of their limiting dissipation mechanisms.

Stressed silicon nitride (SiN) membranes and strings have in recent years been shown to have remarkable mechanical properties[16][17] with recent demonstrations of $f \times Q$ products of $2 \times 10^{13}$ Hz at room temperature in commercial high stress silicon nitride membrane resonators[17]. In addition they have favorable optical properties[9] with an extremely low optical absorption (less than a part in $10^6$) in the near infrared. Since the pioneering experiment of Thompson et al[10], who showed how such membranes could be coupled efficiently to an optical mode of a Fabry-Perot Cavity using the so-called membrane-in-the-middle approach, SiN membranes have become one of the most promising platforms in optomechanics.

When our group embarked on its program for optomechanics, one of the first steps was to realize high Q resonators, building on the work previously described. As a preliminary study, we first reproduced the previously reported results for quality factors of commercial high stress stoichiometric silicon nitride membrane resonators, in the process understanding key elements of the experimental procedure such as the handling of the resonators and appropriate clamping mechanisms. This led us to embark on a systematic study of quality factors of resonators of different geometries, i.e., different widths and thicknesses, with heuristics pointing towards measurements on resonators with larger aspect ratios. This resulted in the realization of resonators with peak quality factors of $5 \times 10^7$ and a frequency-Q product approaching $1 \times 10^{14}$ Hz, the highest quality factors reported to date for membrane resonators at room temperature, which are an order of magnitude larger than what is required for room temperature quantum control.

The exceptionally high quality factors measured, and the quest for even higher quality factors necessitated an understanding of the limiting dissipation mechanisms in these resonators.

This chapter is organized as follows. We start with a description of the mechanical resonator in Sec.[2.2], followed by a description of our apparatus and the optical setup for membrane motion detection in Sec.[2.3]. Sec.[2.4] provides a description of our method for interferometric imaging of membrane motion. In Sec.[2.5], we present the results of our measurements of the mechanical properties of these membranes, particularly the dissipation, characterized by the quality factors of the resonator modes. This is followed by an overview of the dissipation mechanisms in these systems as given in Sec.[2.6] and an analysis of each of their roles in explaining the measured quality factors in the sections that follow. The contents of this chapter are an elaboration of [8].

## 2.2 Mechanical description of silicon nitride membrane resonators

The SiN membranes that are studied in this work are suspended on a square window etched on a silicon substrate (chip). The membrane sizes range from 0.5 - 5 mm and their thicknesses range from 30 - 200 nm. The silicon substrate width ranges from 5 - 10 mm with thicknesses ranging from 200 - 500 $\mu m$. All the silicon nitride membrane resonators that we study are fabricated by NORCADA inc., a Canadian MEMS company which produces these membranes for their use as transmission electron microscopy windows.

The SiN membrane is grown on the silicon substrate through a low pressure chemical vapor deposition (LPCVD) process. This results in silicon nitride membranes that are highly stressed with an intrinsic stress of $\approx$ 900 MPa [18].

A stressed two dimensional membrane is described by the following equation of motion[19],

$$D\left(\frac{\partial^2}{\partial x^2}+\frac{\partial^2}{\partial y^2}\right)^2 w-\sigma h\left(\frac{\partial^2 w}{\partial x^2}+\frac{\partial^2 w}{\partial y^2}\right)=-\rho h\frac{\partial^2 w}{\partial t^2} \tag{2.1}$$

where in the above, $w(x,y)$ gives the z displacement of the membrane as a function of location on the membrane, $\sigma$ = 900 MPa is the intrinsic tensile stress, $\rho$ = 2.7 g/cm$^3$ is the mass density of silicon nitride. D is the flexural rigidity of the membrane, which is related to the Young's modulus ($E$), the thickness ($h$) and the Poisson ratio ($\nu_p$) via the expression $D=\frac{Eh^3}{12(1-\nu_p^2)}$. In the absence of tensile stress, this equation describes the vibrations of a plate. The relative strength of the flexural rigidity in comparison with the intrinsic tensile stress is parametrized by $\epsilon=\frac{D}{\sigma h L^2}$, where $L$ is the lateral dimension of the membrane. $\epsilon$ ranges from $10^{-7}$ - $10^{-10}$ for the membranes studied. The mechanical eigenfrequencies of the membrane are hence well approximated by that of a stressed membrane with no

flexural rigidity, i.e.,

$$\nu_{mn} = \sqrt{\frac{\sigma}{4\rho L^2}}\sqrt{m^2+n^2} \tag{2.2}$$

where $m$ and $n$ describe the number of antinodes along the $x$ and $y$ directions. A characteristic plot of the eigenfrequencies of the membrane as a function of $\sqrt{m^2+n^2}$ shown in Fig.[2.1] demonstrates the validity of the above expression for these membranes.

The motion of a single mode of the membrane can be characterized by a time de-

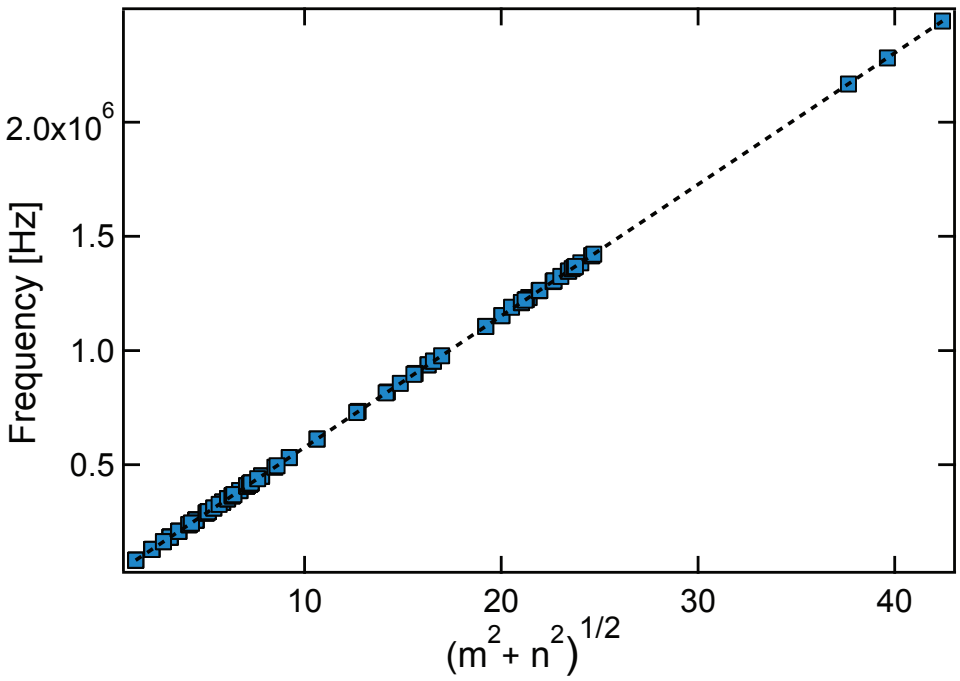


Figure 2.1: Frequency of the modes of a membrane ($L = 5$ mm; $h = 100$ nm) as a function of $\sqrt{m^2+n^2}$. The fit to the line provides a slope of $57569 \pm 5$ Hz. Therefore the phase velocity of the membrane is $c_R = \sqrt{\frac{\sigma}{\rho}} = 565.69 \pm 0.05\ m/s$. Assuming $\rho = 2.7\ g/cm^3$ results in a tension of $\sigma = 895$ MPa.

pendent amplitude $z(t)$. The displacement of each point of the membrane is related to the eigenmode $u_n(x,y)$, and the amplitude $z(t)$ via $w(x,y,t) = u_n(x,y)z(t)$. This effective coordinate $z(t)$ satisfies the equation for a damped harmonic oscil-

lator:

$$m_{eff}\frac{d^2z}{dt^2} + \Gamma_m m_{eff}\frac{dz}{dt} + m_{eff}\omega_n^2 z = F_{ext}(t) \tag{2.3}$$

where $\Gamma_{eff}$ is the decay rate of the membrane mode and $m_{eff}$ is the effective mass of the membrane which is related to the physical mass of the membrane as $m_{eff} = \frac{m}{4}$. This is obtained by equating the potential energy of the membrane to that of the single harmonic oscillator[20]. In the above $z(t)$ is the antinodal displacement. If $z(t)$ is instead the displacement as read out by a laser beam with a finite waist incident at an arbitrary point on the membrane, the effective mass is larger than $\frac{m}{4}$.

The transient solution of the equation for a damped harmonic oscillator is given by

$$z(t) = Ae^{-\frac{\Gamma_m t}{2}}\cos(\omega_n' t + \phi) \tag{2.4}$$

with $\omega_n' = \sqrt{\omega_n^2 - \frac{\Gamma_m^2}{4}}$. The driven response of the oscillator to a harmonic force given by $f(t) = |f(\omega)|e^{i\omega t}$ is given by $A(\omega)e^{i\omega t}$ where the response amplitude and phase are in turn given by

$$\begin{aligned} |A(\omega)| &= \frac{|F(\omega)|}{m_{eff}(\sqrt{(\omega^2-\omega_0^2)^2 + \Gamma_m^2\omega^2})} \\ \cot\phi(\omega) &= \frac{\Gamma_m\omega}{\omega_0^2 - \omega^2} \end{aligned}$$

The quality factor of the resonance is the ratio of the energy stored in the resonator ($E$) to the energy lost by the resonator per period $\Delta E$, i.e.,

$$Q = \frac{2\pi E}{\Delta E} = \frac{\omega E}{\dot{E}} = \frac{\omega_m}{\Gamma_m} \tag{2.5}$$

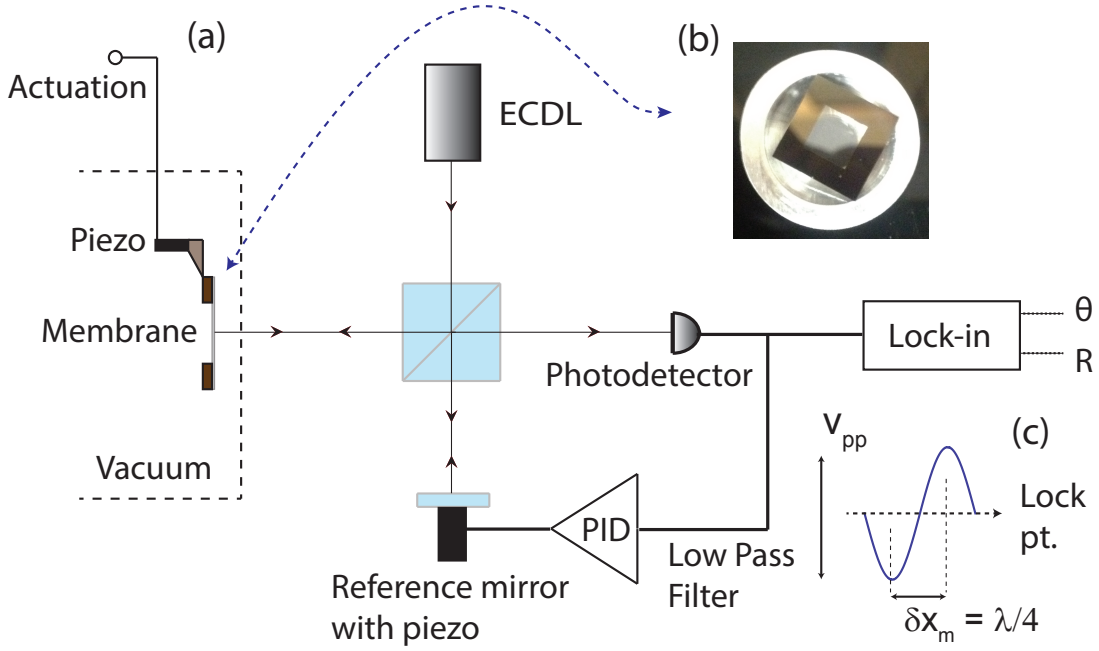


Figure 2.2: (a) Schematic of Michelson interferometer setup for detection of membrane motion. The interferometer is locked to the side of the interference fringe (see (c)) using a home built lock circuit. (b) The mounting scheme: substrate is mounted on an aluminum chuck with a dab of torr-seal on one corner with the substrate making contact with the aluminum chuck atmost at 3 corners. (c) A schematic of the interference fringe obtained by moving the reference piezo with the arrow indicating the side of the fringe, where the interferometer is locked.

## 2.3 Apparatus for membrane characterization

To handle and characterize the resonator, the silicon substrate is mounted on an aluminum chuck $\sim$ 1.5 cm in diameter, using a small dab of torr-seal on one corner, with the substrate making contact with the aluminum chuck at two to three corners (Fig.[2.2(b)]). This aluminum chuck screws into a second cylindrical aluminum piece with a slot,which is glued on to a ring piezo (PhysicsInstrumente (P-010.00H), Travel: 5 $\mu m$/1000V ; Resonance frequency: 144 kHz), mounted on

a cylindrical piece of copper. The entire setup screws into a standard lens mount which is mounted on a copper feed through and vibrationally isolated using a set of viton rings. The system goes inside a vacuum chamber which is pumped down to a pressure of $2 \times 10^{-7}$ torr using a roughing and a turbo pump, followed by an ion pump (Varian: 18 l/s). The membrane properties are characterized with the turbo pump switched off, in order not to be affected by the resulting vibrations.

The mechanical properties of the membrane are characterized by using the membrane as one arm of an actively stabilized Michelson interferometer (Fig.[2.2(a)]) using a home built external cavity diode laser (ECDL) operating at $\approx$ 795 nm. The reference arm of the interferometer has a mirror mounted on a low voltage piezo. A low pass filtered output of the photodetector is input to a feedback circuit, that actively stabilizes the interferometer to the side of the interference fringe (Fig.[2.2(c)]). The displacement of the membrane is imprinted in the light and measured using the unfiltered photodetector output using either a lockin-amplifier or a spectrum analyzer. A change in the total path length by $\frac{\lambda}{2}$ results in a change in the photodetector voltage by $V_{pp}$. When the interferometer is locked to the side of the fringe, the displacement of the membrane is related to the measured voltage through the expression,

$$\delta x = \frac{V_{sig}}{V_{pp}} \left( \frac{\lambda}{2\pi} \right) \tag{2.6}$$

The lengths of the two arms of the interferometer are matched in order to reduce the effect of phase noise. A focusing lens is placed before the membrane in order to obtain as small a spot size as possible. A large spot size results in lower signal to noise arising from the larger effective mass. Additionally, it results in detection nonlinearities. For instance, a spurious signal is seen at twice the frequency of oscillation of a driven membrane mode, when the spot size is comparable to the

wavelength of the membrane mode. The size of the spot after focusing is estimated to be $\sim 100\mu m$. This realizes a position measurement with a sensitivity of $\sim 0.03$ pm/$\sqrt{\text{Hz}}$ with powers of 200 $\mu$W incident on the membrane.

## 2.4 Dark ground imaging of mechanical motion

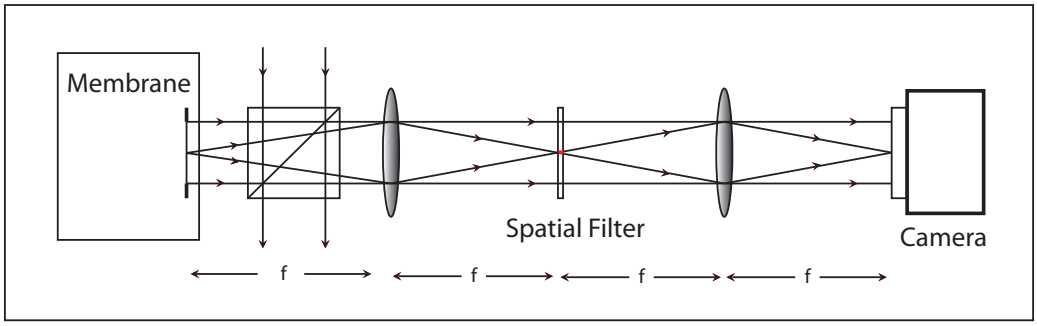


Figure 2.3: Schematic for dark-ground imaging of membrane motion. A dark spot in the Fourier plane of the first lens blocks the spatial DC background.

In addition to standard displacement measurements through a small focused beam incident on the membrane, we also implement interferometric imaging of the membrane motion. In addition to providing clues regarding the limiting dissipation mechanisms in these resonators, this technique allows for optical addressability of resonator modes of one's choosing and is a powerful tool for studies of multimode optomechanics[21].

The schematic for obtaining the interferometric images is shown in Fig.[2.3]. The setup consists of two identical lenses spaced apart by twice their focal length, with the membrane at the focus of the first lens and the camera at the focus of the

second. A small dark spot is placed in between the two lenses, in the Fourier plane of the first lens. The light reflected off of the membrane consists of a part that is directly reflected, i.e., with a well defined wavevector along the axis of the incident beam, and a part that is scattered. The information about the membrane motion is contained in the scattered light. The signal is obtained by the interference from the scattered light and light that is directly reflected. The light that is directly reflected results in a background that drowns out the signal resulting from the membrane motion. The dark spot ($\sim 200\ \mu m$) blocks out this (spatial DC) background component thereby increasing the signal to noise.

The signal detected on the camera is proportional to the square of the amplitude of the membrane motion. This can be easily seen as follows. If the reflected light from the membrane is given by $E(x,y) = E_0 e^{i\phi(x,y)}$, where $\phi(x,y)$ is the phase accrued from the motion of the membrane. This phase is related to the displacement $\delta z(x,y)$ of the membrane via $\phi(x,y) = \frac{4\pi}{\lambda}\delta z(x,y)$. The dark spot blocks the spatial DC component of the light and the intensity of the light on the camera $I(x,y)$ is therefore given by,

$$\begin{aligned} I(x,y) &= E_0^2 |(e^{i\phi(x,y)} - 1)|^2 \\ &\approx I_0 \phi(x,y)^2 \\ &= I_0 \frac{16\pi^2}{\lambda^2} \delta z(x,y)^2 \end{aligned}$$

Fig.[2.4] shows images of membrane motion acquired through such a method using an incident beam with a waist of 3.5 mm and $\sim 10\mu W$ of power and 3 ms of camera exposure. The intensity of the light being the square of the membrane displacement is reflected in neighbouring antinodes being bright. This imaging scheme is therefore not sensitive to the phase of the membrane vibration.

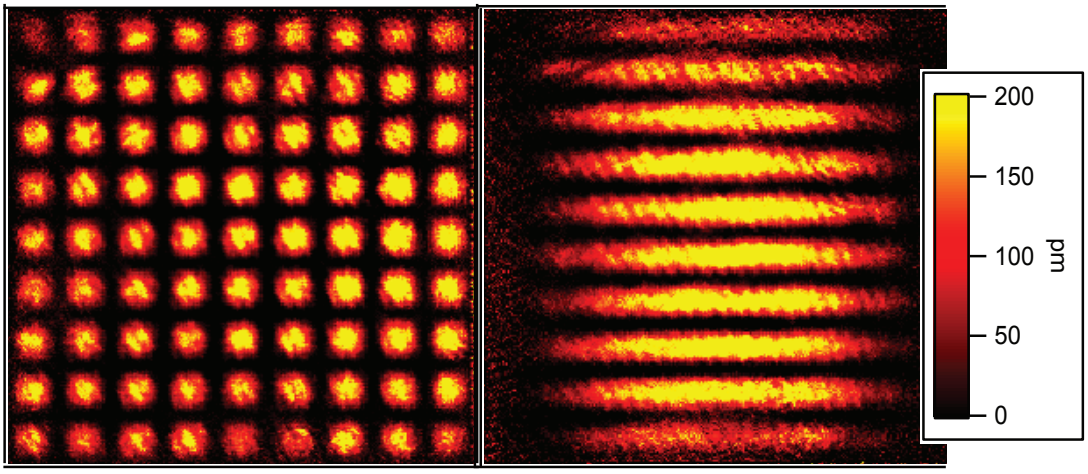


Figure 2.4: Interferometric imaging of the mechanical modes: in situ images of the (left) (9,9) mode and (right) (1,10) mode of the membrane. Neighbouring antinodes are bright, indicating insenstivity of imaging scheme to the phase of vibration.

## 2.5 Quality factor measurements

We first identify the frequencies of the resonator modes by monitoring the photodiode output on a spectrum analyzer and identifying either the thermal motion peaks or by identifying the response frequencies through piezo actuation of the membrane. We know where the resonances are expected to be based on the membrane dimensions and the approximate stress. Once the fundamental mode frequency is identified, it is easy to identify the other mode frequencies because of the excellent agreement between the resonance frequencies with Eqn.[2.2] (See Fig.[2.1]).

The dissipation is characterized through ring down measurements of the oscillation (see Fig.[2.5](left)). The membrane is piezo actuated for periods upto 10 ms, resulting in the excitation of the membrane to amplitudes ranging from 10-1000 pm, after which the drive is switched off and the decay in amplitude measured

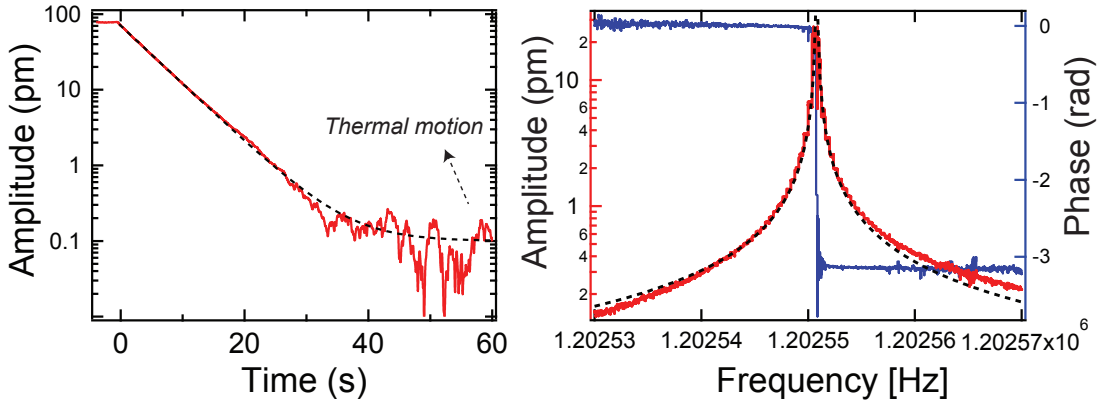


Figure 2.5: (Left) Ringdown curve corresponding to $\tau = 5.63$ s, $\nu = 1202.553$ kHz and $Q = 21.3 \times 10^6$, $\Gamma = 56$ mHz. (Right) Amplitude (red) and phase (blue) response to a sweep of the piezo drive frequency. The dashed black curve is the driven response of a harmonic oscillator with a linewidth of 60 mHz.

using a lock-in amplifier, with the decay fit to an exponential to extract the fall time $\tau$. The quality factor is then calculated using the expression $Q = \pi\nu\tau$, where $\nu$ is the frequency of the mode in question. The quality factors measured are as high as $50 \times 10^6$. The exceptionally high quality factors measured, necessitated a careful study of systematic errors that might affect the measurements.

### 2.5.1 Validating the Q-factor measurements

We performed various checks to ensure the validity of our quality factor measurements. These include:

(1) The negligible effect of radiation pressure and heating due to the laser field on the mechanical motion. We found no change in quality factor for a change in the intensity of incident light by an order of magnitude.

(2) The linearity of the drive. Changes in the peak amplitude by up to a factor

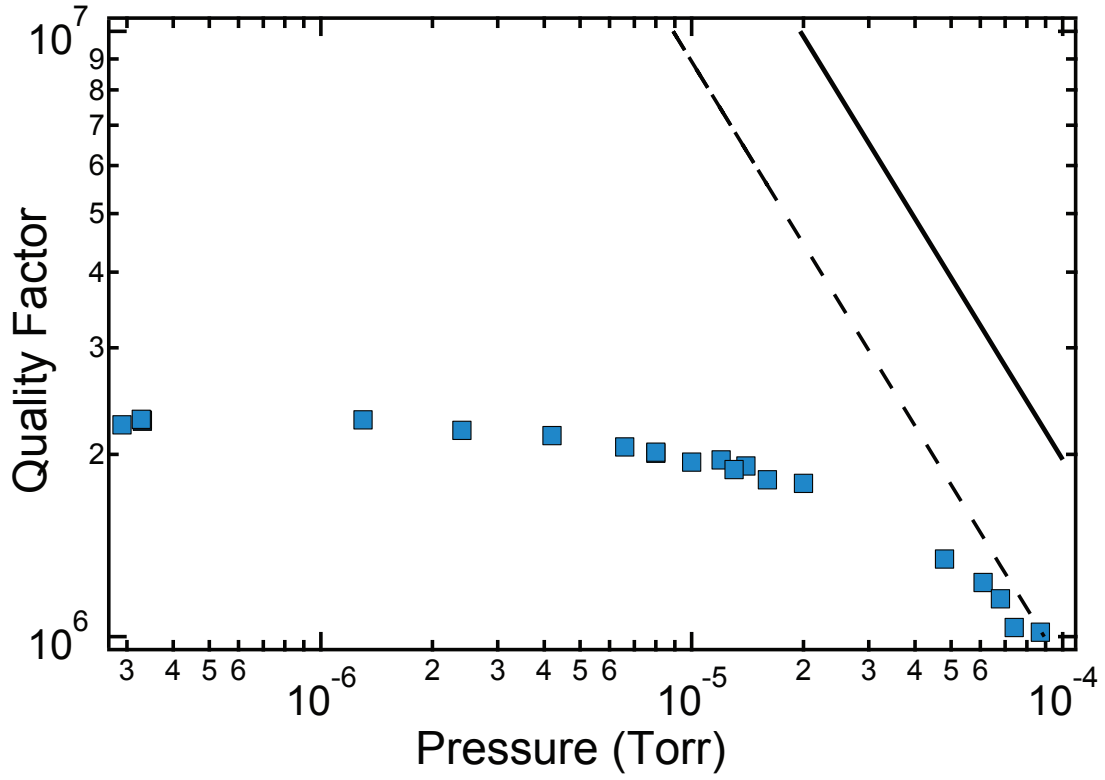


Figure 2.6: Pressure dependence of mechanical quality factors. Saturates well before the operating pressure of $2 \times 10^{-7}$ Torr. The black curve shows quality factor limit set by viscous damping, given by Eqn.2.7, for $h = 50nm$, and $\rho = 2.7$ g/cm$^3$, the mass density of silicon nitride. The air damping is assumed to be from Nitrogen. The dashed curve is the same expression scaled by a factor of 2.1 required to match with the rise in the experimentally measured quality factors.

of 5 in either direction do not change the measured value of the quality factor, indicating that we are in a regime far away from nonlinearities of the mechanical resonator.

(3) Negligible influence of viscous damping at the operating background pressure of $2 \times 10^{-7}$ torr. Fig.[2.6] shows the variation in quality factor for a mode of a membrane (21 mode of a $L = 1$ mm, $h = 50$ nm membrane) as a function of

pressure in the vacuum chamber. The quality factor saturates well before the operating pressure. The black curve shows the pressure limit to the mechanical quality factor[22] given by the expression,

$$Q_{jk}(p) = \left(\frac{\pi}{2}\right)^{3/2} \rho h \nu_{jk} \sqrt{\frac{k_B T}{m_g}} \frac{1}{p} \tag{2.7}$$

with $h = 50nm$ being the thickness, and $\rho$ the mass density of silicon nitride. The dashed curve is the same expression scaled by a factor of 2.1, required to match with the rise in the experimentally measured quality factors.

(4) The mechanical line width inferred from thermal Brownian motion, and from the response to frequency sweeps of the drive force, near resonance are consistent with that derived from the ringdown measurements. This can be seen for instance in Fig.[2.5], where we see that the quality factor obtained from a ringdown measurement (left) is consistent with the width obtained from the driven response (right). For high Q modes, this required the stabilization of the frequencies of the membrane modes (see Sec.[4.2]).

### 2.5.2 Summary of results

The quality factor measurements were performed for a host of membrane geometries ranging in width from $L = 0.5$ to 5 mm and in thickness from $h = 30$ to 200 nm. The measured quality factor versus frequency for the $L = 5$ mm membranes are shown in Fig.[2.7], with the blue open squares representing the quality factors for $h = 30$ nm membrane, while the green squares represent those of a $h = 100$ nm membrane. We can clearly distinguish between two regimes of behavior. For mode indices $(j, k)$ such that $\sqrt{j^2 + k^2} <\sim 4$, the peak quality factor values in a given frequency window increase with increasing frequency. In this regime, we

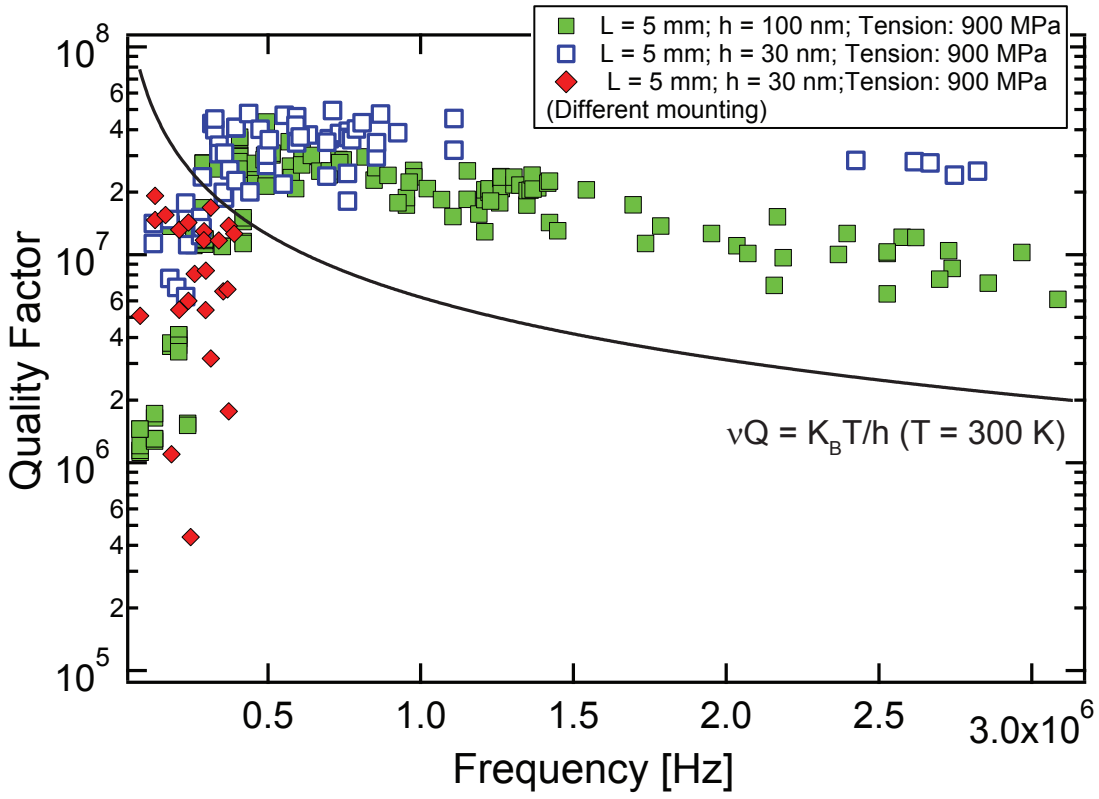


Figure 2.7: Peak mechanical quality factors of a L = 5 mm, h = 100 nm SiN membrane versus frequency (green squares). The solid line corresponds to $f \times Q = k_B/h \times 300K$. For low mode frequencies ($\nu < 300$ kHz), the quality factors can be improved by an order of magnitude (red diamonds) by reducing the contact region between the substrate and the in-vacuum mount. The weak frequency dependence of the measured Qs at high frequencies is further reduced for a h = 30 nm membrane (blue open squares).

observe a large variation and a sensitive dependence of the quality factors on the clamping mechanism, which can be greatly reduced by ensuring minimal contact between the supporting silicon wafer and the in-vacuum mount. See for instance the data represented by the filled diamonds in Fig.[2.7], which are measurements performed with the membranes mounted using a sharp piece of aluminum making contact with the edge of the silicon chip at one point. The observations in this

regime are consistent with the dominant loss mechanism being anchor losses from the membrane into the supporting mount.

For mode indices $\sqrt{j^2+k^2} >\sim 4$, we observe a characteristic variation of peak quality factors, where the peak quality factors plateau at around $40-50\times10^6$ and then weakly decrease with frequency. The frequency dependence becomes weaker with decreasing thickness, decreasing lateral dimensions and increasing tensile stress (see Fig.[2.7]).

The peak quality factors in this plateau regime, for membranes ranging in width from $L = 0.5$ to 5 mm and in thickness from $h = 30$ to 200 nm, are shown in Fig.[2.8], as a function of the membrane aspect ratio $\left(\frac{L}{h}\right)$. The peak quality factor

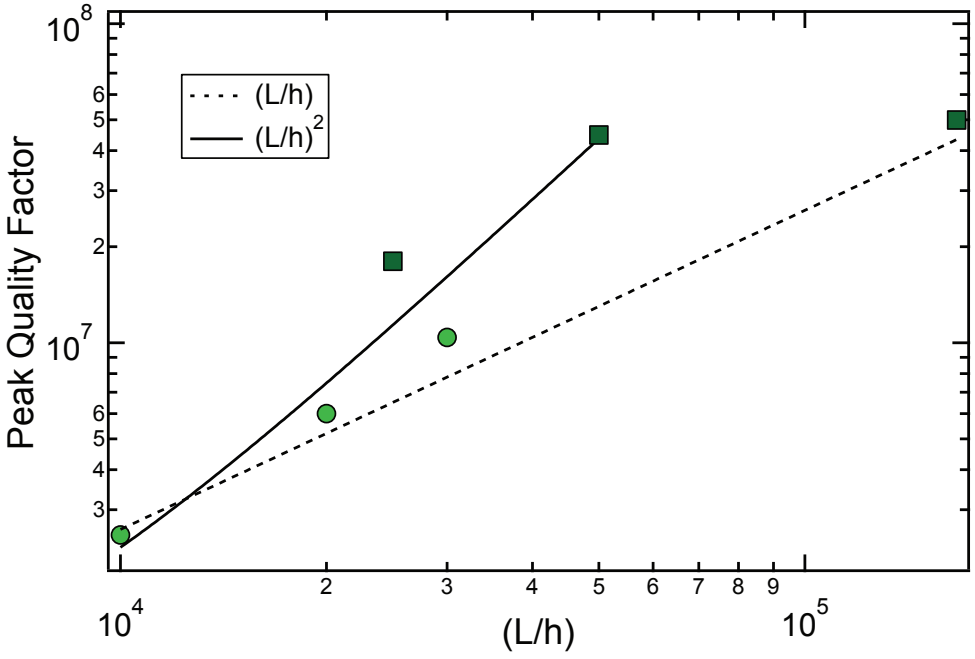


Figure 2.8: Peak mechanical quality factor versus membrane geometry, parametrized by the ratio of the membrane width (L) to the thickness (h). The squares indicate membranes with a width of 5 mm, with the aspect ratio changed by changing the thickness, while the circles indicate membranes with a thickness of 50 nm, with the aspect ratio changed by changing the width.

increases with the membrane aspect ratio and for $\frac{L}{h} < 10^5$ scales approximately as $Q \sim (\frac{L}{h})^2$ and $f \times Q \sim (\frac{L}{h})$. The thinnest membranes ($h = 30$ nm) however do not obey this scaling. In order to rule out additional surface contamination of the 30 nm membrane, we annealed the membrane in an argon environment at 650° C. This did not lead to an increase in the mechanical quality factors, as can be seen from Fig.[2.10]. XPS measurements of the surface constitution of these

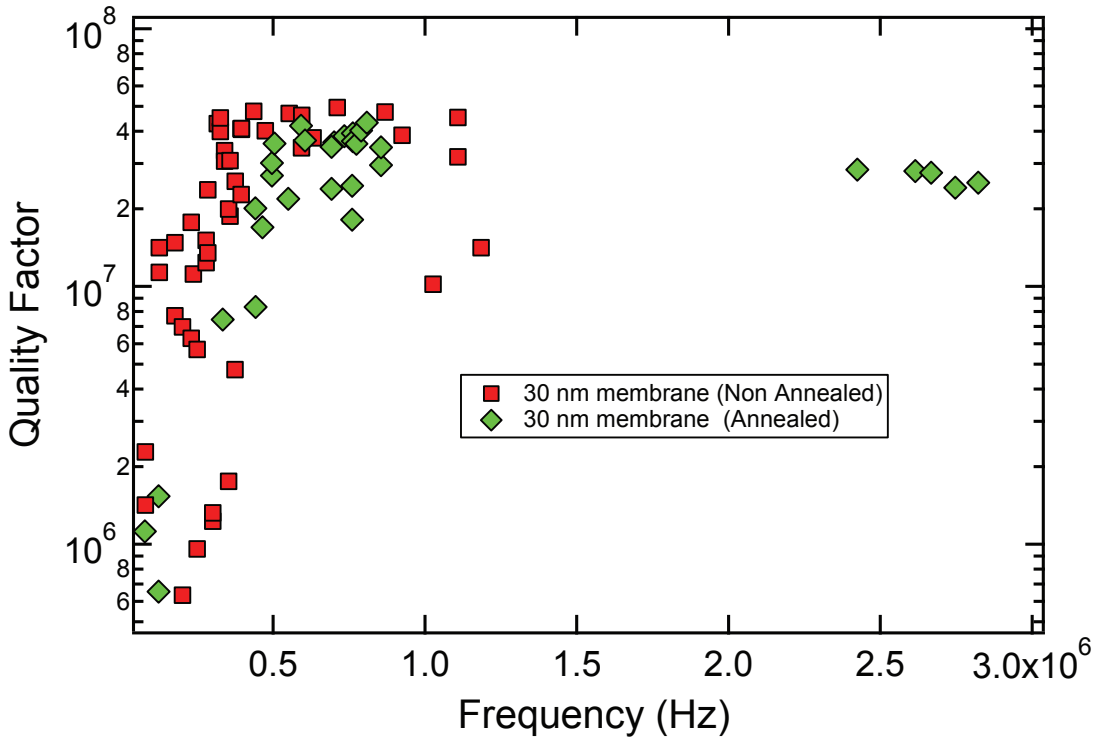


Figure 2.9: Quality factors of a 30 nm membrane before and after annealing at 650° C.

membranes revealed no additional contamination of these membranes, in comparison to membranes of other thicknesses. The reason for the apparently discrepant behavior of the thinnest membranes is therefore still unknown.

## 2.6 Overview of dissipation mechanisms

The sources of dissipation in silicon nitride membranes have received a lot of attention in recent years [9][23][11][17][24][25][26][27], with still no consensus on the limiting damping mechanism in these resonators. The range of damping mechanisms in these membranes can be broadly classified into intrinsic mechanisms, where the loss process occurs inside the membrane resonator and extrinsic mechanisms, where the loss occurs due to inevitable coupling between the membrane and the supporting substrate.

Among these intrinsic processes, some are fundamental, i.e., they would be present even in a defect free 'ideal' material. These include, thermoelastic damping and Akheizher damping (arising from phonon-phonon coupling). Other intrinsic mechanisms occur due to the coupling between the phonons and surface or bulk defects in the membrane resonator.

Even if these processes were absent, which we could imagine would be the case at low temperatures and for more perfect materials, there would still be loss due to coupling between the resonator and the surrounding substrate. Once the energy leaks from the resonator to the supporting substrate, it may either be dissipated there or propagated away. This corresponds to radiation loss of the elastic energy from the resonator. A summary of the damping mechanisms in these resonators is listed in the table below.

| Intrinsic | | Extrinsic | |
|---|---|---|---|
| Fundamental | Material | Loss in the substrate | Anchor loss |
| Thermoelastic Damping | Surface loss in the membrane | Thermoelastic damping: substrate | Loss due to phonon tunneling into the substrate |
| Akheizer Damping | Loss in the bulk of the membrane | Material loss in the substrate | Corrections from substrate induced mode hybridization |

## 2.7 Thermoelastic damping

We start by considering thermoelastic damping (TED) originally considered by Zener in [28]. TED arises as a result of the nonlinear coupling between the acoustic resonator mode and the bath of thermal phonons, in the limit where the mean free path of the thermal phonons is much smaller than the wavelength of the acoustic wave/resonator mode. In this limit, where the thermal phonons are diffusive, the resonator can be associated with a local temperature which is different at different locations as a result of the local changes in volume arising from the resonator motion. Thermoelastic dissipation arises due to irreversible heat flow from these local temperature gradients. The interactions between the acoustic mode and the bath of thermal phonons is characterized by the coefficient of thermal expansion $\alpha$. The term in the free energy that captures this is given by

$$\delta F = E\alpha(T - T_0)\sum_j u_{jj} \tag{2.8}$$

This is the only symmetry allowed term that is linear in the temperature deviation and the strain. Zener's model for thermoleastic damping is obtained through a generalization of Hooke's law in which the stress and the strain are related by,

$$\sigma + \tau_e\dot{\sigma} = E_R(\epsilon + \tau_\sigma\dot{\epsilon}) \tag{2.9}$$

where $\tau_e$ and $\tau_r$ are relaxation constants for the strain and the stress respectively. Fourier transforming the above equation and calculating the ratio of the imaginary and real part of the complex elastic modulus results in the quality factor limit given by

$$Q^{-1} = \Delta_M \frac{\omega\tau}{1+(\omega\tau)^2} \tag{2.10}$$

where in the above,

$$\Delta_M = \frac{E_{ad} - E}{E} = \frac{E\alpha^2 T_0}{C_p} \tag{2.11}$$

where $E_{ad}$ and $E$ are the adiabatic and isothermal elastic moduli, $T_0$ is the resonator temperature, $\alpha$ is the coefficient of thermal expansion and $C_p$ is the heat capacity. The relaxation timescale goes as $\tau \propto b^2$ where $b$ is the smallest dimension of the resonator. The exact derivation is done for a cantilever, whose width is $b$. The dependence on the square of the dimension arises as a result of the diffusive nature of the heat flow. Thermoelastic dissipation therefore grows with decreasing dimensions of the resonator and decreases with decreasing temperature. The above expressions are valid for an unstressed cantilever resonator. The simple Zener model provides results that are similar to a more exact calculation of the same done in [29].

We now model the thermoelastic damping for a silicon nitride membrane resonator, under stress, based on the formalism introduced in Ref.[29],[30]. The internal stress in the silicon nitride drastically changes the quality factor limit set by thermoelastic damping. We start with Eqn.[2.1] for a membrane with flexural rigidity, under tension. We note that in terms of the deviation of the membrane along the z direction $w(x,y)$, the strain tensor is given by

$$\begin{aligned} u_{ij} &= \frac{1}{2}\left(\frac{\partial u_i}{\partial x_k} + \frac{\partial u_j}{\partial x_i}\right) \\ &= \frac{1}{2} z \left(\frac{\partial^2 w}{\partial x_i \partial x_j} + \frac{\partial^2 w}{\partial x_j \partial x_i}\right) \end{aligned}$$

The equation of motion in the presence of thermal strain becomes ([31]),

$$D\nabla^4 w - \sigma h \nabla^2 w + \rho h \frac{\partial^2 w}{\partial t^2} = -\nabla^2 M^T - N^T \nabla^2 w \tag{2.12}$$

The terms on the right of the above equation are effective forces resulting from thermal stresses and are decomposed into a thermal axial force and thermal bending moment[31] as given below:

$$\begin{aligned} N^T &= \frac{E\alpha}{1-\nu_p}\int \theta dz \\ M^T &= \frac{E\alpha}{1-\nu_p}\int z\theta dz \end{aligned}$$

The temperature field itself satisfies the standard diffusion equation which is modified in the presence of the thermoelastic term, as given below

$$\kappa\nabla^2\theta = \rho C_p \frac{\partial\theta}{\partial t} - \frac{E\alpha T_0}{1-\nu_p}\frac{\partial}{\partial t}(z\nabla^2 w)$$

The thermal diffusion that needs to be considered is along the smallest dimension, i.e., the thickness of the membrane. In the above, $\theta(x,y,z,t) = T(x,y,z,t) - T_0$ is the deviation in temperature from the equilibrium temperature $T_0$, $\kappa$ is the thermal conductivity, $\rho$ the density and $C_p$ the specific heat. The coupled thermoelastic equations (2.12),(2.13) can be solved for the normal modes of vibration by obtaining an effective equation for membrane vibration in the presence of thermoelastic damping. The quality factor can then be extracted from the corresponding eigenfrequencies using,

$$Q^{-1} = 2\frac{\Im(\tilde{\omega})}{\Re(\tilde{\omega})} \tag{2.13}$$

The effective equation for membrane vibration is obtained by first solving the diffusion equation with the boundary conditions corresponding to no heat flow at the top and bottom membrane surfaces, i.e., $\frac{\partial\theta_0}{\partial z} = 0; z = \pm\frac{h}{2}$, which gives

$$\theta_0(x,y) = \frac{E\alpha T_0}{(1-\nu_p)\rho C_p}\nabla^2 w_0(x,y)\left(z - \frac{\sin(\tilde{k}z)}{\tilde{k}\cos(\frac{1}{2}\tilde{k}h)}\right) \tag{2.14}$$

where $\tilde{k} = (1-i)\sqrt{\frac{\omega\rho C_p}{2\kappa}}$. We now return to the equation (2.12) describing the membrane displacement $w(x,y,t)$. Substituting the expressions for the thermal axial strain and bending moment (2.13), we get,

$$D\nabla^4 w_0 - \sigma h\nabla^2 w_0 + \frac{E\alpha}{1-\nu_p}\nabla^2 w_0 \int_{-h/2}^{h/2} \theta_0 dz + \frac{E\alpha}{1-\nu_p}\int_{-h/2}^{h/2} z\nabla^2\theta_0 dz = \rho h\omega^2 w_0 \tag{2.15}$$

Substituting the solution of the heat equation into the above results in a modified equation for membrane vibration [31]:

$$(D+D_t)\nabla^4 w_0 - \sigma h\nabla^2 w_0 = \rho h\omega^2 w_0 \tag{2.16}$$

where in the above, we have written $w(x,y,t) = w_0(x,y)e^{i\omega t}$ and,

$$D_t = \frac{E^2\alpha^2 T_0}{(1-\nu_p)^2\rho C_p}\left(\frac{h^3}{12} + \frac{h}{\tilde{k}^2} - \frac{2\tan(\frac{\tilde{k}h}{2})}{\tilde{k}^3}\right) \tag{2.17}$$

is the correction due to thermoelasticity. $D_t$ has a non zero imaginary part which quantifies the thermoelastic damping of the membrane vibrations.

Solving Eqn.[2.17] to obtain the normal modes and eigenfrequencies assuming standard clamped boundary conditions at the membrane edges gives the eigenfrequencies,

$$\omega_{mn} = \sqrt{\frac{\sigma\pi^2}{\rho L^2}(m^2+n^2) + \frac{(D+D_t)}{\rho h L^4}(m^2+n^2)^2\pi^4} \tag{2.18}$$

In the limit of large stress, the first term in the above equation is much larger than the second term. The small parameter comparing the tension term and the flexural rigidity $D$ is $\eta = \frac{D}{\sigma h L^2}$ which for the 5 mm membranes is $\sim 10^{-7}$. In this case (2.18) reduces to,

$$\omega_{mn} = \omega^0_{mn}\left(1 + \frac{\pi^2(D+D_t)}{2\sigma h L^2}(m^2+n^2)\right) \tag{2.19}$$

where $\omega^0_{mn} = \sqrt{\frac{\sigma\pi^2(m^2+n^2)}{\rho L^2}}$. The quality factor is therefore given by

$$\begin{aligned} Q^{-1}_{mn} &= 2\frac{\Im[\omega_{mn}]}{\Re[\omega_{mn}]} \\ &\approx \frac{\pi^2(m^2+n^2)}{\sigma h L^2}\Im[D_t] \end{aligned}$$

We have

$$\Im[D_t] = \frac{E^2\alpha^2 T_0 h^3}{12(1-\nu_p)^2\rho C_p}\Im[\frac{24}{h^3\tilde{k}^3}\left(\frac{\tilde{k}h}{2} - \tan\left(\frac{\tilde{k}h}{2}\right)\right)] \tag{2.20}$$

The imaginary part in the expression above is identical to Eqn.[22] of [29]. The above expression thus evaluates to,

$$\Im[D_t] = \frac{E^2\alpha^2 T_0 h^3}{12(1-\nu_p)^2\rho C_p} g(\xi) \tag{2.21}$$

where,

$$g(\xi) = \left(\frac{6}{\xi^3}\frac{\sinh(\xi)+\sin(\xi)}{\cosh(\xi)+\cos(\xi)} - \frac{6}{\xi^2}\right) \tag{2.22}$$

and $\xi$ in the expressions above is a dimensionless parameter given by,

$$\xi = h\sqrt{\frac{\omega_0\rho C_p}{2\kappa}} \tag{2.23}$$

The quality factor in the limit of high stress as a function of mode index and as a function of frequency therefore reduces to:

$$\begin{aligned} Q_{mn} &= \frac{12(1-\nu_p)^2}{\pi^2}\frac{1}{(m^2+n^2)}\left(\frac{\rho C_p}{E\alpha^2 T_0}\right)\frac{\sigma}{E}\left(\frac{L}{h}\right)^2\frac{1}{g(\xi)} \\ Q(\nu) &= \frac{3(1-\nu_p)^2 C_p\sigma}{\pi^2\nu^2 E^2\alpha^2 T_0 h^2}\frac{1}{g(\xi)} \end{aligned}$$

It is straight forward to obtain the result for intermediate stresses as

$$Q = \frac{12(1-\nu_p)^2\rho C_p}{E^2\alpha^2 T_0 h^3 g(\xi)}\frac{(\sigma h L^2 + D\pi^2(m^2+n^2))}{(m^2+n^2)\pi^2} \tag{2.24}$$

where in the above the function $g(\xi)$ and $\xi$ are as defined in Eqns.[2.22,2.23]. In the limit $\sigma \to 0$, the above equation reduces to the expression obtained for an unstressed plate in [30]. The low stress limit for the quality factor is the dashed orange curve plotted in Fig.[2.10]. The measured quality factors for the 5 mm membranes exceed this bound[1] which does not apply for these high stress membranes.

[1]Prior comparisons of quality factor data for high stress membranes with this low stress bound necessitated the above analysis. This error has also been noted in [18][32].

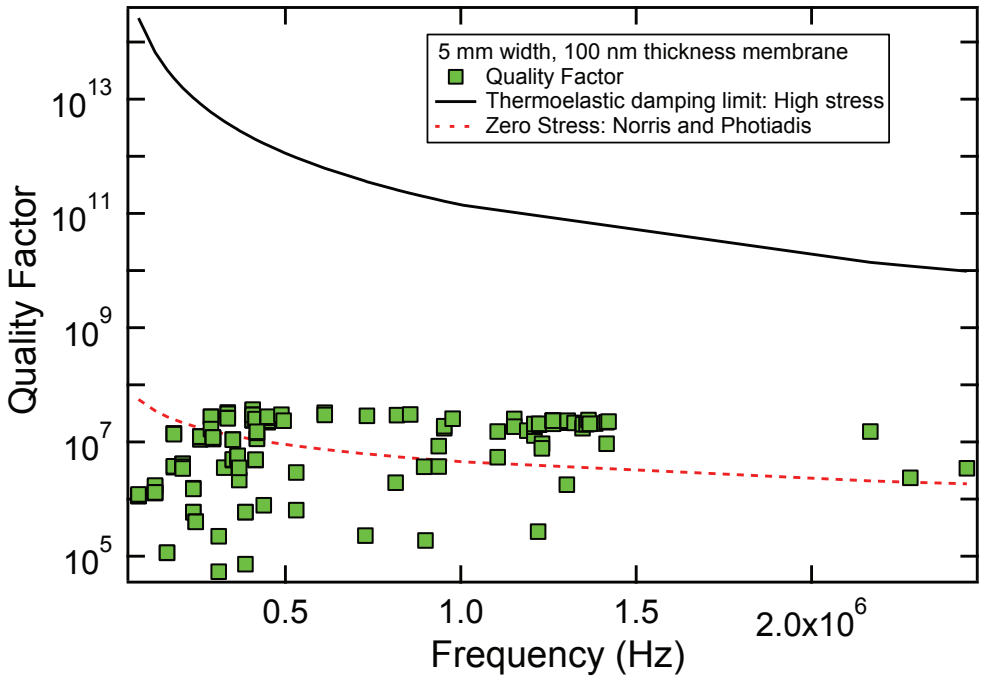


Figure 2.10: Quality factors for high stress silicon nitride (5mm, 100 nm), and the thermoelastic damping limit curves. The thermoelastic damping limit in the high stress case (black curve) is around $Q_{TED} = 10^{12}$ for $\nu = 500$ kHz, which is 5 orders of magnitude larger than the measured mechanical quality factors. The quality factor limit in the limit of low stress is given by the dashed orange curve. Material parameters: $E = 270$ GPa, $\alpha = 1.6 \times 10^{-6}$/K, $C_p = 710.6$ J/kg/K, $\kappa = 10$ W/m/K, $\nu_p = 0.27$, $\sigma = 900$ MPa, $\rho = 2.7 \times 10^3$ kg/m$^3$

For the high stress membranes, for material parameters used in our study, we find that the thermoelastic damping (TED) limit is $Q_{TED} \approx 10^{12}$ at $\nu = 500$ kHz, which is consistent with the estimate in [32]. This therefore discounts thermoelastic damping in the membrane as the limiting cause for damping in high stress silicon nitride membranes.

### 2.7.1 Thermoelastic damping in the silicon substrate

In addition to thermoelastic damping in the membrane, another source of damping that we considered was thermoelastic damping in the supporting substrate platform. This is of interest since, while the substrate dimensions are larger, it is not under stress. As a result the thermoelastic damping limit for modes of the substrate platform are lower than that of the high stress membrane. The thermoelastic damping limit for the modes of the substrate platform are shown in Fig.[2.11(a)]. The two different arcs correspond to the thermoelastic damping limits for flexu-

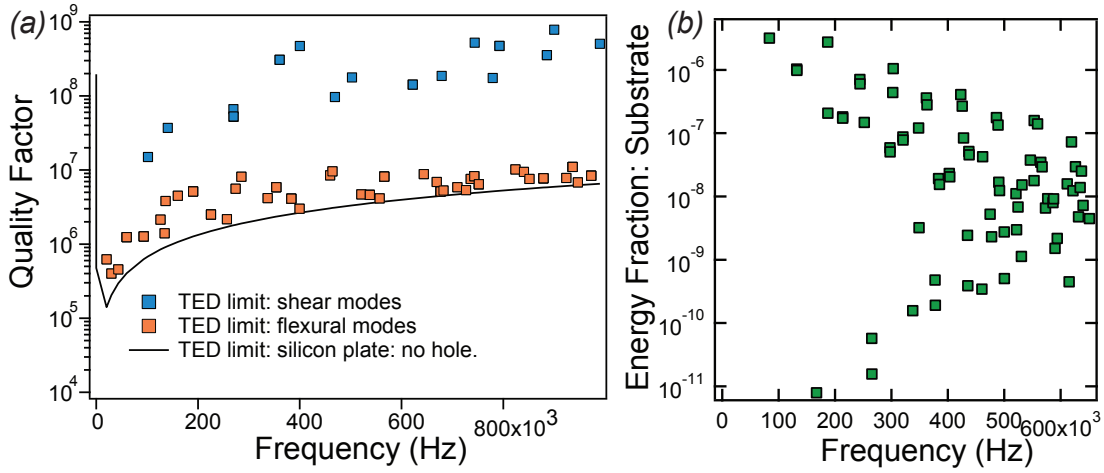


Figure 2.11: (a) Thermoelastic damping of vibrations of the susbtrate platform. The flexural modes have a lower thermoelastic damping limit since the limiting dimension is the substrate thickness as opposed to the substrate width. (b) Fraction of the elastic energy in the substrate, obtained through COMSOL simulations of the membrane and the substrate. Eigenfrequencies of the combined membrane substrate system are obtained and the fraction of elastic energy in the substrate are obtained for each eigenmode.

ral modes (orange squares), corresponding to out of plane vibrations and shear modes corresponding to in plane vibrations (blue squares). For flexural modes of

the substrate platform the quality factor limit is commensurate with the measured membrane quality factors (see Fig.[2.11]). An estimate of the membrane quality factor limit set by this mechanism can be obtained by considering the thermoelastic limit for the substrate modes in conjunction with the elastic energy of the membrane substrate system that is stored in the substrate (Fig.[2.11](b)). This fraction, estimated through COMSOL simulations of the membrane substrate system, is $< 10^{-6}$. Therefore a naive lower bound for the mechanical quality factors would be $E_{mem}/E_{sub} \times Q_{TED}^{sub} > 10^{12}$, i.e., much larger than the measured membrane quality factors. We therefore discount this as a limiting mechanism for the observed quality factors.

## 2.8 Akheizer damping

Akheizer damping[33] is a fundamental source of intrinsic damping arising from phonon-phonon coupling. Unlike thermoelastic damping, where a spatially modulated strain leads to heat flow between different spatial locations, Akheizer damping involves energy flow between different phonon modes. The strength of Akheizer damping is given by the Gruneisen parameter $\gamma$, characterizing the strength of the coupling between phonons. The quality factor limit arising from this coupling is of the general form[34],

$$Q_{akh}^{-1} = \frac{CT\gamma^2}{\rho v^2} \frac{\omega\tau_{ph-ph}}{1+\omega\tau_{ph-ph}^2} \tag{2.25}$$

here $C$ is the specific heat, $T$ is the temperature, $\rho$ is the density and $v$ is the speed of sound. The relaxation time $\tau_{ph-ph}$ for this process is given by $\tau_{ph-ph} = \frac{3k}{Cv^2} \approx 0.1 - 10$ ps [35], where $k$ is the thermal conductivity. An estimate of the Akheizer

damping limit to the quality factors is therefore,

$$Q_{akh}^{-1} = \frac{CT\gamma^2}{\rho v^2}\omega\tau \approx \frac{6\pi\nu T k\gamma^2}{\rho v^4} \approx 3 \times 10^{-9} \tag{2.26}$$

for $\nu = 1$ MHz and using the bulk properties of silicon nitride ($k = 10W/m/K$; $\gamma = 1$, $\rho = 3.2\ g/cm^3$, $v = 8800$ m/s). While this analysis does not take into account the intrinsic stress of the silicon nitride, it provides an order of magnitude estimate that suggests that the phenomenon is not relevant for explaining the observed quality factors.

## 2.9 Intrinsic material dissipation

Having discounted thermoelastic damping and Akheizer damping, we proceed to intrinsic damping arising from the phonons coupling to defects present in the silicon nitride membranes. The nature of the defects in the silicon nitride that play a role in the mechanical dissipation is largely unknown. One that has received some attention[23], is the coupling between mechanical motion and intrinsic, localized defects within the membrane. The losses in this case are modeled as being due to coupling between phonons and two-level systems, with the energy splitting of the two level systems being modulated by an oscillating strain field[36]. The re-equilibration of excited two-level systems results in the attenuation of the mechanical energy.

Given that our experiments are conducted at room temperature, we may consider these two-level systems to be thermally activated over a wide range of energies. The temperature dependence of the dissipation within this model, while not showing an Arrhenius type behavior, still shows a strong temperature dependence with $Q^{-1} \propto T^3$ (See [37]). However it is well known that dissipation in silicon nitride

does not show a significant temperature dependence[23]. Our own data on the temperature dependence of the mechanical quality factors, shown in Fig.[2.12], albeit over a small temperature range of $\sim 50°$C, does not appear to show a change in the peak quality factor values (The variation of the qaulity factor with temperature seen for a few modes, such as those designated by the black squares in Fig.[2.12] are due to resonances with modes of the substrate platform[38]).

Additionally, for the mechanical frequencies in this work, the two-level system

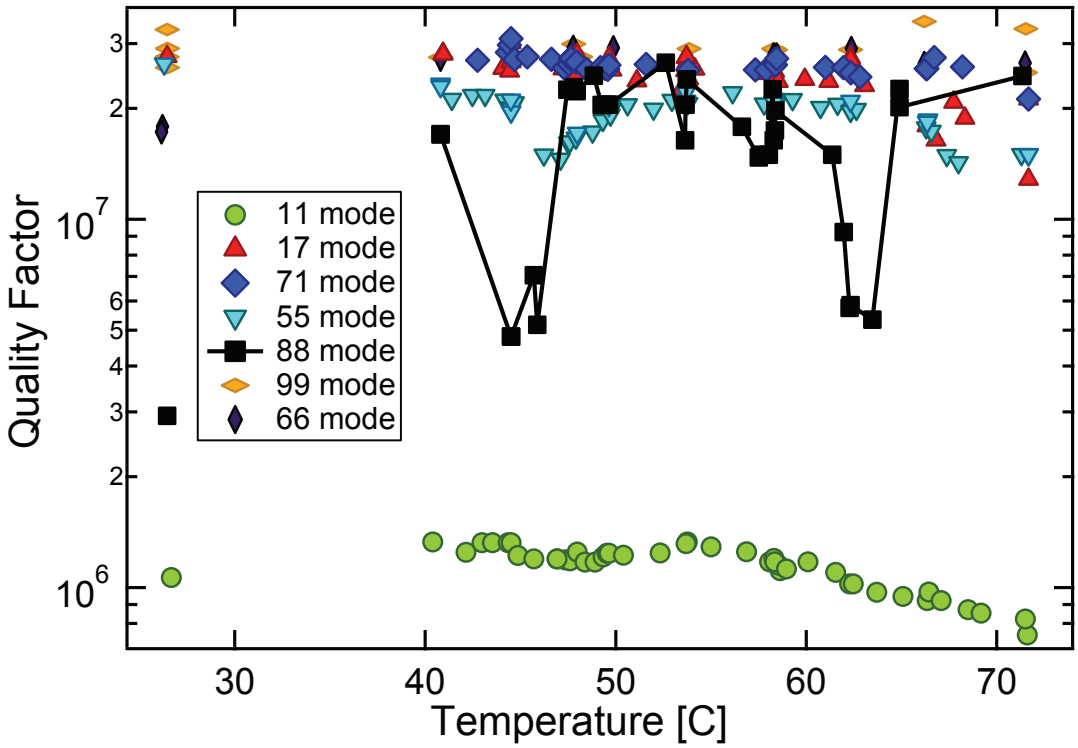


Figure 2.12: Temperature dependence of mechanical quality factors over a temperature range of $50°C$. Most of the modes show barely any change in the mechanical quality factors. The large change in the mechanical quality factor of one of the modes (88 mode: black) is believed to be due to resonance with a mode of the substrate platform.

model [39] predicts a scaling of $Q_{jk} \propto \frac{1}{\nu_{jk}}$ and a dissipation that is independent

of the mode geometry, dimensions of the resonator and the details of the support structure, which are inconsistent with our observations.

We therefore discount this intrinsic loss mechanism based on the absence of the correct scaling of quality factors with frequency and the absence of temperature dependence of the measured quality factors.

### 2.9.1 Mechanism agnostic intrinsic damping: defects coupling to membrane curvature

Another intrinsic damping mechanism is that proposed in [25],[26]. Here a specific microscopic mechanism is not considered, but the intrinsic damping is instead phenomenologically modeled through an imaginary elastic modulus. The dissipation is proportional to the imaginary part of the elastic energy, which is proportional to the square of the curvature of the displacement field, the leading symmetry allowed term. Given the quartic term in Eqn.[2.1] and given that the resonator satisfies clamped boundary conditions[2] at the resonator substrate interface,

$$w(x,y)|_{edge} = \frac{\partial w}{\partial n}|_{edge} = 0 \tag{2.27}$$

where $n$ is the direction normal to the edge, the membrane displacement near the edges deviates from sinusoidal functions. The length scale of this exponential tail, obtained by solving Eqn.[2.1], with the above boundary conditions is given by $\frac{\lambda L}{4}$, where $\lambda = \sqrt{\frac{Eh^2}{12(1-\nu_p^2)\sigma L^2}}$, where $E$ is the Young's modulus and $\nu_p$ is the Poisson ratio, and $L$ is the width of the resonator[25]. Most of the curvature of the membrane occurs at clamped edges, given the short length scale over which the

[2]assuming that the substrate is rigid. The basis of anchor loss models is that the base at the point of attachment is not rigid. Instead the point of attachment moves, resulting in work being done by the resonator and concomitant energy loss.

membrane deviates from sinusoidal behavior ($\sim$ 100 nm). This model therefore predicts a quality factor that is largely flat with frequency, with a slight decrease in the quality factors due to the small additional contribution coming from the curvature at the antinodes. The predicted quality factor as a function of mode index is,

$$Q_{m,n} = \frac{Q_{intr}}{2\lambda + (n^2 + m^2)\pi^2\lambda^2} \tag{2.28}$$

The model does not explain the variation seen in the measured quality factors with mode number over a given frequency window. This can be seen by plotting the quality factor as a function of the measured curvature using modal images obtained through our interferometric imaging technique. We observe that the quality factors can vary by almost 2 orders of magnitude for a corresponding variation in the integrated curvature of less than 20%, pointing to a weak correlation between the two quantities. This can be seen in Fig.[2.13], where the green squares show the variation of the measured quality factors as a function of the measured curvature. The red diamonds show the expected variation of the quality factors based on Eqn.[2.28]. We note here that the measured curvature does not include the contribution from the curvature near the clamp, which is below the resolution of our images. This notwithstanding, such a source of loss cannot explain the dramatic variation in quality factors seen for a given frequency with variation in mode index. Additionally, as we will see in Sec.[2.10], the large variation in quality factor has a specific functional dependence on the mode index that is not captured by this model. The model however appears to be consistent with the observed weak decrease in peak quality factor with increasing frequency, and its dependence on the membrane width and thickness, as can be seen in Fig.[2.14]. The loss modulus, extracted from these, which is a phenomenological fit parameter, varies by a factor of 2 over the membrane geometries considered and is found to increase with

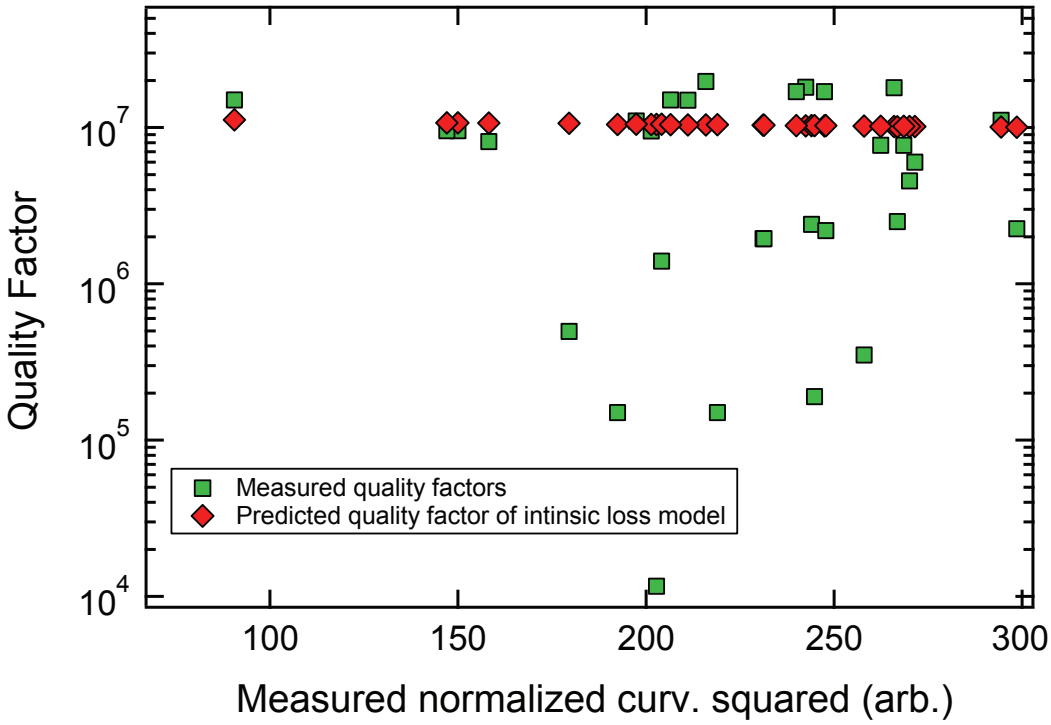


Figure 2.13: Quality factor vs measured curvature. There is no correlation between the measured quality factors and the measured curvature. The figure shows the quality factors of all modes between 300 and 400 kHz for a membrane with parameters: $\sigma = 250$ MPa, $L = 5$ mm, $h = 100$ nm. The relation between the measured curvature and the calculated curvature can be found in Fig.[2.20] of Appendix.[2.1].

decreasing membrane thickness (Inset of Fig.[2.14]).

A purely intrinsic loss modulus can also not explain the variation in the peak quality factor for the same membrane geometry, through a change in just the substrate thickness (See Fig. 4.9 of [18]). It remains to be seen if such an imaginary loss modulus can arise an from effective coupling to the substrate, i.e., through anchor loss.

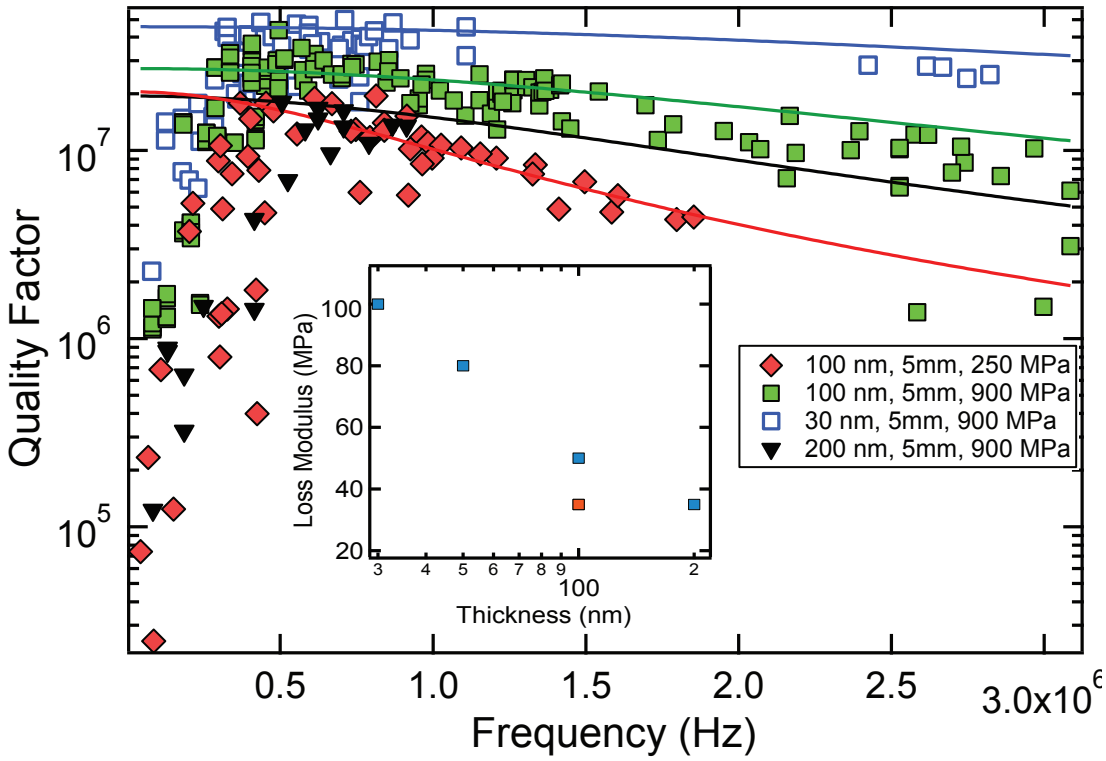


Figure 2.14: Graphs of peak quality factor versus frequency for various membrane geometries, membrane parameters shown in the legend, with fits to an intrinsic loss model parametrized by an imaginary frequency independent elastic (loss) modulus. (Inset) Loss moduli values from the fit are plotted as a function of membrane thickness (Blue squares correspond to high stress (900 MPa) membranes, orange square corresponds to low stress membrane(250 MPa)). For comparison, the Young's modulus of SiN is $\sim 270$ GPa.

## 2.10 Radiation loss to the surrounding substrate

Finally, we consider the role of radiation loss from the membrane into the supporting substrate, arising from the work done by the resonator on the substrate, as the resonator moves. There are various treatments of anchor loss that have been considered in the literature [11][24][40][41][42][43]. The one that we consider here

is based on the picture of 'phonon tunneling' [11][24][40], wherein the resonator can be regarded as a phononic cavity, weakly coupled to the surrounding substrate. Every time the phonon wavepacket hits the boundary of the resonator, there is a probability of transmission to the substrate. The anchor loss limited quality factor is therefore heuristically given by[40],

$$Q(\omega)^{-1} \approx \frac{c_R}{\omega L} T(\omega) \tag{2.29}$$

where $T(\omega)$ is the transmission coefficient from the resonator to the substrate and $\frac{c_R}{\omega L}$ is the rate at a phonon wavepacket hits the wall of the resonator per oscillation period. The transmission coefficient can be obtained by solving for the boundary conditions at the resonator substrate interface, in a manner similar to the case of an electromagnetic cavity.

An alternative way to calculate the transmission probability is to use Fermi's golden rule to obtain the decay rate of a phonon of the resonator coupled to the continuum of modes of the support[44], and use it to extract the anchor loss limited quality factor in the classical limit. We consider the resonator, the substrate and the resonator substrate coupling to be characterized by the following Hamiltonian[11],

$$\hat{H} = \hat{H}_0 + \hat{H}' = \hbar\omega_R b_R^\dagger b_R + \int_q \hbar\omega(q) b_q^\dagger b_q + \hbar \int_q (\xi(q) b_q + \text{hc}) \left( b_R^\dagger + b_R \right) \tag{2.30}$$

$H'$ parametrizes the coupling between the resonator and the substrate, and in what follows will be related to the physical interaction between the resonator and the substrate at the periphery of the resonator. The rate of transition from state $|n, 0\rangle \rightarrow |n-1, q\rangle$, through Fermi's golden rule is,

$$\Gamma_{n\rightarrow n-1} = \frac{2\pi}{\hbar} \int d^3q \left| \langle n, 0 | \hat{H}' | n, q \rangle \right|^2 \delta(E - E_q) \tag{2.31}$$

The matrix element in the above equation evaluates to,

$$\langle n, 0 | \hbar \int_q \left[ \xi(q) b_R^\dagger b_q + \text{hc} \right] | n, q \rangle = \sqrt{n} \hbar \xi(q) \tag{2.32}$$

The quality factor is hence given by,

$$Q^{-1} = \frac{\dot{E}}{\omega E} = \frac{\Gamma_{n\to n-1}\hbar\omega}{\omega\left(n\hbar\omega\right)} = \frac{\Gamma_{n\to n-1}}{n\omega} = \frac{2\pi\int_{d^3q}\left|\xi(q)\right|^2\delta(\omega-\omega_q)}{\omega} \tag{2.33}$$

Note that the Fock state index $n$ and the factors of $\hbar$ cancel in the equation above. The coupling between the resonator and the substrate is computed through the expression for the work done at the resonator substrate interface[19][11] and is given by,

$$H' = \int_S d\vec{S}.\left(\breve{\sigma}^0_{sub}.\vec{u}_{res} - \breve{\sigma'}_{res}.\vec{u}_{sub}\right) \tag{2.34}$$

where $S$ indicates the contact area between the resonator and the substrate at the resonator periphery. In order to go from Eqn.2.34 to the expression for $\xi(q)$ in Eqn.[2.30], we write the resonator, substrate stress and displacement in terms of their respective normal modes using the standard decomposition given by[11],

$$\begin{aligned}
\vec{u}_{sub}(r) &= \int_q \sqrt{\frac{\hbar}{2\rho_s\omega(q)}}\left(\vec{u}_q b^\dagger_q + \text{hc}\right) \\
\vec{u}_{res}(r) &= \sum_n \sqrt{\frac{\hbar}{2\rho_R\omega_{R,n}}}\left(\vec{u}_R b^\dagger_R + \text{hc}\right)
\end{aligned}$$

Substituting the expressions above into Eqn.[2.34] results in,

$$\xi(q) = \sqrt{\frac{1}{2\rho_s\omega(q)}}\sqrt{\frac{1}{2\rho_R\omega_{R,n}}}\int_S d\vec{S}.(\breve{\sigma}^0_q.\vec{u}_{R,n} - \breve{\sigma'}_{R,n}.\vec{u}^0_q) \tag{2.35}$$

The above equation, along with Eqn.[2.33] results in the following expression for the anchor loss limited quality factor, identical to that obtained in [11],

$$\frac{1}{Q} = \frac{\pi}{2\rho_s\rho_R\omega_R^3}\int_q d^dq\left|\int_S d\vec{S}.(\breve{\sigma}^0_q.\vec{u}_R - \breve{\sigma'}_R.\vec{u}^0_q)\right|^2 \times \delta(\omega_R - \omega(q)) \tag{2.36}$$

Note that $\sigma'_R$ is the change in stress field associated with the normalized resonator mode and $\vec{u}_q$ the displacement field for the continuum of free modes of the substrate. Given the clamped boundary conditions satisfied by the resonator, $\vec{u}_R = 0$, only the second term in Eqn.[2.36] contributes, i.e.,

$$\frac{1}{Q} = \frac{\pi}{2\rho_s\rho_R\omega_R^3}\int_q d^dq\left|\int_S d\vec{S}.(\breve{\sigma'}_R.\vec{u}^0_q)\right|^2 \times \delta(\omega_R - \omega(q)) \tag{2.37}$$

The support modes are labeled by a wave vector index $q$, with $\omega_q$ being the corresponding eigenfrequency. Note that the in the above expression, $\rho_s, \rho_R$ are $2d/3d$ densities depending on the model for the resonator and the substrate. The membrane can typically be well approximated as 2 dimensional and therefore $\rho_R = \rho_{SiN} t$ where $t$ is the thickness of the silicon nitride. In [24] the substrate is modeled as an elastic half space with infinite thickness (see inset Fig.[2.15]). Further more, the under etched gap between the resonator and the substrate is ignored. Such a space supports longitudinal, transverse and surface acoustic waves. The wavelength of the various substrate waves are plotted as a function of frequency in Fig.[2.15]. At low frequencies, i.e. upto 300-400 kHz, the wavelengths of the acoustic waves

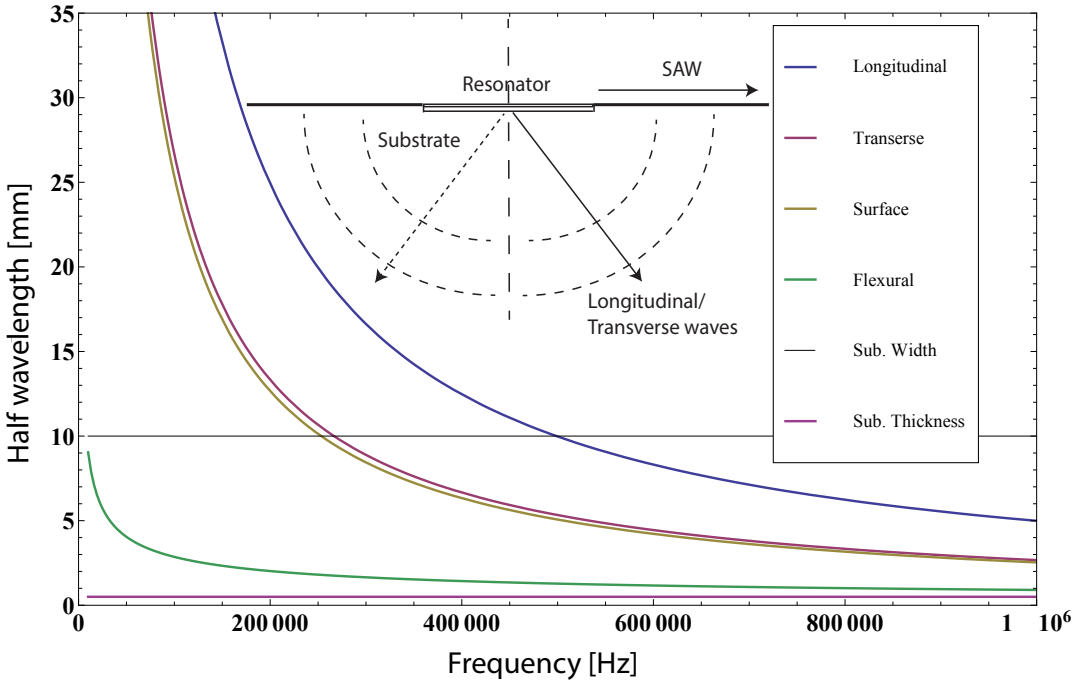


Figure 2.15: Half wavelengths of various waves in a silicon substrate as a function of frequency. The width of the substrate is 10 mm and the thickness of the substrate is 500 $\mu m$.

are larger than the lateral size of the silicon substrate. This is consistent with

the fact that for frequencies less than 300 - 400 kHz, the quality factors are drastically affected by the clamping mechanism of the substrate to the underlying aluminum chuck (See Sec.[2.5]). At all frequencies of interest, the half wavelengths are greater than the thickness of the substrate. Typically, the quality factor limit is determined by the impedance mismatch between waves in the resonator and waves in the substrate[24], characterized by the parameter

$$\eta_\gamma = \frac{c_\gamma}{c_R} \sim \sqrt{\frac{E_s \rho_R}{\sigma \rho_s}} \tag{2.38}$$

where $c_\gamma$ and $c_R$ are the sound velocities in the resonator and the substrate. The larger this parameter is, the lesser the radiated acoustic energy and the higher the quality factor limit (with a dependence going as $\eta_\gamma^3$ for coupling to a 3d substrate). This can be heuristically understood from the fact that $Q^{-1}$ is proportional to the substrate density of states. As the speed of sound in the substrate is increased, the density of modes of the substrate at a given frequency decreases as $\frac{1}{c^3}$ where $c$ is the speed of sound in the substrate.

There are additional factors arising from an explicit evaluation of the integral in Eqn.[2.37] associated with the overlap between the resonator and the substrate mode. The large intrinsic stress of the stoichiometric SiN and the extremely small thickness of the membrane allow us to relate the stress field at the periphery to the slope of the resonator mode evaluated at the clamp[24],

$$\int \hat{z}.\breve{\sigma'}_R.\hat{x}dz = \sigma t \frac{\partial \phi_R}{\partial x} \tag{2.39}$$

where in the above expression x is the direction normal to clamp edge, t is the membrane thickness and $\sigma$ is the intrinsic tensile stress and $\phi_R(x, y)$ is the membrane eigenmode. For a square membrane, this results in the expression,

$$\begin{aligned} \int_S d\vec{S}.\breve{\sigma'}_R.\vec{u}_q^0 &= 2\sigma t \int u_{\gamma,\lambda}(x = L/2, y) \frac{\partial \phi_R}{\partial x}|_{x=L/2} dy \\ &+ 2\sigma t \int u_{\gamma,\lambda}(x, y = L/2) \frac{\partial \phi_R}{\partial y}|_{y=L/2} dx \end{aligned}$$

where in the above, $\gamma$ indexes the type of substrate wave, i.e. longitudinal (l), transverse (t) and surface acoustic waves (s), and $\lambda$ an index of the substrate eigenmodes based on ts symmetry. The ideal square membrane and the substrate system is reflection symmetric about the x-z and y-z planes and the eigenmodes of the substrate can be decomposed into eigenmodes of these reflection symmetry operators. The contributions to the integral in Eqn.[2.40] only arise from substrate and resonator modes that share the same symmetry, i.e. resonator modes with even parity only couple to substrate modes with even parity etc. An explicit evaluation of the integral above[24],results in the following expression for the mechanical quality factor,

$$\frac{1}{Q_{nm}} = \frac{16\pi n^2 m^2 \rho_R t}{\sqrt{m^2+n^2}\rho_s D} \sum_{l,\gamma} n_\gamma^3 \tilde{w}_{l,\gamma}^{n,m}(\sqrt{m^2+n^2}\eta_\gamma, \nu_s) \tag{2.40}$$

with the function $w_{l,\gamma}^{n,m}$ are functions that parametrize the resonator substrate overlap, listed in [24][11].

This phonon tunneling model leads to a large difference in the quality factors for modes with even and odd parity[24], with the even parity modes having a higher predicted quality factor due to destructive interference of the radiated elastic waves. This is observed to a degree for modes with low mode indices (see Fig.[2.16]), particularly for the membranes with small sizes and correspondingly higher frequencies. In contrast, for the low mode indices of the $L = 5$ mm membranes, the distinctive parity dependence predicted by the above formalism is not seen in the measured data. This is due to the fact that the wavelengths of the modes of the substrate are larger than the substrate length which means that the radiated elastic waves see the underlying mount which breaks the x-y reflection symmetry which is crucial for the destructive interference effect.

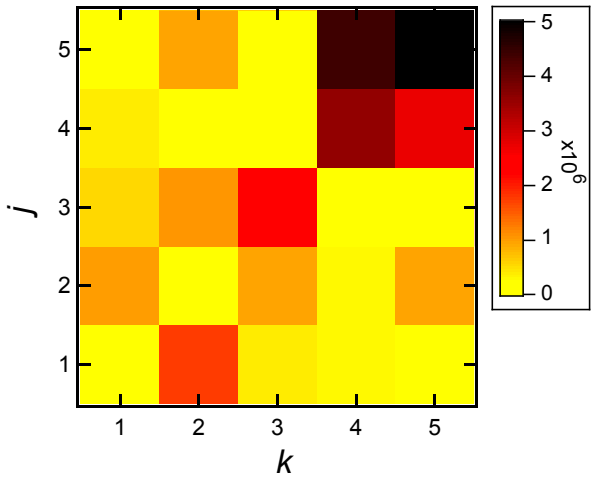


Figure 2.16: Parity dependence of the measured quality factors for the low mode indices. Membrane dimensions; $L = 0.5$ mm, $h = 50$ nm.

### 2.10.1 Modification arising from substrate mediated hybridization

The mode patterns for the high mode indices $\sqrt{j^2 + k^2} > 4$ (the plateau regime) also do not show this distinctive parity dependence. These modes are observed to be often hybridized into linear combinations of (j,k) and (k,j) on account of substrate induced mode coupling (See Fig.[2.17]). In order to isolate the geometrical dependence of the quality factor, we consider the $Q$s measured over a narrow range of frequency corresponding to an arc of radius $\sqrt{j^2 + k^2} \sim 12$ in the $(j, k)$ (shown in Fig.[2.18]). We model this substrate induced mode coupling by using the hybridized modes to calculate the radiation loss based on the phonon tunneling expression Eqn.[2.37] and Eqn.[2.40], with $\phi_R$ now being the hybridized modes. We see that the substrate-induced mode coupling and ensuing hybridization suppresses the large $Q$ variation between modes of even and odd parity (see Fig.[2.18(b)]). Instead, we observe a more gradual variation with lower $Q$s measured for modes with

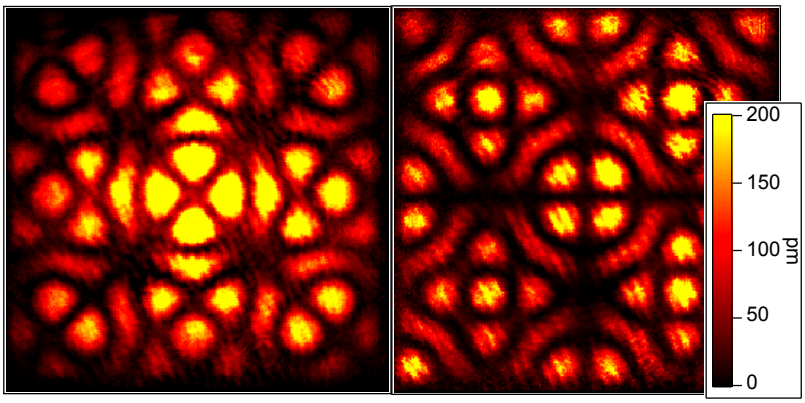


Figure 2.17: Interferometric images of the modal structures resulting from substrate-mediated coupling. (Left) hybridized mode corresponding to $\phi_{3,11} - \phi_{11,3}$,(Right) hybridized mode corresponding to $\phi_{10,6} + \phi_{6,10}$.

either $j \ll k$ or $j \gg k$, and higher $Q$s measured for $j \sim k$. The close agreement between our observations and the tunneling model, modified to include interference effects arising from substrate-induced hybridization (see Fig.[2.18(c)](blue circles), clarifies the role of anchor losses in determining the peak quality factors. Shown alongside is the calculation that does not take into account any hybridization (blue squares). The two predictions differ the most for modes of low symmetry. The hybridization suppresses the large variations of $Q$ with alternating parity observed in the original model. For large mode indices $j, k \gg 1$ with $j, k > \eta_\gamma \sqrt{j^2 + k^2}$, the suppressed parity dependence can be well approximated by the asymptotic expression,

$$Q^{-1}_{kj,asympt} \approx \frac{16\pi j^2 k^2}{\sqrt{j^2 + k^2}} \left[\frac{1}{j^4} + \frac{1}{k^4}\right] \frac{\rho_R h}{\rho_s L} \sum_\gamma \eta_\gamma^3 |u_\gamma^{(0)}|^2 \tag{2.41}$$

where the summation is now carried out over the various modes (surface acoustic, transverse, longitudinal and flexural waves) supported by the substrate. Here, $\eta_\gamma = c_R/c_\gamma \ll 1$ is the ratio of phase velocities in the membrane and the substrate. Note that, in this limit, the summation evaluates to a constant and the entire

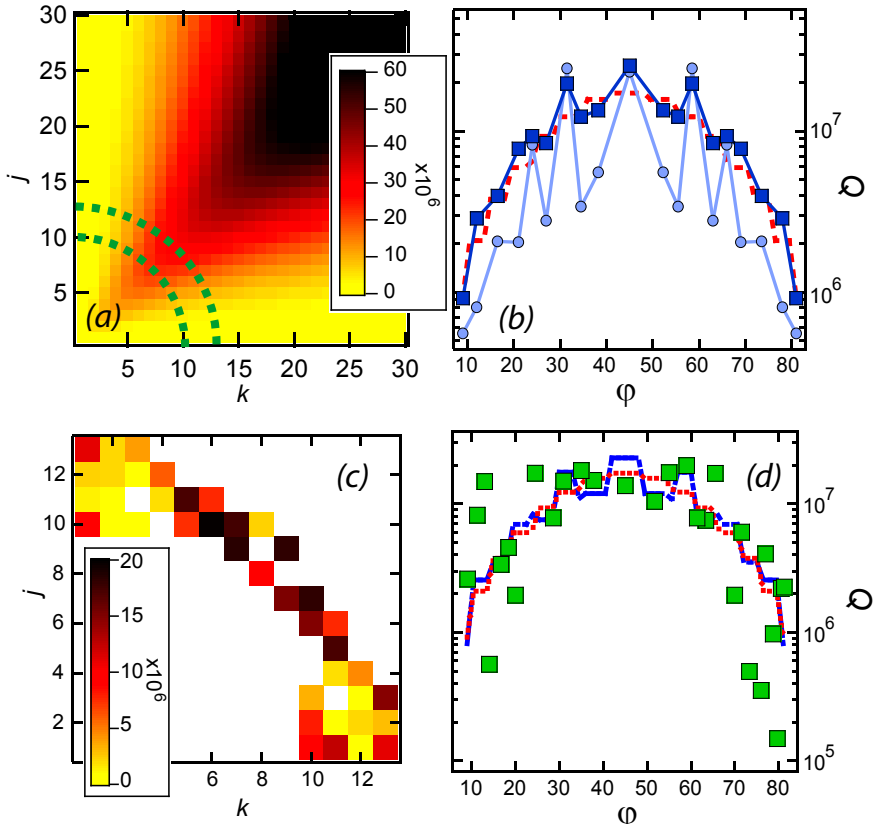


Figure 2.18: (a) Predicted quality factors versus mode indices based on asymptotic limits of our anchor loss model (b) Predicted quality factors versus $\phi = \arctan(j/k)$ for mode indices $(j^2+k^2)^{1/2} = 12$ with (without) substrate-mediated hybridization are shown as squares (•). Also shown is the asymptotic expression for the quality factors from our model (dashed line). (c) Measured $Q$s for mode indices indicated by the green arc in (a). (d) Comparison between the measured $Q$s in this arc and our predictions from (b).

mode index dependence is contained in the prefactor. This approximate expression is plotted alongside the exact calculation in Fig.[2.18(b)] (dashed red lines). To summarize, hybridization between degenerate resonator modes results in modal structures that are more symmetric than either of the constituent modes (see Fig.[2.17]). As can be seen in Fig.[2.18(b)], this results in an increased quality factor due to destructive interference of substrate modes radiated from the evenly

spaced antinodal segments around membrane periphery and a suppressed dependence of $Q$ on the parity of the resonator mode.

## 2.11 Conclusions

We extend previous work [9][17] to realize silicon nitride membrane resonators with quality factors of $5 \times 10^7$ and $f \times Q$ products of $1 \times 10^{14}$ Hz which to our knowledge, are the largest yet reported at room temperature for membrane resonators. We considered various possible limiting dissipation mechanisms in these resonators and identified radiation loss as the dominant source of dissipation. We have modelled this loss through a modification of the phonon-tunneling model[24] to include the effect of substrate induced hybridization, which accurately captures the modal dependence of the quality factors for the high mode numbers in the plateau regime.

We have thus realized a platform for the optomechanical cooling and quantum control of a mesoscopic mechanical resonator that meets all the criteria for ground state cooling and room temperature quantum control. Additionally, the ultrahigh quality factors have been realized in resonators with low mechanical frequencies (100's of kHz). These are as a result, ideally suited for various schemes to interface mechanical resonators with atomic gases or solid state spin systems, thereby allowing for the realization of hybrid quantum systems for sensor and transduction applications as well as for fundamental studies.

## 2.12 Appendix: Extraction of membrane curvature

We outline here the procedure for obtaining the curvature from the mode images measured through our dark field imaging technique. The images obtained are proportional to the $z$ displacement squared, as can be seen from neighbouring antinodes having the same intensity.

The images after background subtraction and normalization with the beam profile, with intensities given by $I(x, y)$ approximate to

$$I_{m,n}(x, y) \propto \sin^2\left(\frac{m\pi x}{L}\right) \sin^2\left(\frac{n\pi y}{L}\right) \tag{2.42}$$

for unhybridized modes. For hybridized modes, the corresponding intensities are,

$$I_{m,n,\pm} \propto \left(\sin\left(\frac{m\pi x}{L}\right) \sin\left(\frac{n\pi y}{L}\right) \pm \sin\left(\frac{n\pi x}{L}\right) \sin\left(\frac{m\pi y}{L}\right)\right)^2 \tag{2.43}$$

### Processing of the Images

To image a given mode, the resonator is driven on resonance with that mode to an amplitude of $\approx$ 200pm. The membrane (5 mm x 5 mm) is incident with an expanded beam with a waist of $\approx$ 3.5mm and a power of $\approx 10\mu$W. The reflected light from the membrane focusses on a spot of size $200\mu$m, to block out the DC component, and the resulting images are obtained with a camera exposure time of $1ms$. The distances were calibrated with a Michelson interferometer with a small spot size ($\approx 700\mu$m) focused at the center of the membrane.

A background image $I_{bkg}$ is obtained while the membrane is not driven. The beam profile ($I_{bp}$) of the beam is extracted by imaging at lower power with the dot removed.

The raw image obtained is rotated to align the square with the x and y axes. The

edge of the membrane can be clearly identified and the substrate portion of the image is cut out. The effect of the background and the beam profile is removed to obtain the an image proportional to the squared displacement $\tilde{z}^2$ using,

$$\tilde{z}^2(x,y) = \frac{I(x,y) - I_{bkg}(x,y)}{I_{bp}(x,y)} \tag{2.44}$$

An image proportional to the modulus of the displacement is therefore,

$$|\tilde{z}(x,y)| = \sqrt{\frac{I(x,y) - I_{bkg}(x,y)}{I_{bp}(x,y)}} \tag{2.45}$$

The sign of the displacement is not present in the image. However since the modes can be accurately identified (even for the case of the hybridized modes) this sign information can be added in by hand. We use the calculated displacement for the mode $z_{calc}(x,y)$ to extract the sign of the displacement ($\mathrm{Sign}\,[z_{calc}(x,y)]$). We multiply this with the measured $|\tilde{z}|$ to obtain,

$$\tilde{z}(x,y) = |\tilde{z}(x,y)| \times \mathrm{Sign}\,[z_{calc}(x,y)] \tag{2.46}$$

Fig.[2.19] shows modal images for the hybridized (6,10) mode before (left) and after (right) processing. The curvatures are now obtained from $\tilde{z}(x,y)$ as outlined in the next section.

## Extracting the curvature

The mean curvature of the membrane is given by

$$C(x,y) = \left(\frac{\partial^2 z}{\partial x^2} + \frac{\partial^2 z}{\partial y^2}\right) \tag{2.47}$$

For a membrane with a loss given by some loss modulus, the energy loss in the membrane is given as an integral of the mean curvature squared, over the membrane [25].

$$\Delta U \propto \int\int \left(\frac{\partial^2 z}{\partial x^2} + \frac{\partial^2 z}{\partial y^2}\right)^2 dxdy \tag{2.48}$$

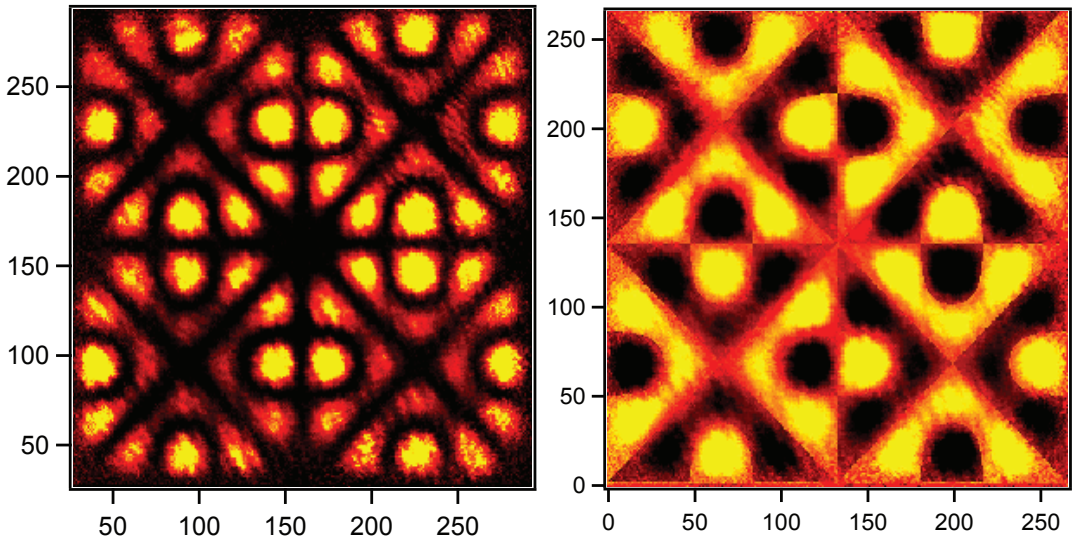


Figure 2.19: Image of mode $\phi_{(10,6)} - \phi_{(6,10)}$ before (left) and after (right) image processing.

Furthermore the energy stored in the membrane is proportional to the integral of the displacement squared

$$U = \frac{\rho h \omega^2}{2} \int \int z(x,y)^2 dxdy \tag{2.49}$$

The intrinsic loss limited curvature contribution to the Q is

$$Q = \frac{2\pi U}{\Delta U} \propto \frac{\int \int z(x,y)^2 dxdy}{\int \int \left( \frac{\partial^2 z}{\partial x^2} + \frac{\partial^2 z}{\partial y^2} \right)^2 dxdy} \tag{2.50}$$

The image is a $266 \times 266$ pixel grid. We replace the functions of coordinates, with functions of pixel index, i.e., $\tilde{z}(x,y) \rightarrow \tilde{z}[i,j]$. The derivatives in the above expression are extracted from $\tilde{z}$ by taking finite differences as below.

$$\begin{aligned} C(x,y) &= \left( \frac{\partial^2 \tilde{z}}{\partial x^2} + \frac{\partial^2 \tilde{z}}{\partial y^2} \right) \\ C[i,j] &= \frac{(\tilde{z}[i+d,j] + \tilde{z}[i-d,j] - 2\tilde{z}[i,j])}{d^2} + \frac{(\tilde{z}[i,j+d] + \tilde{z}[i,j-d] - 2\tilde{z}[i,j])}{d^2} \end{aligned}$$

A quick optimization of the smoothness of the extracted curvatures gave led to a choice of $d = 5$pix. The curvature contribution to the 1/Q, labelled $\tilde{C}$ is given by

$$\tilde{C} = \frac{\sum_{i,j} C[i,j]^2}{\sum_{i,j} \tilde{z}[i,j]^2} \tag{2.51}$$

The above quantity is a normalized curvature that does not depend on the magnitude of the z displacement of the membrane. A plot of the measured curvature extracted using the method described, versus the calculated curvature is shown in Fig.[2.20].

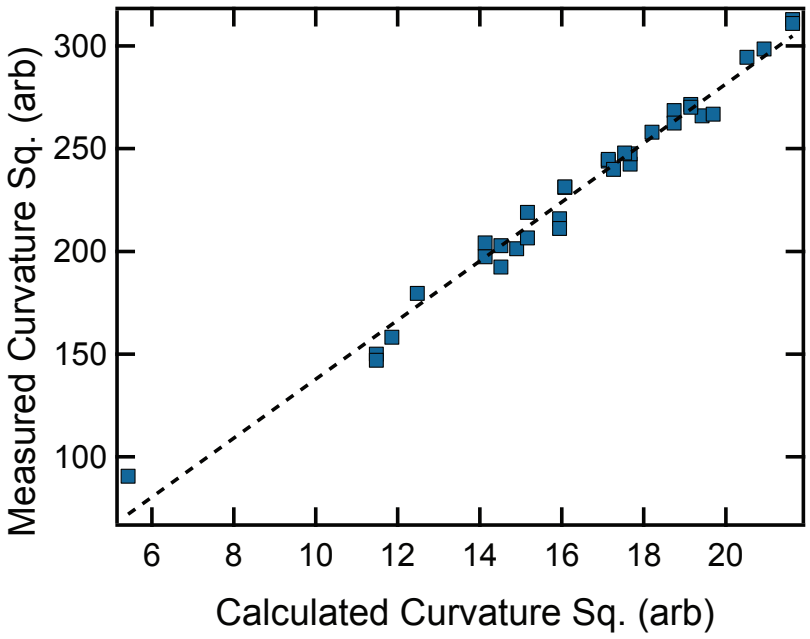


Figure 2.20: Plot of the measured membrane curvature versus the calculated curvature

CHAPTER 3

# ENGINEERING HIGH-Q RESONATORS THROUGH PHONONIC BANDGAP SUBSTRATES

## 3.1 Introduction

The previous chapter identified radiation loss as the dominant source of dissipation in stressed silicon nitride membrane resonators. In order to verify this hypothesis and mitigate radiation loss, we engineer devices with silicon nitride membranes suspended on silicon substrates, which are patterned to have an acoustic band gap[45, 46]. This chapter reports progress towards increasing the mechanical quality factors using this approach.

Materials with engineered phononic substructures are now being used for a variety of applications[47]. In optomechanics, there has been an upsurge of interest in such structures with the creation of optomechanical crystals[45], structures with simultaneous phononic and photonic bandgaps which allow for enhanced interactions between sound and light, in a small localized mode volume. In SiN membranes resonators on silicon substrates, apart from mitigation of radiation loss, acoustic bandgaps also play a role in reducing noise from the substrate modes, which poses limitations on optomechanical cooling and thermometry[48].

Acoustic bandgaps have previously been engineered in the supporting substrates of resonators similar to the ones we consider[46, 49], to achieve these ends[1]. Apart from the differences in fabrication methods, which we discuss below, a key dif-

[1]Ref.[46] saw a decrease in the density of substrate modes and a 30 dB suppression of propagating substrate modes, but no change in the mechanical quality factors. Ref.[49] saw the same mechanical quality factors in a bandgapped substrate, rigidly clamped to the support, as a substrate with no bandgap that is weakly coupled to the support, indirectly indicating mitigation of radiation loss. Neither however saw an increase in mechanical quality factors.

ference between these works and ours is that we engineer the devices to have a large number of membrane modes within the band gap and hence unambiguously identify the effect of the acoustic band gap on the quality factors of the modes of the mechanical resonator, measuring a quantitative difference in the mechanical quality factors inside and outside the acoustic band gap. We find that inside the acoustic bandgap, the typical radiation loss limited quality factor dependence with modal angle[8] is replaced by uniformly high quality factors for all the modes within the band gap, irrespective of the modal angle.

However, while we have therefore managed to increase the quality factors of several modes within the bandgap by more than two orders of magntitude, we have not yet measured an increase in the peak mechanical quality factors, which remains ongoing work. We discuss the possible reasons for this in Sec.[3.5].

We engineer the spatial modulation necessary for the creation of a phononic

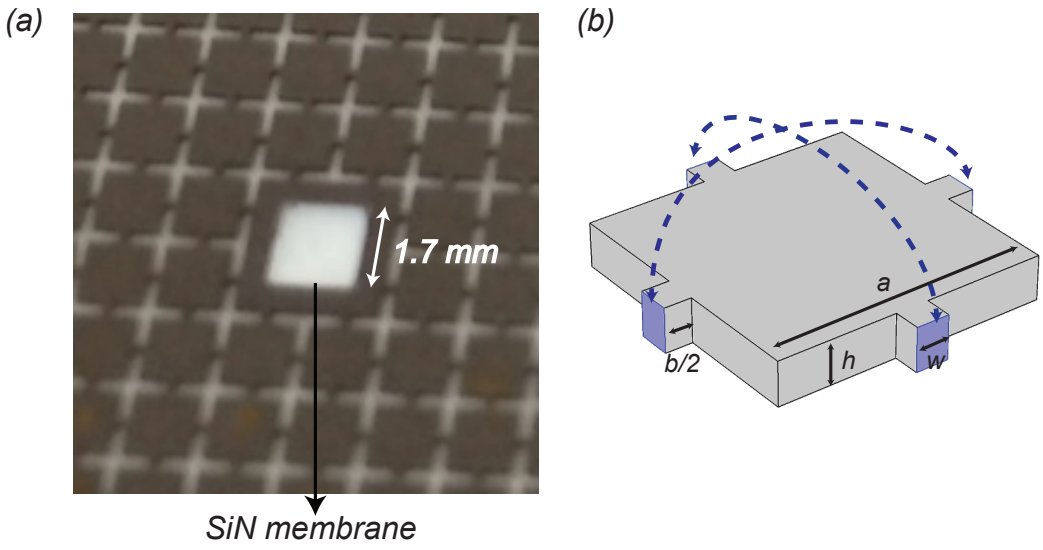


Figure 3.1: (a) Image of device with a bandgapped substrate (b) The unit cell of the band gap pattern for the device shown in (a). Dimensions; a = 1250 $\mu m$; b = 250 $\mu m$; w = 150 $\mu m$; h = 200 $\mu m$.

bandstructure by removing parts of the silicon from the sustrate. The patterns are laser cut on silicon substrates precoated with LPCVD nitride.[2] This is also unlike [46, 49], where deep reactive ion etching (DRIE) is used to create the pattern on the silicon substrate, before the LPCVD coating of the nitride.

The rest of this chapter is organized as follows. We describe the design of the bandgapped substrates, using the finite element package COMSOL, in Sec.[3.2]. In Sec.[3.3], we describe tests of the efficacy of the bandgap on prototype bandgapped silicon substrates[3], with no membrane, through interferometric measurements of displacements at different locations on the substrate. Lastly, we present the results of the dissipation measurements of membranes on substrates with acoustic bandgaps and conclude with a discussion of future steps to enhance the peak quality factors.

## 3.2 Design of phononic band gaps in the silicon substrate

The creation of a phononic band structure requires a periodic modulation of the density of the silicon, which is engineered through a periodic array of holes of specific shapes in the silicon substrate. The size of the unit cell $a$ is related to the frequency of the bandgap through $\nu_{bg} = \alpha\frac{v}{2a}$, where $v$ is the speed of sound in silicon and prefactor $\alpha$ depends on the geometry of the hole in the substrate. This implies that if one is interested in a band gap at low frequencies, of around a MHz, the unit cell size is $\sim$ a few mm. We pick a cross shaped hole, which for a given unit cell size is found to have a low value of $\alpha$[45].

[2]The membrane is protected from the debris of the laser cutting through a protective coating. The devices are fabricated by NORCADA inc.

[3]Fabricated by Yogesh Patil using the laser cutter at the group of A. K Lal, Electrical and Computer Engineering, Cornell University.

The cross shape retains the symmetry of a square and results in structures composed of square blocks of silicon, connected through tethers (See Fig.[3.1]). Each block can be thought of as an individual oscillator with modes. The connecting tethers result in a coupling between the different blocks. If one thinks of this in the sense of the tight binding model, one can see that the connecting tethers will result in the formation of phononic bands. As the tether width is decreased, the structure becomes less stiff. This reduces the speed of sound in the structure which in turn pushes down the frequency of the lower acoustic band. It also makes the high frequency optical band narrower and thereby increases the size of the phononic band gap[45]. In order that the final structure not be too fragile, and because of constraints from the laser cutting process, the tether width was constrained to a minimum of 150 $\mu m$.

Additionally the bandgap size was found to grow larger and decrease in frequency, through an increase in the thickness of the substrate. The substrate thickness was constrained to be 200 $\mu m$, because of the challenge of laser cutting the substrate, with a fragile membrane already grown on it. Given these constraints, the aspect ratio of the cross shaped hole was optimized to maximize the size of the bandgap.

### 3.2.1 COMSOL simulations of band structure

The band structure for a given unit cell is obtained in COMSOL by finding the eigenfrequencies and eigenmodes of the structure, while imposing Floquet periodic boundary conditions at the edge of the unit cell (see Fig.3.1(b)), i.e.,

$$\mathbf{d}(\vec{r}) = e^{i\vec{Q}.\vec{a}}.\mathbf{d}(\vec{r}+\vec{a})$$

where in the above, $\mathbf{d}$ is the displacement of a point $\vec{r}$ on the boundary of the unit cell, $\vec{a}$ is the lattice vector and $\vec{Q}$ is the wave vector corresponding to a given

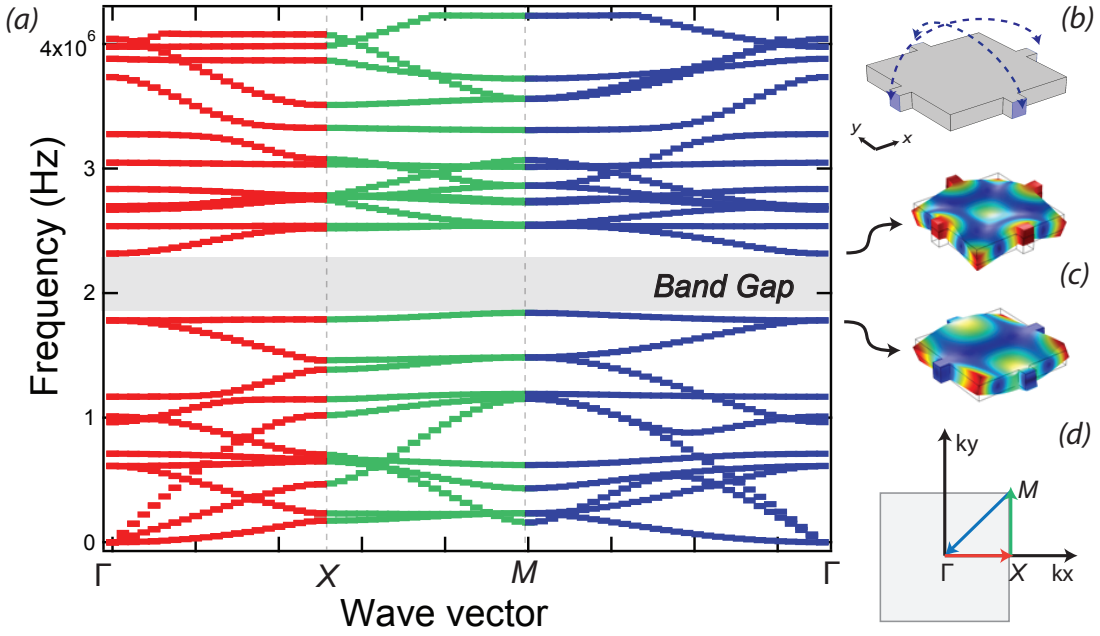


Figure 3.2: (a) Band structure obtained by solving for the eigenfrequencies of the structure shown (b), using Floquet periodic boundary conditions, with a bandgap near 2 MHz, with a width of 200 kHz. (b) Schematic of unit cell and periodic boundary conditions used. (c) The characteristic displacement profile of modes above and below the band gap at the $M$ point. (d) The closed loop in momentum space over which the eigenfrequency analysis is performed.

point in the Brillouin zone. We obtain the eigenfrequencies and eigenmodes of the structure while doing a parametric sweep of the wave vector $\vec{Q}$ across a closed loop in k space (see Fig.[3.2](d)) in order to obtain the band structure. Fig.[3.2](a) shows the band structure for the device shown in Fig.[3.1] with the gray shaded region indicating a bandgap with $\Delta \approx 200$ kHz at 2 MHz.

The geometry of the membrane and the bandgap structure is chosen such that there were at least two unit cells between the outer edge of the membrane and the outer edge of the substrate, with the bandgap at as low a frequency and as wide as possible. We chose the membrane dimensions to be such that there would be

enough membrane modes within the bandgap so as to obtain a meaningful quality factor versus modal angle ($\tan^{-1}(m/n)$) graph for the frequency band within the bandgap, in order to compare with the case outside the bandgap, for which we would expect to see the characteristic dependence that is a signature of radiation loss.

### 3.2.2 COMSOL simulations for a finite substrate

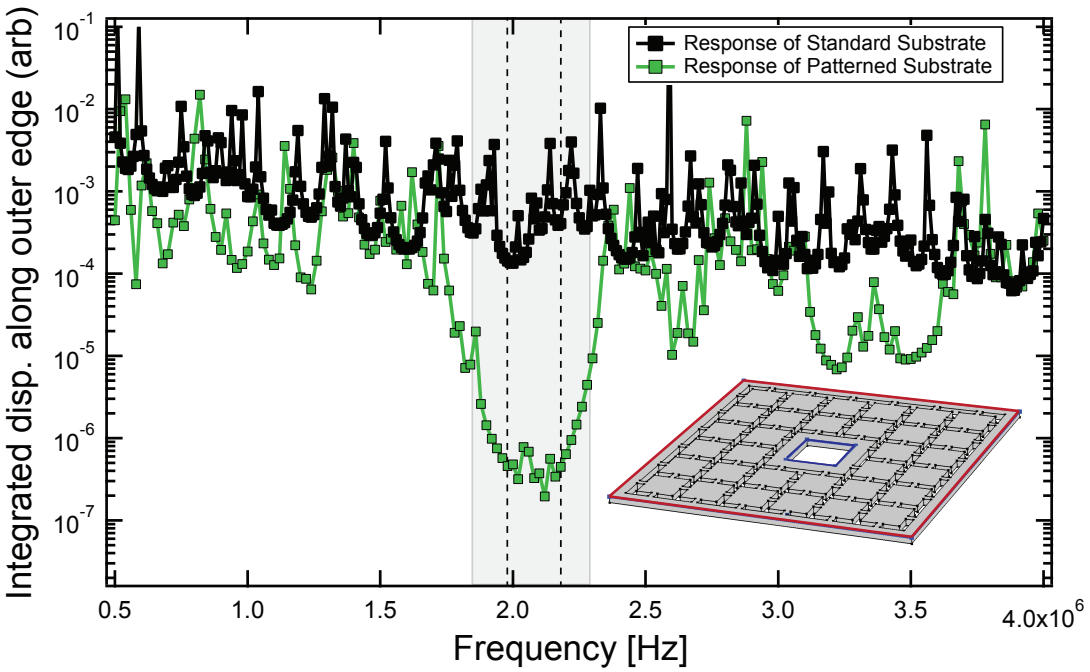


Figure 3.3: Response on the chip edge (red curve in inset) to a sinusoidal out of plane drive force on the inner membrane rim (blue curve in inset), mimicking the force from the membrane. The green points show the response of the bangpapped substrate while the black points show the corresponding response of a substrate with no band gap pattern. The gray region indicates the bandgap for the corresponding infinite system and the dashed black lines show the frequency band corresponding to a 30 dB suppression in the displacement.

The simulations described in the previous section are done for an infinite system. Given the large size of the unit cell required for band gaps at the relatively low frequencies of interest, we can fit only a few unit cells between the membrane edge and the edge of a standard 1 cm wide substrate chip. However, just 2 unit cells between the membrane boundary and the substrate edge are sufficient for the bandgap to have an effect on the energy transfer between the membrane and the substrate periphery. This was seen from simulations of a finite substrate with the band gap pattern between the membrane frame and the edge of the chip in which we actuate the substrate on the inner (membrane) rim with an out of plane force of fixed magnitude and varying frequency and compute the resulting displacement of the outer edge of the substrate. Fig.[3.3] (green points) shows the displacement of the outer edge of the substrate in such simulations on a finite substrate for the bandgap design for the device in Fig.[3.1(a)]. The suppression of the outer edge displacement coincides with the grey shaded region, which indicates the bandgap from the infinite system simulations in Fig.[3.2(a)]. No such suppression is seen for the standard non-patterned substrates (black points). The simulations produce a 30 dB reduction in the displacement inside the band gap, in comparison to that produced in an unpatterned substrate actuated at the same frequency, even for a design with two unit cells between the membrane edge and the edge of the substrate platform. The suppression as defined above, was seen to increase by 10 dB for each additional unit cell between the membrane edge and the outer substrate edge.

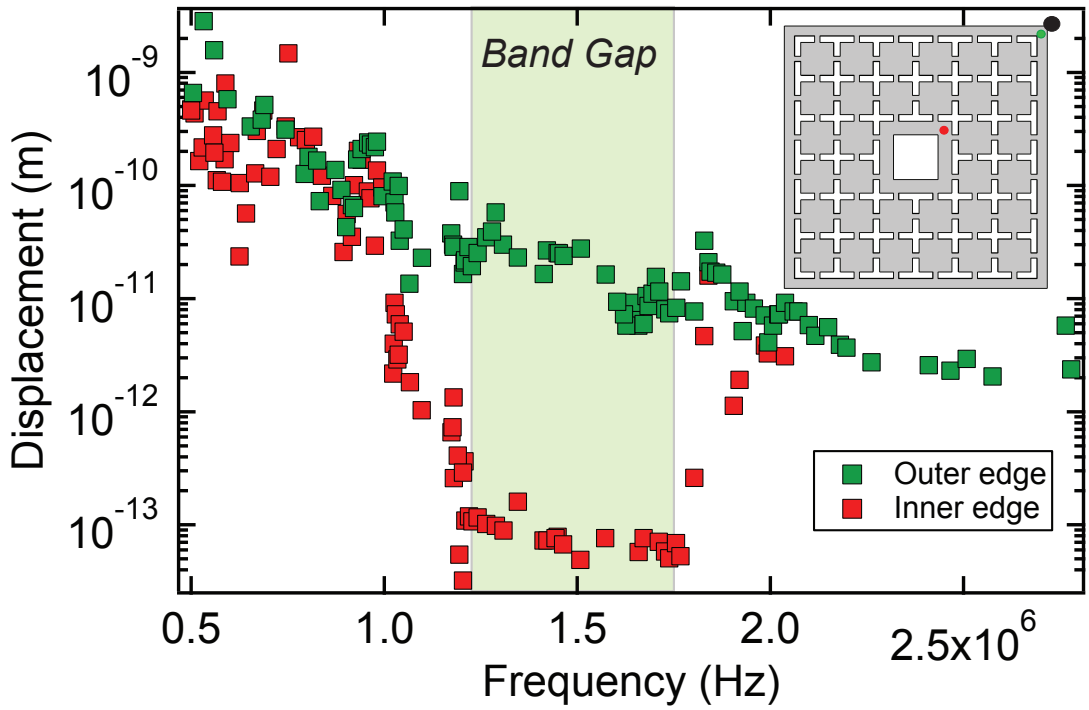


Figure 3.4: Bandgap substrate excited from an outer corner of the substrate (black spot) where it is attached to an aluminum mount and the underlying piezo. Resonances of the substrate are measured through interferometry using a beam focused to a spot near the outer corner (green spot in the inset schematic of substrate). The green points show the displacements measured at the outer corner (green spot) for a fixed piezo drive. The gradual decrease in the displacement is a result of the band width of piezo response. The red points are the corresponding displacements measured through a beam focused to a spot on the inner membrane rim of the substrate (spot marked in red). The displacement is reduced at the location of the bandgap for the corresponding infinite system (light green region).

## 3.3 Interferometric tests of bandgap efficacy

Before the fabrication of the final bandgapped devices, the efficacy of the band gap was tested through prototype band gap substrates with no membrane on them.

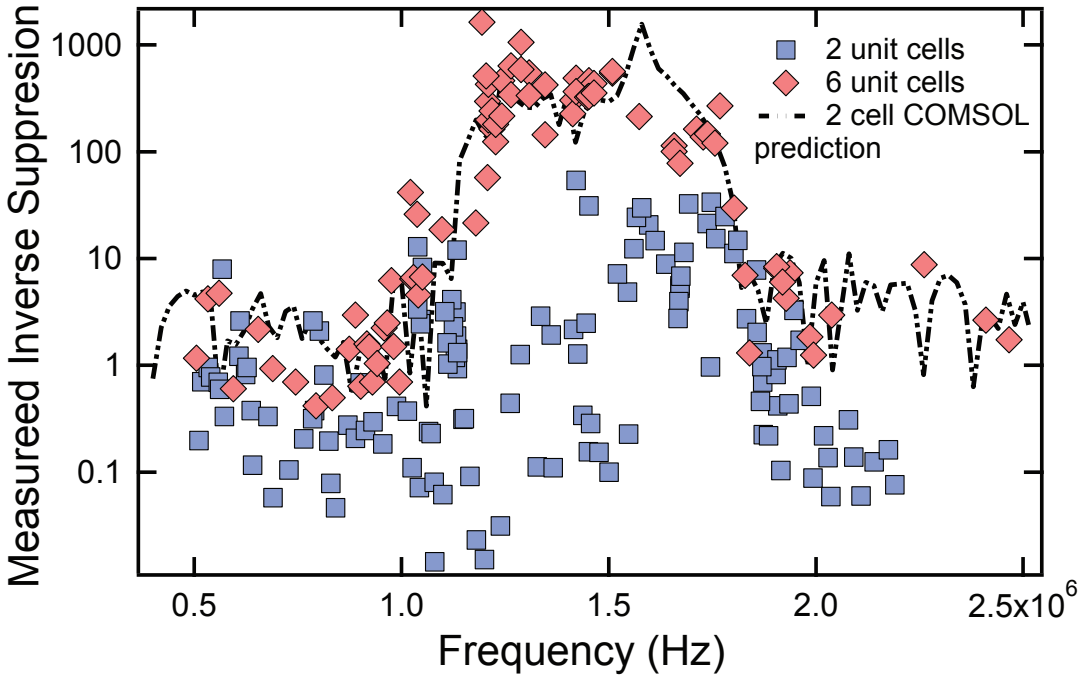


Figure 3.5: Measured displacement suppression for a design with two unit cells between the membrane and chip edge (light blue scales) and for the same design with six unit cells between the membrane and chip edge (light red diamonds).

The tests were conducted out of vacuum with the substrate mounted on an aluminum chuck attached to a ring piezo, similar to the mounting of the resonator chips described in Sec.[2.3]. The suppression of propagating substrate modes is extracted through interferometric measurements of the displacements, at different spot locations of a focused beam incident on the substrate. Fig.[3.4] shows one such measurement for a design with six unit cells between the inner membrane edge and the outer chip edge. The green squares show the displacements, for a fixed piezo drive voltage, of resonances of the substrate platform as measured on the outer edge of the substrate (green spot on the outer frame in the inset). The red squares are displacements as measured using the same piezo drive, with the

beam spot incident near the membrane edge of the substrate (red spot shown in the inset). The gradual decrease in amplitude for the green data points as a function of frequency is a result of the bandwidth of the piezo actuation. The displacement of the inner edge shows a pronounced dip at the location of the expected band gap (indicated by the shaded region).

We define the suppression of propagating modes resulting from the bandgap as the ratio of the displacement of the inner edge, to that on the outer edge which we extract through measurements such as the one described. Fig.[3.5] shows a plot of suppression obtained through such means for a design with 2 unit cells across the chip frame and one with 6 unit cells across the chip frame. A two unit cell design shows a displacement suppression of a factor of $\sim 30$, while a 6 unit cell design shows a displacements suppression of a factor of $\sim 500$ in the displacement.

While the extent of the suppression is lower by an order of magnitude, compared to the predictions of COMSOL, we were not too concerned by this on account of of the differences in the details of the measurements, and the simulations. In the simulations, the substrate was excited uniformly on the membrane edge and the displacements measured on the chip outer edge. In comparison, in the measurements, the substrate was excited on the outer edge along one corner. Additionally, a factor of 30 suppression in displacement, would correspond to a factor of 1000 suppression in the energy, which was deemed sufficient to have a substantial effect on the quality factors of the membrane resonances within the bandgap.

Morover, the frequency of the measured band gap is very close to that predicted by the simulations, as can be seen in Fig.[3.4,3.5].

## 3.4 Mechanical quality factors of membranes on bandgapped substrates

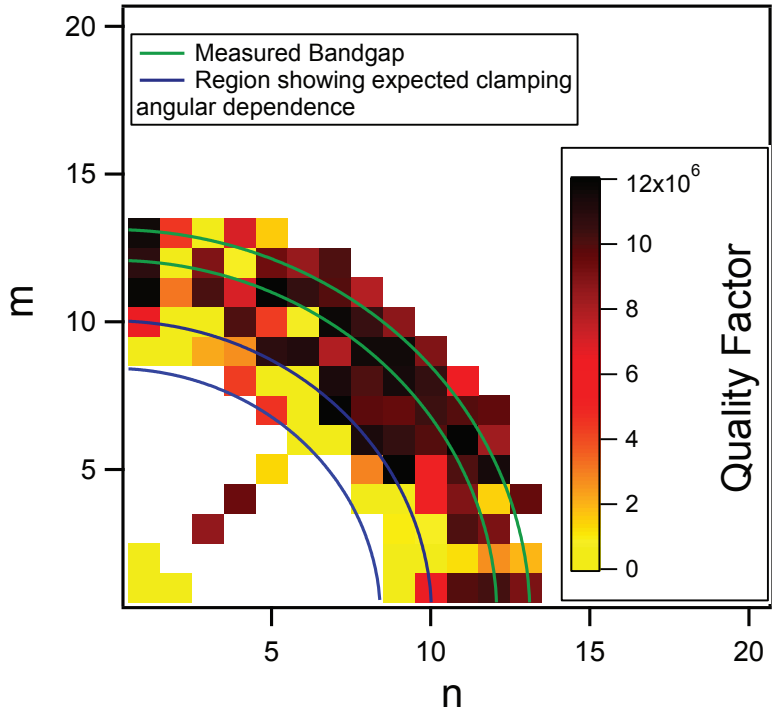


Figure 3.6: Quality factor versus mode index for a membrane on a bandgapped substrate with 2 unit cells between the inner membrane rim and outer chip frame. The band gap is over a 200 $kHz$ window between 1.9 - 2.1 MHz, indicated by the region between the green arcs.

In this section, we present the results of the measurements of the mechanical quality factors for membranes on bandgapped substrates. Our measurements of the quality factors use the setup described in Sec.[2.3], with the membrane displacements measured while in vacuum, using a Michelson interferometer. The quality factors are measured through ringdown measurements of the decay time, using a lock-in amplifier.

We first measured the quality factors for the 2 unit cell substrate. Fig.[3.6] shows the quality factor as a function of the mode index for this device. The mode indices can largely be uniquely identified based on the frequency, with the two near degenerate modes arbitrarily assigned with indices (m,n) and (n,m). In case of quadruple degeneracies, the mode indices were identified through modal images obtained using the technique described in Sec.[2.4]. The green arcs enclose the region of the measured band gap, obtained by sweeping the piezo drive, while monitoring the displacement near the membrane frame (analogous to the red point in Fig.[3.4]). The swept spectrum is shown in Fig.[3.7(b)(right axis)]. From the mode indices, we obtain a mode angle as before, through $\phi = \tan^{-1}\left(\frac{\mathrm{m}}{\mathrm{n}}\right)$.

A plot of the quality factors as a function of the mode angle, for the 2 unit cell device, are shown in Fig.[3.8]. The green squares indicate the modes within the band gap, while the blue diamonds indicate modes that are outside the bandgap (between the blue arcs in Fig.[3.6]). The latter show the typical radiation loss limited angular dependence, while the former, by comparison show quality factors that are independent of mode angle. This is a strong indication that radiation loss has been suppressed. The peak mechanical quality factors for this membrane were however not higher than those measured for the same membrane without a bandgap pattern, with the peak Q factor of the band gapped substrate being the additional red square in Fig.[3.7(a)].

Having not observed an increase in the peak quality factors, we began to question whether a measured suppression only a factor of $\sim 30$ in displacement, was responsible for the clamping of the peak quality factors. We therefore proceeded with measurements of a structure with more unit cells and enhanced suppression, the 6 unit cell design. The quality factors for the six unit cell device as a function of mode angle are shown in Fig.[3.9](This data is courtesy of Yogesh Patil).

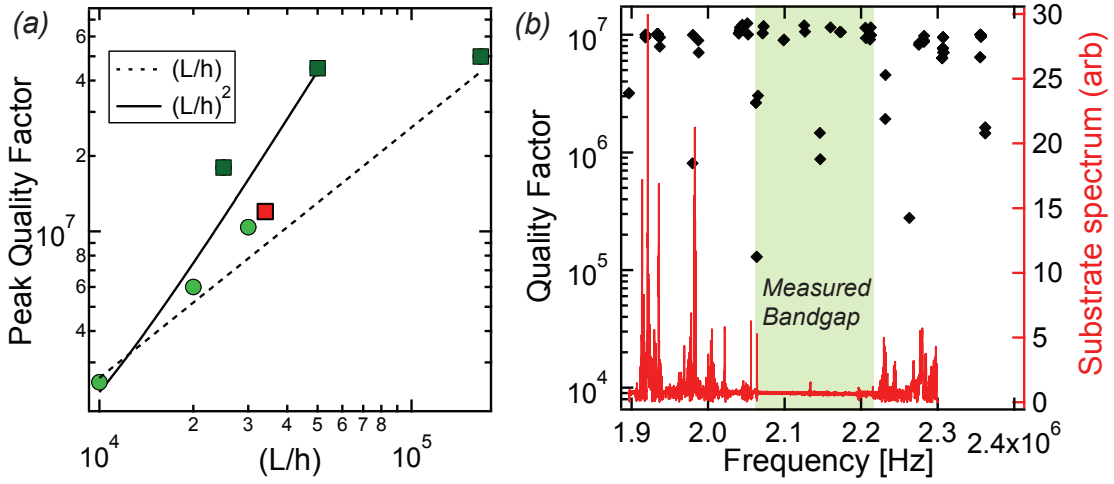


Figure 3.7: (a) Peak quality factor as a function of membrane aspect ratio including the peak quality factor for the bandgapped substrate (red square) (b) (Right axis) spectroscopic measurement of substrate displacement (red trace), (Left axis) quality factors in this frequency window (black diamonds)

Once again we see that the quality factor as a function of mode angle within the bandgap (black squares) has a flat modal dependence in comparison to the quality factor versus modal angle outside the band gap. Here the (light blue) diamonds are the quality factors of modes in an arc that is lower in frequency than the band gap, while the red circles indicate the quality factors of modes in a corresponding arc that is higher in frequency than the band gap, both showing a large variation with modal angle. Additionally, as further corroboration that radiation loss is suppressed within the bandgap, we see a pronounced modal angular dependence for the quality factor in the same frequency window (as the bandgap), for a device with no band gap pattern. This is shown in Fig.[3.10] (data taken by Yogesh Patil). The peak quality factors within the bandgap are still however about the same, about the same as for the 2 unit cell device.

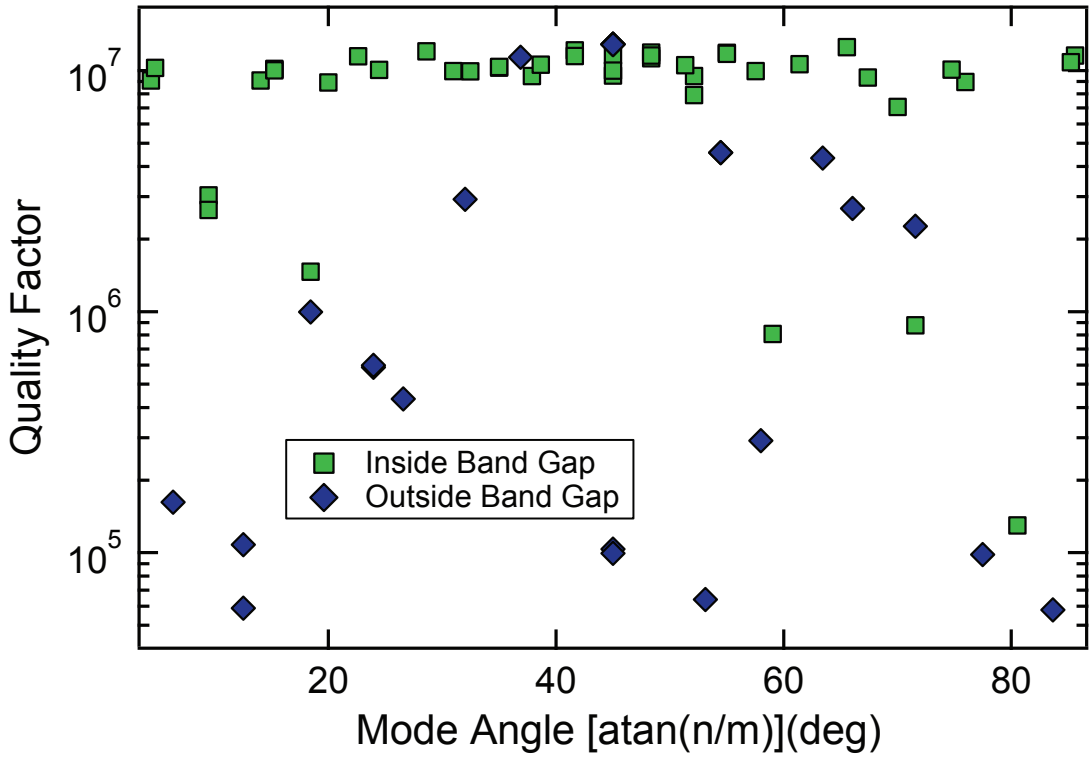


Figure 3.8: Quality factor versus mode angle for modes inside and outside the bandgap. The typical angular dependence of quality factors is not seen within the bandgap, indicating suppression of radiation loss.

## 3.5 Conclusions and future work

The quality factor measurements on the bandgapped substrate, indicate a suppression of radiation loss within the bandgap, as can be seen from the uniformly high quality factors measured as a function of modal angle. The increase in the quality factors is by almost two orders of magnitude for some of the modes within the bandgap.

The peak quality factors, i.e., the highest quality factors in a given frequency window have however not yet seen an increase, and remain clamped at values con-

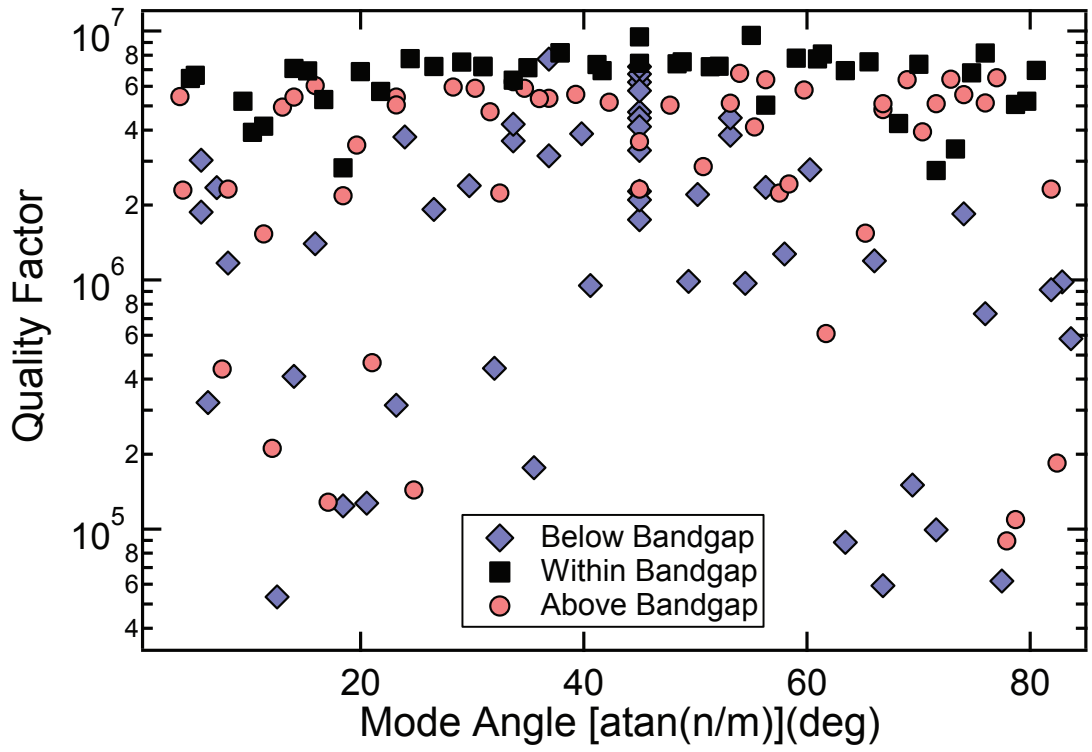


Figure 3.9: Quality factor versus mode angle for modes inside and outside the bandgap for the 6 unit cell device. The typical angular dependence of quality factors is not seen within the bandgap, indicating suppression of radiation loss.

sistent with that expected given the aspect ratio of the membrane.

If the quality factors of the membrane modes were still limited by radiation loss, we would not see a flat dependence of quality factor on modal angle, but would instead still see the arc dependence with much higher Qs. The fact that the quality factors of all the modes within the arc are limited to the same value suggests that they are limited though some other mechanism.

The naive explanation is that the quality factors are limited by intrinsic loss in the nitride, i.e., by curvature induced coupling near the edge of the membrane. This explanation is however at variance with the known dependence of the mechanical

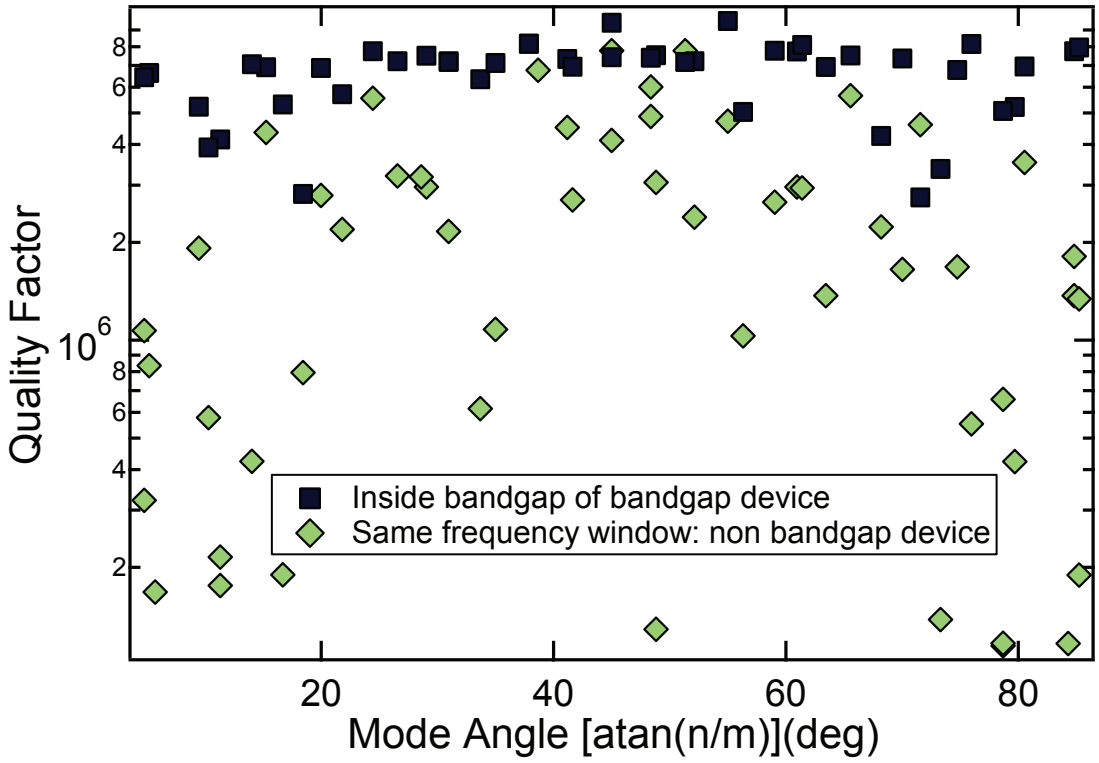


Figure 3.10: Quality factor versus mode angle inside the bandgap (black squares), compared with the quality factor versus mode angle for the same frequency modes on a device with same dimensions, but with no bandgap pattern.

quality factors of similar membranes on the thickness of the substrate[18].

The hypothesis being pursued stems from the observation that, while the bandgap is reasonably successful at suppressing propagating modes of the substrate platform, it still is the case that the bandgapped substrate has a large number of localized frame modes. These non propagating disturbances of the substrate have been seen in COMSOL simulations and through laser doppler vibrometry measurements of the substrate vibration profile. The coupling to this bath of frame modes might not have the same angular dependence that arises from the coupling to radiating modes. The coupling to such frame modes and subsequent decay of

the acoustic energy, through for instance, thermoelastic damping in the substrate platform might be accentuated by the small dimensions of the connecting structures in the bandgapped substrate. Tests of these hypotheses are being pursued through the fabrication of devices on thicker substrates, which are expected to show higher quality factors.

Additionally, new bandgap designs with a larger suppression of propagating modes and with fewer localized frame modes near the membrane rim are being pursued.

CHAPTER 4

# PARAMETRIC NONLINEAR MECHANICS IN HIGH Q MEMBRANE RESONATORS

## 4.1 Introduction

One of the outstanding goals of cavity optomechanics is the creation and manipulation of nonclassical states of mechanical degrees of freedom. The realization of such states would be an important step, both for fundamental studies of quantum physics and for metrology. Unlike in the case of radiation pressure cooling and detection of mechanical motion, this mandates a strong nonlinear interaction between the mechanical degrees of freedom. With this in mind, there have been numerous theoretical and experimental studies devoted to the realization of nonlinear interactions in mesoscopic mechanical resonators. Broadly, these schemes can be categorized into those that use optically mediated nonlinearities[21, 50, 51, 52], those that involve dispersive coupling to other auxiliary quantum systems[53, 54] and those that use various kinds of nonlinear mechanical interactions[55, 56, 57], a subset of which are parametric processes, where the nonlinear interaction involves a modulation of a parameter of the mechanical system, such as the spring constant, and, can be tuned in strength.

Parametric phenomena[58] have been extensively studied in mechanical resonators. They have been realized in single and coupled cantilever and torsional resonators[59, 60] and have been used for signal amplification[55] and thermomechanical squeezing[61, 62]. They have been recently used in coupled beam resonators for coherent manipulation of phonon populations[63, 56]. These are however typically studies that have been done in lossy mechanical systems that

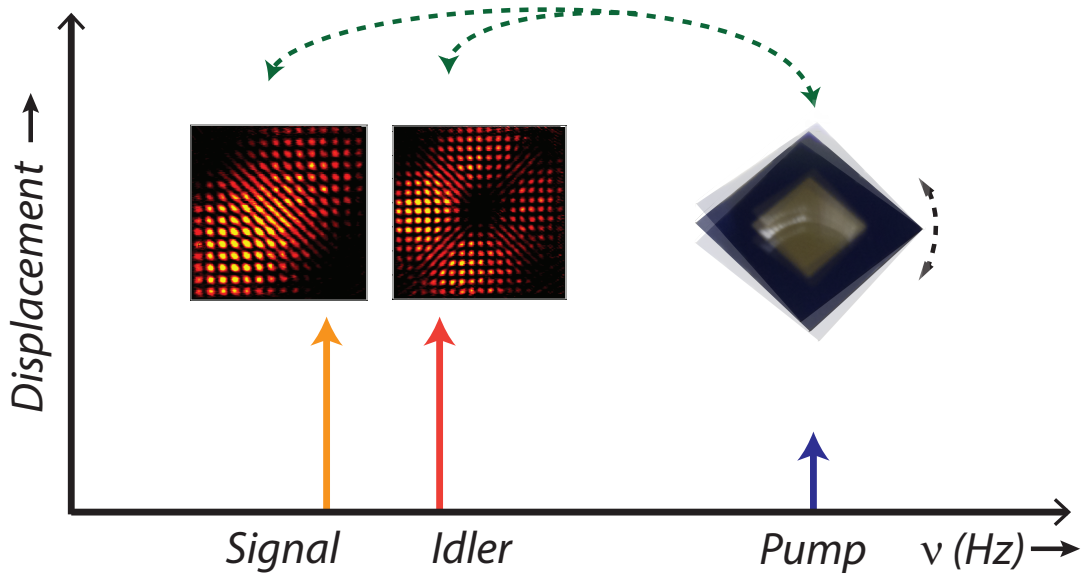


Figure 4.1: Schematic of a nondegenerate parametric amplifier, with drive at the pump leading to response at nondegenerate membrane modes (Signal and Idler)

are not compatible with optomechanical cooling and room temperature quantum control.

This chapter reports on the realization of a strong two-mode parametric nonlinearity between distinct modes of a single high stress silicon nitride membrane resonator suspended on a silicon substrate similar to the ones studied in Chapter 2, i.e., in a platform that has been demonstrated to be compatible with optomechanical cooling to the quantum regime and quantum limited detection. The nonlinear system realized is a nondegenerate parametric amplifier[59, 60], characterized by spontaneous self oscillation of two nondegenerate mechanical modes (signal and idler) when the membrane is piezo actuated at the sum frequency (pump) above a critical drive strength (For a schematic illustration, see Fig.4.1). Remarkably, the nonlinearity results in the onset of subharmonic response at pump drives as low as a few tens of *fm* despite the high degree of isolation from the environment.

This system is therefore very promising for the nonlinear manipulation of phononic fields, similar in spirit to studies in nonlinear optics.

This chapter is organized as follows. In Sec.[4.2], we describe a scheme to stabilize the frequency of the mechanical resonator, which because of the narrow linewidths of the resonator modes, is essential for a quantitative study of the parametric nonlinearity. This is followed in Sec.[4.3] by a description of the observed phenomenology including subharmonic generation at a threshold drive strength, the characteristic frequency dependence of the threshold (instability tongue) and the observation of hysteresis in the response of the signal and idler modes as function of the pump drive amplitude. In Sec.[4.4], we describe experiments to pinpoint the microscopic origin of the nonlinearity. Sec.[4.5] provides a description and solution of a model involving the coupling between the membrane modes and a third mode located at the pump. We compare the predictions of this model with experimental observations and find excellent agreement over many orders of magnitude in displacement.

This chapter, the first of two chapters on this subject, focuses on the identification of the appropriate model for the observed phenomena and discusses primarily the behavior seen above or at threshold. In chapter 5, we describe experiments done below threshold, where the system operates as a parametric amplifier. We demonstrate the parametric amplification of weak membrane mode signals by almost 30 dB and the phase dependence of the amplification of one of the modes (signal) in the presence of the parametric drive and a coherent drive for the other mode (idler) and realize dynamics akin to that seen in an optical parametric amplifiers. Lastly, we demonstrate the use of this parametric amplifier for thermomechanical noise squeezing.

## 4.2 Photothermal feedback control of mechanical frequencies

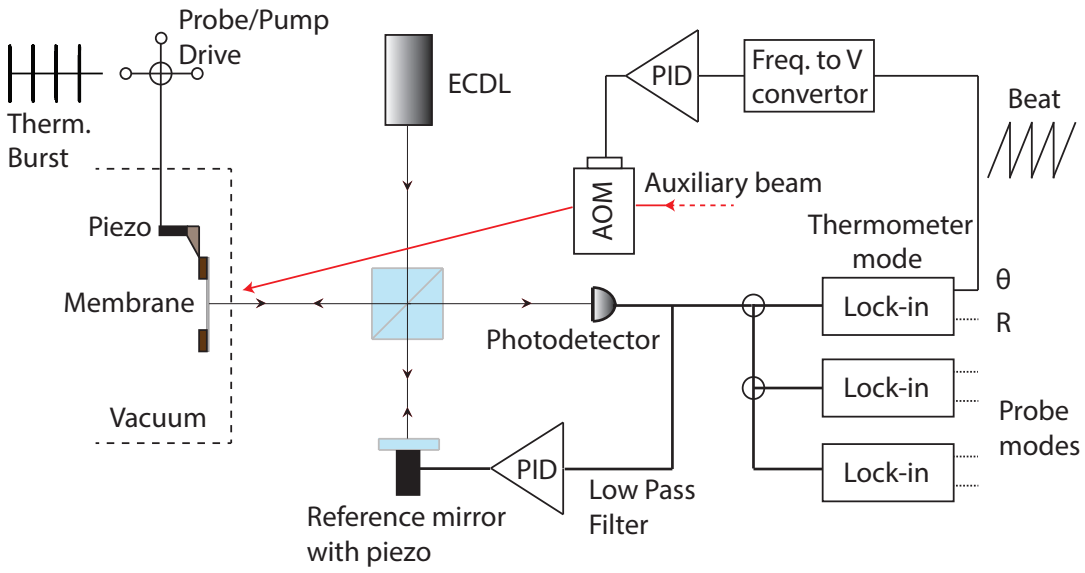


Figure 4.2: Schematic of the setup for studies of parametric nonlinearities. One of the modes of the membrane is used as a modal thermometer. The frequency of this mode is stabilized through photo thermal heating from an auxiliary beam, whose intensity is controlled to stabilize the frequency.

This study was performed on 100 nm thick, 5 mm wide high stress membranes, mounted on 10 mm wide, 500 $\mu m$ thick single crystal silicon substrates. These membranes show peak quality factors of $45 \times 10^6$ with the membrane mounting and assembly as previously described. The membrane is piezoactauted and displacements are measured using an actively stabilized Michelson interferometer with a sensitivity of 0.03 pm/$\sqrt{\text{Hz}}$ using a lock-in amplifier (Zurich Instruments: HF2LI).

The high quality factors of the modes of the resonator in question result in extremely narrow line widths (The linewidth of the 77 mode of the membrane, at

580 KHz and $Q = 30 \times 10^6$ is 20 mHz). The coefficient for the shift in frequency of this mode versus temperature is 120 mHz/mK. As a result, stabilization of the temperature of the membrane mount to 1 mK still results in a shift in frequency that is several times the linewidth of the mode, preventing a quantitative study of the nonlinear dynamics under investigation. This problem is circumvented by using one mode of the membrane as a modal thermometer[64], whose frequency we stabilize using the frequency shifts that are caused by photo thermal heating from an auxiliary laser beam.

The thermometer mode is actuated periodically through burst waveforms sent to the membrane piezo, actuating the membrane to amplitudes of $\sim 1 - 5$ pm. The beat frequency with a reference signal is measured using a lock-in amplifier. This beat frequency is converted to a voltage using a frequency to voltage converter circuit and this voltage serves as the measured voltage for an intensity stabilization circuit. This circuit controls the intensity of the auxiliary beam through an acousto-optic modulator. The auxiliary beam has a large waist (few mm), and an increase in the intensity of light results in heating of both the membrane and the substrate. (Schematic shown in Fig.4.2). The thermal expansion coefficient of silicon is larger than that of silicon nitride, and as a result, heating of the membrane and the substrate results in an effective increase in tension and a corresponding frequency increase. We use this feedback to stabilize the frequency of the thermometer mode (at 580 kHz) to 10 mHz over 100 s of observation.[1]

[1]Yogesh Patil improved the frequency stability by more than an order of magnitude by implementing a phase locked loop that directly locks the phase of a driven membrane mode, akin to the method used in [64]. This stabilization scheme is used in the experiments described in Chapter 5.

## 4.3 Phenomenology of subharmonic response of the SiN membrane

Nondegenerate parametric amplifier pairs were identified through frequency sweeps of the membrane piezo drive, while monitoring the photodetector response on a spectrum analyzer and looking for responses nearly subharmonic to the drive frequency. These subharmonic responses are identified as modes of the membrane through their large ringdown times and also through interferometric images of the membrane motion. Having identified a pair of modes that are parametrically coupled, we precisely measure the frequency of the membrane modes, typically to an accuracy of $< 10$ mHz. On driving at the sum frequency, and gradually increasing the drive voltage (proportional to the drive force), one finds that below a critical drive, there is no response at the signal and idler membrane mode frequencies, while above this threshold drive, the signal and idler modes self oscillate, with their amplitudes growing exponentially in time (Fig.4.3(a)). The growth rate increases with drive voltage, showing a linear dependence (Fig.4.3(b)). This growth rate extrapolates to zero at a critical voltage (force)- the instability threshold.

### 4.3.1 Instability tongue and hysteretic response

The threshold drive voltage is found to have a characteristic frequency dependence. The threshold is least when the drive is exactly at the sum frequency. When the drive is detuned from the sum frequency, the instability threshold voltage grows. While the frequency dependence of the instability threshold can be obtained through measurements of the growth rate versus the drive voltage and subsequent

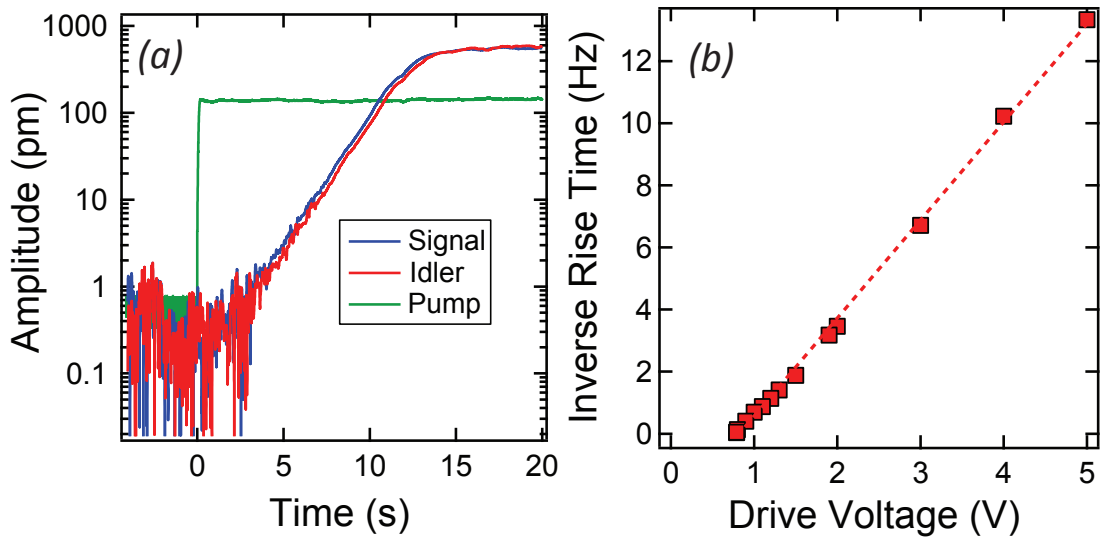


Figure 4.3: (a) Exponential growth of the amplitudes of the signal and idler modes as a function of time after turn on of the pump drive. The growth rate is obtained through a fit of the initial exponential rise. (b) Growth rate of modes approaches zero at a critical value of the drive amplitude; the instability threshold, with a functional dependence that is linear in the drive force.

extrapolation of the growth rate at different drive detunings ($\delta = \nu_d - \nu_1 - \nu_2$), a faster way of obtaining the same, and one that is less prone to errors from long term frequency drifts is by doing slow amplitude sweeps, i.e., at each detuning, the pump amplitude is swept linearly from $0 \rightarrow$ maximum value $\rightarrow 0$, while monitoring the modal response. The modal response to one such drive amplitude sweep is shown in Fig.[4.4(a)].

The response of the signal and idler modes to these amplitude sweeps is hysteretic (Fig.[4.4(b)]) with the onset of the modal response during the upsweep, occurring at a different voltage from the end of the signal and idler response during the down sweep of the drive amplitude. Fig.[4.4(a)] shows the pump amplitudes (arb. units) for the onset of the signal and idler response during the upsweep (orange squares) and the end of the signal and idler response during the down sweep (light blue

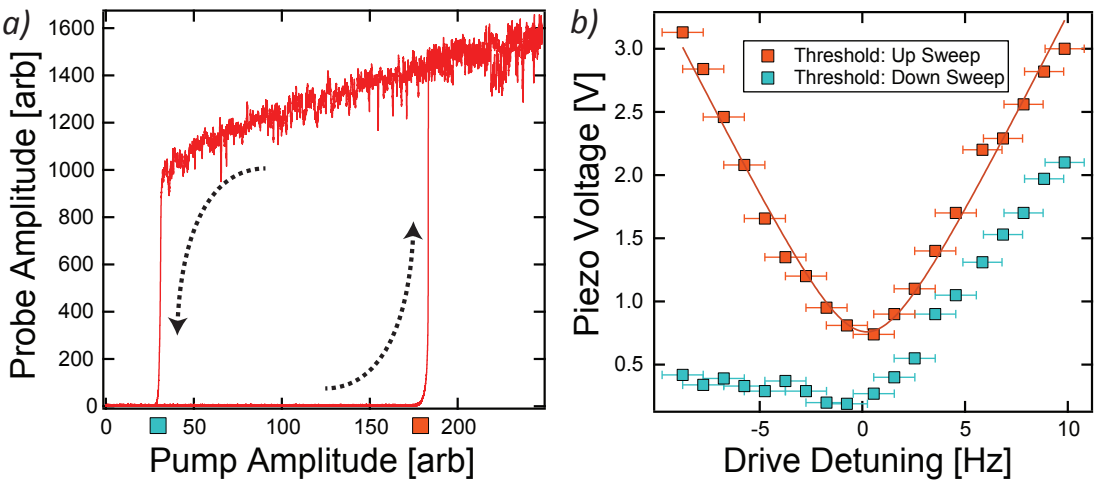


Figure 4.4: (a) Hysteretic response of the signal and idler modes as the parametric drive is linearly swept from $0 \rightarrow$ max value $\rightarrow 0$ at a detuning of $\delta_d = -7.5$ Hz. The hysteresis is largely present when the drive is red detuned from the parametric resonance (b) Frequency dependence of voltage of onset (fall) of signal and idler response during up (down) sweep. The onset of the response of the membrane modes occurs at the instability threshold which is fit to the form $\sqrt{1+\alpha\delta^2}$

squares) as a function of detuning from the parametric resonance. In Fig.[4.4(b)], the threshold for the onset of the down-conversion (upsweep) is fit to:

$$V_{th}(\delta) = V_0\sqrt{1+\alpha\delta^2} \tag{4.1}$$

$\alpha$ dictates the sharpness of the parametric resonance with a smaller $\alpha$ and a narrower resonance for membrane modes with higher quality factors. We show in a Sec.[4.5.1] that this is the predicted frequency dependence of the threshold of a nondegenerate parametric amplifier with a low Q mode situated at the pump. Furthermore, as is discussed futher in that section, the data agrees very well with the predicted $\alpha = \frac{4}{\left(\frac{\nu_i}{Q_i}+\frac{\nu_j}{Q_j}\right)^2}$, where $\nu_{i,j}$, $Q_{i,j}$ are the frequencies and the quality factors of the signal and idler modes. The fit in Fig.[4.4 (b)] is based on the measured value of the frequencies and the quality factors of the signal and idler modes with

only $V_0$ in Eqn.[4.1] free to vary, indicating remarkable agreement.

## 4.4 Investigation of the microscopic origin of mechanical nonlinearity

The observed phenomenon of parametric down-conversion is found to be quite ubiquitous, and we observe that most high Q mode pairs, when driven at a large enough drive amplitude exactly at their sum frequency, show parametric down-conversion. However, we observe that some of the mode pairs show down-conversion at remarkably low drive voltages/pump amplitudes. We address here the question of what is responsible for the efficient parametric coupling between the membrane modes that leads to the observed down-conversion. The scenarios that we consider are resonant enhancement arising from proximal modes of the membrane resonator and resonant enhancement arising from the modes of the substrate platform. The former is ruled out based on the experimental evidence presented in Sec.[4.4.1]. The latter is discussed in Sec.[4.4.2]. We have so far found no spectroscopic evidence in support of this claim. However, this cannot be ruled out because of the existence of substrate modes that our detection is insensitive to, i.e., shear modes of the substrate platform (see Fig.[4.6(b)]).

The existence of a third low Q mode, at the pump frequency is suggested by the observation of a strong dependence of the quality factor of the signal mode on the idler mode amplitude, as we discuss in Sec.[4.4.3]. The shift in the quality factor of the signal mode is a result of coupling to the highly lossy mode, located near the pump, through the amplitude of the idler.

Furthermore, as is discussed there, the correlation between the quality factor

shift and the down-conversion provides strong evidence that the parametric down-conversion is explained by a coupling of the form $H_{ij} = -gx_i x_j X_S$, where $x_{i,j}$ are the displacements of the membrane mode, while $X_S$ is the displacement of the substrate mode.

We detail the above arguments in what follows before solving for the predictions of this model and comparing them closely with the experimental results.

### 4.4.1 Mediation of the parametric coupling by a mode of the membrane

We study the role of membrane modes near the parametric resonance (pump frequency) by studying specific test cases of the down-conversion nonlinearity while simultaneously spectroscopically monitoring the membrane modes near the pump drive. In Fig.4.5, we monitor the membrane response to a small piezo sweep drive in the vicinity of 2 parametric resonances (a) and (b). We identify all the membrane modes (Modes (31,34), (1,46) and their degenerate partners) in a 1 KHz frequency window near parametric resonances. Parametric resonance (a) shows a low down-conversion threshold (half the parametric resonance threshold of (b)) despite being several tens of linewidths away from the nearest membrane mode. (b) and (c) both correspond to the precise sum frequencies of membrane modes $(\nu_5, \nu_6)$ and $(\nu_5, \nu_7)$. Parametric resonance (b) shows a low down-conversion threshold while (c), just as proximate to a membrane mode as (b), does not show any down-conversion for even the highest drive voltages (300 times larger than the down-conversion threshold for (b)).

Additionally, we find that there is no change in the frequencies/response amplitudes of the proximate membrane modes as the drives at (a) and (b) are increased

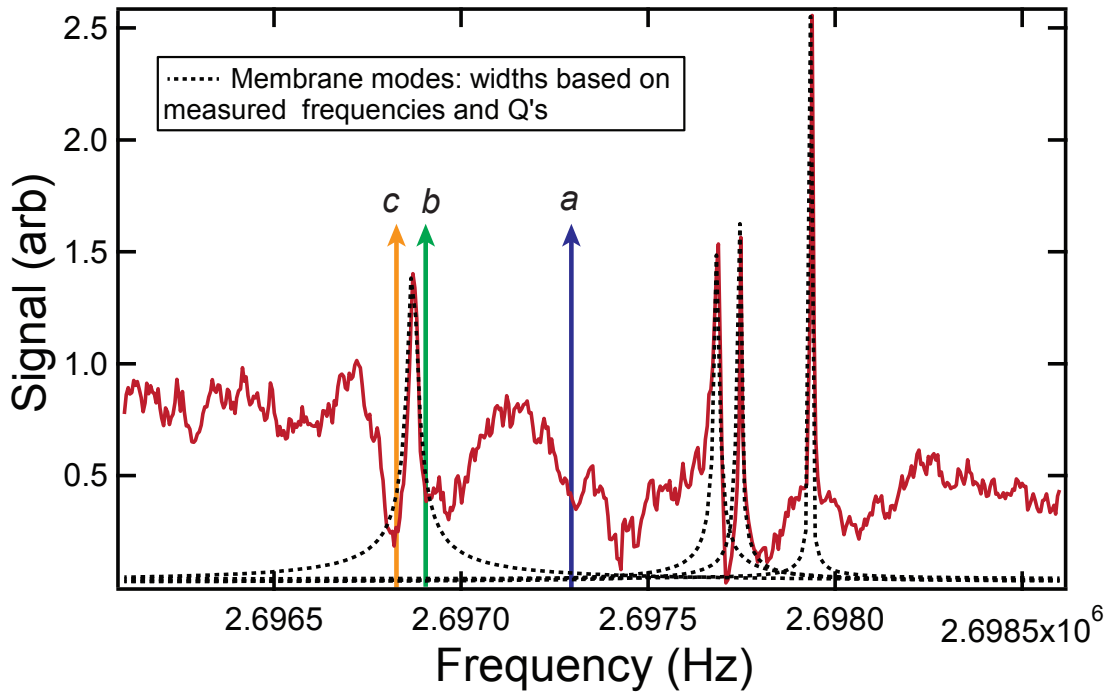


Figure 4.5: Spectroscopy of membrane modes near parametric resonances (a) and (b), indicated by arrows. All the membrane modes within the window are identified, with Lorentzian fits (dashed black curves) based on measured frequencies and quality factors. Parametric resonance (a $= \nu_1 + \nu_2$), showing the lowest parametric resonance threshold is several tens of linewidths away from the nearest membrane mode. ($b = \nu_5 + \nu_6$) also shows a low parametric resonance threshold while (c $= \nu_6 + \nu_7$) does not show down-conversion even at the highest drive voltages, despite being as proximate to a membrane mode as (b).

above the instability threshold, indicating further that membrane modes proximate to the parametric resonance play no role in the down-conversion.

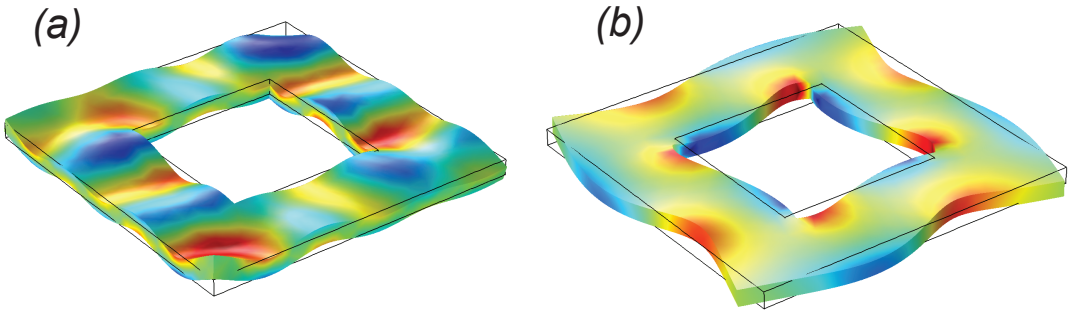


Figure 4.6: Modes of the substrate platform (a) Flexural mode at 537 kHz (b) Shear mode at 470 kHz.

### 4.4.2 Mediation of the parametric coupling by a mode of the substrate

The silicon substrate on which the membrane is mounted supports a host of modes (Fig.[4.6]). These modes consist of flexural modes with vibrations out of the plane which can be detected spectroscopically and shear modes with in plane vibrations. We envisage that, when the substrate is driven on resonance with these modes, there will be easy transfer of energy to the modes of the membrane. In order to detect if there is a flexural substrate mode at the location of the parametric pump, we pointed the interferometer beam on the substrate. We did not detect any flexural modes in the frequency windows where we saw the parametric resonances, even at the largest piezo drive (At the largest piezo drive, the motion due to a possible flexural mode was $< 300$ fm. The noise floor was higher by a factor of 10 on account of the poor reflectivity of silicon substrates with 100 nm coating of SiN, at 794 nm of $\sim 3$ %). While we have not yet found direct spectroscopic evidence for modes of the substrate playing a role in mediating the nonlinearity, the interferometer is insensitive to in-plane vibrations and cannot be used to detect a host of substrate

modes, even in principle. We have possibly only ruled out flexural modes playing a role in the nonlinearity. Furthermore, we find strong indirect evidence of the mediation of the nonlinearity through a substrate excitation, as is detailed in the following sections.

### 4.4.3 Correlation between down-conversion threshold and quality factor shift

Pairs of signal and idler modes showing a low amplitude down-conversion nonlinearity also show a curious decrease in quality factor when the other mode is driven. Fig.4.7 shows the normalized quality factor of the signal mode as a function of the drive amplitude of the idler mode for many pairs of membrane modes. The displacement of the idler mode is calibrated using the measured thermal motion, with the detected RMS value scaled to that which is theoretically expected for thermal motion at $T = 300$ K. The RMS value of the thermal motion is typically measured over 100 s and shows a 10 % variation across iterations.

As is detailed in the next section, this shift in the quality factor is most easily explained through the coupling between the membrane modes and a low Q mode at the pump frequency, through a coupling in the Hamiltonian of the form $H_{ij} = g x_i x_j X_S$, where $x_{i,j}$ and $X_S$ are respectively, the displacements of the membrane modes(i,j) and the third mode located at the pump frequency(S). Driving one of the modes to a large amplitude couples the other membrane mode (idler) with the mode at the pump and pulls its quality factor. The predicted functional form for the Quality factor shift is derived in the next section and given by Eqn.[4.45]. We use this to fit the quality factor versus amplitude curves in Fig.[4.7]. The fit

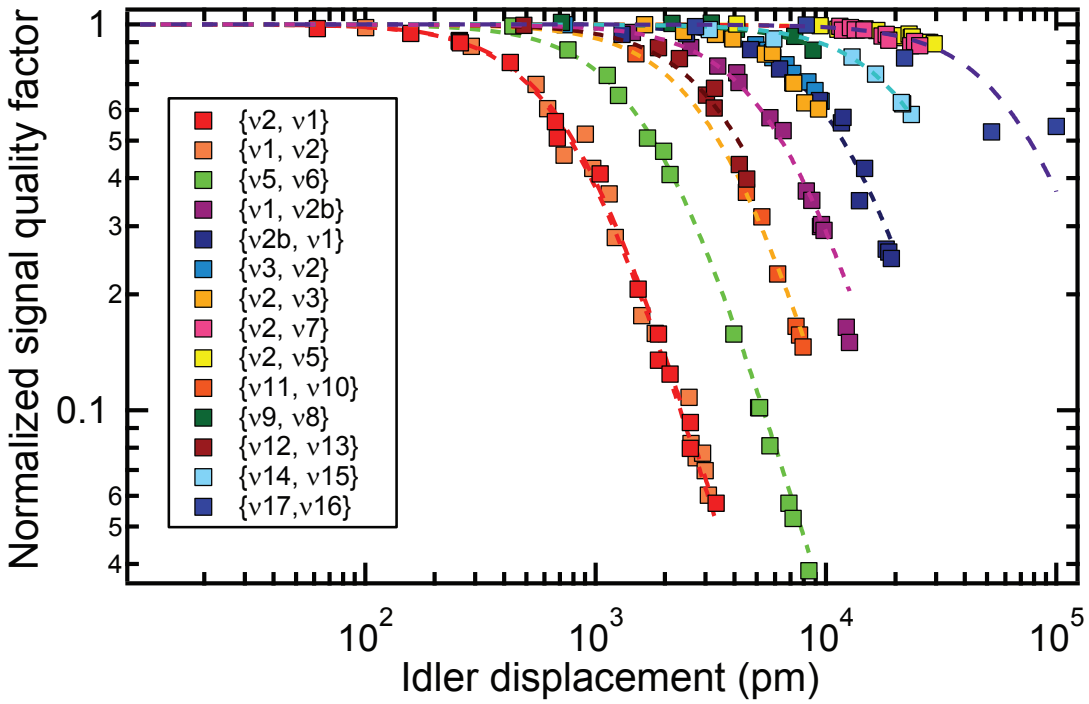


Figure 4.7: Normalized quality factor of the signal as a function of the amplitude that the idler mode is driven to. The quality factor of the signal mode is normalized with its bare value, with the idler undriven. The functional dependence of the normalized signal mode quality factor as function of the idler amplitude is fit to Eqn.4.45. Some mode pairs showing a much larger shift than others. The displacement of the idler mode is calibrated by scaling the measured RMS thermal motion to the theoretically expected thermal motion at $T = 300$ K.

takes as input, the measured quality factor of the signal mode $Q_i$, the quality factor of the putative pump mode $Q_S$, and the parameter $\xi$, which is a length scale that parametrizes the strength of the coupling. We extract $\xi$ from the fits assuming a fixed value for the quality factor for the putative pump mode ($Q_p = 5000$). $\xi$ is correlated with the parametric instability threshold for the mode pairs as can be seen in Fig.[4.8], where the dashed black line is a power law with exponent of one, drawn as a guide to the eye. The instability threshold voltage is converted to a

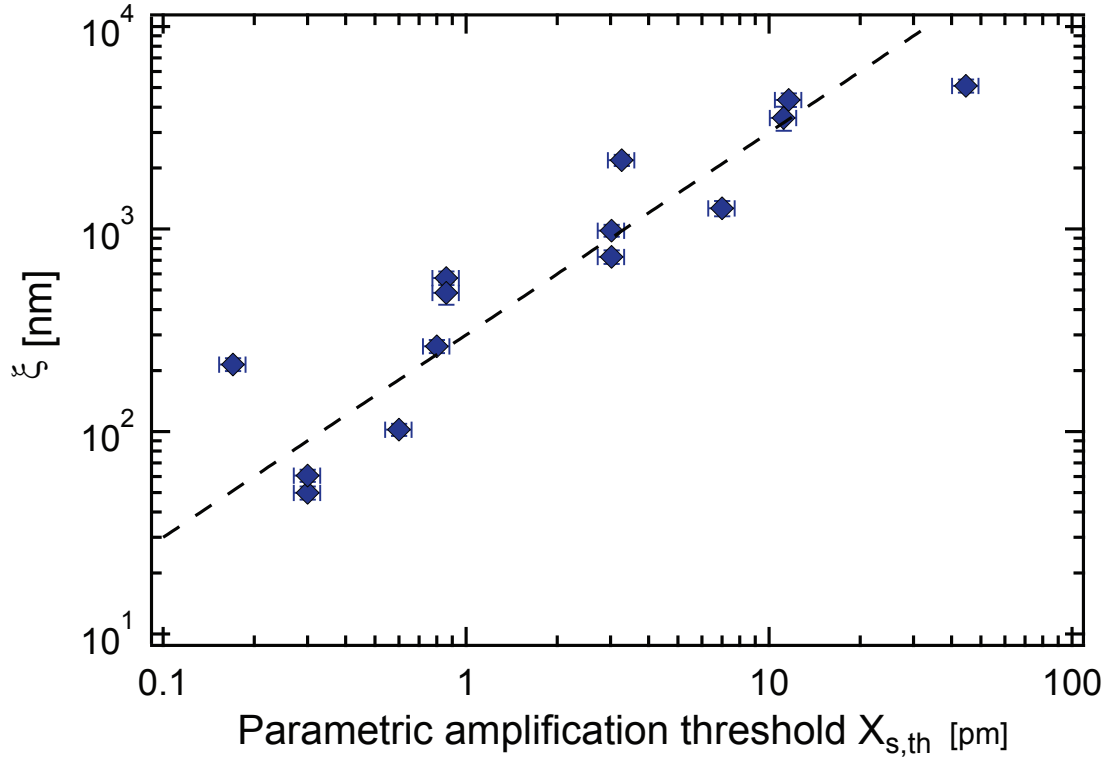


Figure 4.8: Correlation between length scale ($\xi$) parametrizing the quality factor shift of the signal mode with the idler drive and the threshold substrate displacement for parametric down-conversion. The dashed black line is a power law with an exponent of 1.

threshold displacement by monitoring the response of the membrane as a function of the drive voltage far away from a mode of the membrane, but close in frequency to the parametric resonance to calibrate out the frequency dependence of the piezo response.

The approximate linear relationship between $\xi$ and the threshold displacement, arises from the fact that they are both inversely related to the strength of the two-mode coupling $g$ and provides strong support to the model. A model with just two parametric coupled modes, without a third mode located at the pump frequency, will also show Q pulling arising from the coupling between the two membrane

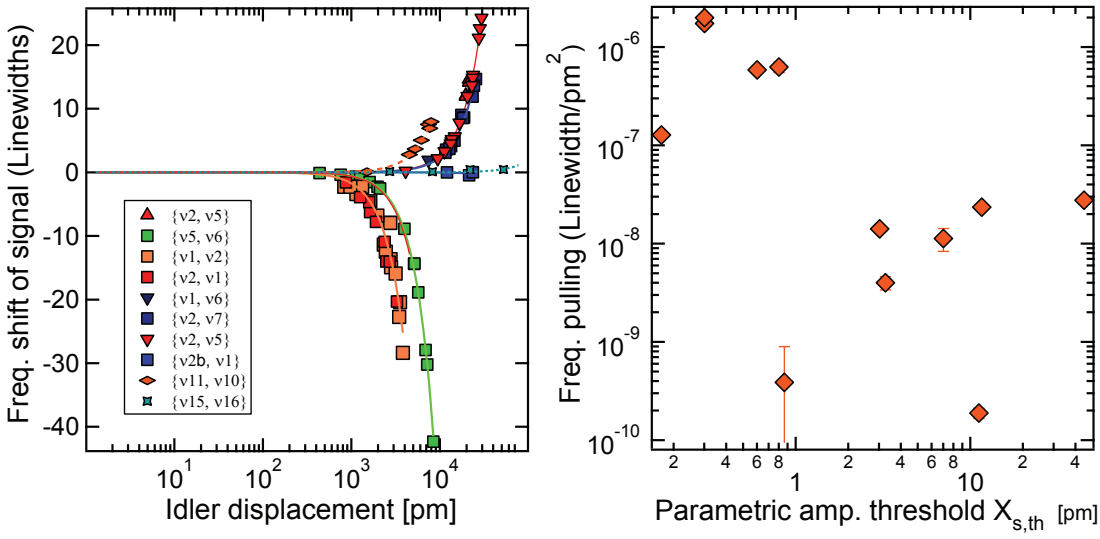


Figure 4.9: (a) Frequency pulling of the signal mode as a function of the drive amplitude of the idler (b) Plot of frequency shift of pairs of membrane modes and their corresponding parametric instability thresholds.

modes. This Q pulling arising from the coupling between the signal and the idler does not lead to the dramatic quality factor shift, by over two orders of magnitude, that we see for membrane modes of comparable damping rates.

In addition to a shift in the quality factor of the signal mode as a function of the idler amplitude, there is also, in addition, a frequency shift of the signal mode (Fig.[4.9(a)]). This frequency shift shows a quadratic dependence on the amplitude of the idler mode. Unlike the quality factor shift, the frequency shift does not show as pronounced a correlation with the parametric instability threshold (Fig.[4.9(b)]).

## 4.5 Nondegenerate parametric amplifier: Model

We now examine a model of two resonator modes, parametrically coupled to each other through a mode at the sum frequency, and quantitatively compare its predictions with the experimental observations of the previous section. The parametrically coupled membrane modes (i,j) and the pump substrate mode (S) have frequencies $\omega_{i,j,S}$, damping rates $\gamma_{i,j,S}$ and are described by displacements $x_{i,j,S}$. We think of the pump mode as a mode of the substrate with a low quality factor ($Q_S \sim 10^3$-$10^4$). The two resonator modes are modes of the SiN membrane with $Q_{i,j} \sim 10^7$, leading to subhertz damping rates for the MHz frequencies of the modes under consideration. The term in the Hamiltonian responsible for the coupling between the modes is considered to be of the form,

$$H_{ij} = -g x_i x_j X_S \tag{4.2}$$

We assume for simplicity that $\omega_S = \omega_i + \omega_j$. The equation of motion (EOM) for the different modes are,

$$\ddot{x}_i + \gamma_i \dot{x}_i + \omega_i^2 x_i = \frac{f_i(t)}{m_i} + \frac{g}{m_i} x_j X_S \tag{4.3}$$

$$\ddot{x}_j + \gamma_j \dot{x}_j + \omega_j^2 x_2 = \frac{f_j(t)}{m_j} + \frac{g}{m_j} x_i X_S \tag{4.4}$$

$$\ddot{X}_S + \gamma_S \dot{X}_S + \omega_S^2 X_S = \frac{f_S(t)}{m_S} + \frac{g}{m_S} x_i x_j \tag{4.5}$$

If we are not interested in the dynamics of the pump mode, we can obtain the limit of $X_S$ being a non-dynamical field through a suitable choice of $m_S, \gamma_S$ & $f_S$. We are going to be considering forces $f_k$ that are going to be nearly resonant with the oscillators $\omega_i$. We therefore rewrite

$$f_k(t) = \Re[F_k(t) e^{i\omega_k t}] \tag{4.6}$$

Note that $F_k(t)$ is complex and is allowed to vary slowly in time. We also complexify the displacements, i.e.,

$$x_k \;=\; \Re[z_k] \quad k \in [i, j, S]$$

The equations of motion now become,

$$\ddot{z}_i + \gamma_i \dot{z}_i + \omega_i^2 z_i \;=\; \frac{F_i e^{i\omega_i t}}{m_i} + \frac{g}{2m_i}\left(Z_S z_j^* + \cancel{Z_S z_j}\right) \tag{4.7}$$

$$\ddot{z}_j + \gamma_j \dot{z}_j + \omega_j^2 z_j \;=\; \frac{F_j e^{i\omega_i t}}{m_j} + \frac{g}{2m_j}\left(Z_S z_i^* + \cancel{Z_S z_i}\right) \tag{4.8}$$

$$\ddot{Z}_S + \gamma_S \dot{Z}_S + \omega_S^2 Z_S \;=\; \frac{F_S e^{i\omega_S t}}{m_S} + \frac{g}{2m_S}\left(z_i z_j + \cancel{z_i z_j^*}\right) \tag{4.9}$$

We solve the equation above with an ansatz of the form,

$$z_k = A_k(t) e^{i\omega_k t} \tag{4.10}$$

where the $A_k$'s are complex displacements which also encode the phase of the response. They vary slowly in time, over time scales set by the coupling and the decay times of the modes. We drop terms in Eqn.[4.7] of the form $Z_S z_j$ since they are off resonant with the membrane mode by $\approx \omega_S$, akin to the rotating wave approximation. Rewriting Eqn.[4.7,4.8] in terms of $A_k$ gives,

$$\cancel{\ddot{A}_{i,j}} + (2i\omega_{i,j} + \cancel{\gamma_{i,j}})\dot{A}_{i,j} + i\gamma_i\omega_i A_{i,j} = \frac{F_{i,j}}{m_i} + \frac{g}{2m_{i,j}} A_S^* A_{j,i} \tag{4.11}$$

We ignore the $\ddot{A}_{i,j}$ & $\gamma_{i,j}\dot{A}_{i,j}$ terms in the above equations, which are small if the envelopes $A_i$ are slowly varying. We obtain the same equations of motion through a two-time scale approximation[2] as performed in [58]. This results in the following

[2]The fast time scale is by $\tilde{\omega} = \frac{\omega_i + \omega_j}{2}$. We define a non-dimensionalized slow time variable as $T = \epsilon\tilde{\omega}t$, where $\epsilon = \frac{1}{Q}$ where $Q$ is the quality factor of the lowest Q mode (pump). The terms in Eqn.[4.11] that are dropped are at least $\epsilon$ smaller than the ones that remain.

equations of motion for the slowly varying envelopes,

$$\begin{aligned} 2\dot{A}_i + \gamma_i A_i &= -i\left(\frac{F_i}{m_i\omega_i} + \frac{g}{2m_i\omega_i}A_j^* A_S\right) = -i\left(v_i + \kappa_i A_j^* A_S\right) && (4.12)\\ 2\dot{A}_j + \gamma_i A_i &= -i\left(\frac{F_j}{m_j\omega_j} + \frac{g}{2m_j\omega_j}A_i^* A_S\right) = -i\left(v_j + \kappa_j A_i^* A_S\right) && (4.13)\\ 2\dot{A}_S + \gamma_S A_S &= -i\left(\frac{F_S}{m_S\omega_S} + \frac{g}{2m_S\omega_S}A_i A_j\right) = -i\left(v_S + \kappa_S A_i A_j\right) && (4.14) \end{aligned}$$

In the above, we define the following parameters for ease of manipulation,

$$v_k = \frac{F_k}{m_k\omega_k}; \quad \kappa_k = \frac{g}{2m_k\omega_k} = \frac{g\gamma_k\chi_k}{2}; \quad k \in [i, j, S] \tag{4.15}$$

The $v_k$'s defined above are proportional to the applied forces $F_k$'s and have dimensions of velocity and the $\kappa_k$'s parametrize the coupling between the modes. We will use the $v_k$'s interchangeably with forces, using Eqn.[4.15] to convert between them.

Firstly, we look at the steady state solution, which can be obtained by setting the time derivatives in Eqns.[4.12-4.14] to zero. We consider the case where only the pump mode is being driven, i.e. $F_{i,j} = 0$.

At small values of the pump force $F_S$, the only allowed solutions are with $A_{i,j} = 0$. Above a threshold pump force, the probe modes aquire non-zero steady state amplitudes. This corresponds to the system undergoing self-oscillation. The threshold pump force is obtained from Eqn.[4.12] and Eqn.[4.13] and is given by,

$$\begin{aligned} |v_{S,th}| &= \gamma_S\sqrt{\frac{\gamma_1\gamma_j}{\kappa_1\kappa_j}} && (4.16)\\ \Rightarrow F_{S,th} &= m_S\omega_S\gamma_S\sqrt{\frac{\gamma_1\gamma_j}{\kappa_1\kappa_j}} && (4.17) \end{aligned}$$

It is convenient to rewrite the above equation and the ones that follow in terms of the magnitude of the on-resonant susceptibility of the oscillators as

$$\begin{aligned} \chi_k &= \frac{1}{m_k\omega_k\gamma_k} && (4.18)\\ k &\in [i, j, S] \end{aligned}$$

Note that the susceptibility is complex, and is given by $\chi_k(\omega = \omega_k) = -i\chi_k$, with $\chi_k$ as defined above i.e., $|\chi_k(\omega = \omega_k)| = \chi_k$. In terms of the susceptibility the threshold drive force and drive displacement are given by

$$F_{S,th} = \frac{2}{g\chi_S\sqrt{\chi_i\chi_j}} \quad X_{S,th} = \frac{2}{g\sqrt{\chi_i\chi_j}} \tag{4.19}$$

Above threshold, the saturated/steady state amplitudes of the probe modes grow with increasing pump drive. The functional form for the saturated probe amplitudes as a function of pump drive are given by

$$\Rightarrow |A_i|^2 = 2\sqrt{\frac{\chi_i}{\chi_j}}\left(\frac{F_S - F_{S,th}}{g}\right) \tag{4.20}$$

$$|A_j|^2 = 2\sqrt{\frac{\chi_j}{\chi_i}}\left(\frac{F_S - F_{S,th}}{g}\right) \tag{4.21}$$

We parametrize the drive force in terms of the threshold drive force and define the normalized parametric drive $\mu = \frac{F_S}{F_{S,th}}$. Fig.[4.10] shows a plot of the predicted pump and signal and idler amplitudes as a function of this scaled parametric drive. We see that the pump amplitude grows linearly with drive force until the instability threshold, where it saturates, at which point the signal and idler amplitudes grow $\propto \sqrt{F_S - F_{S,th}}$. The functional dependence of the saturated amplitude of the signal and idler amplitudes agrees very well with that predicted by the model as can be seen in Fig.[4.11] (left axis).

An additional prediction of the model that is borne out by the data is the linear dependence of the growth rate of the modes above the instability threshold (See Fig.[4.11](right axis)). This predicted growth rate $\propto (V - V_{th})$ is easily seen by solving the time dependent Eqns.[4.12-4.14] with a drive force exceeding the threshold drive.

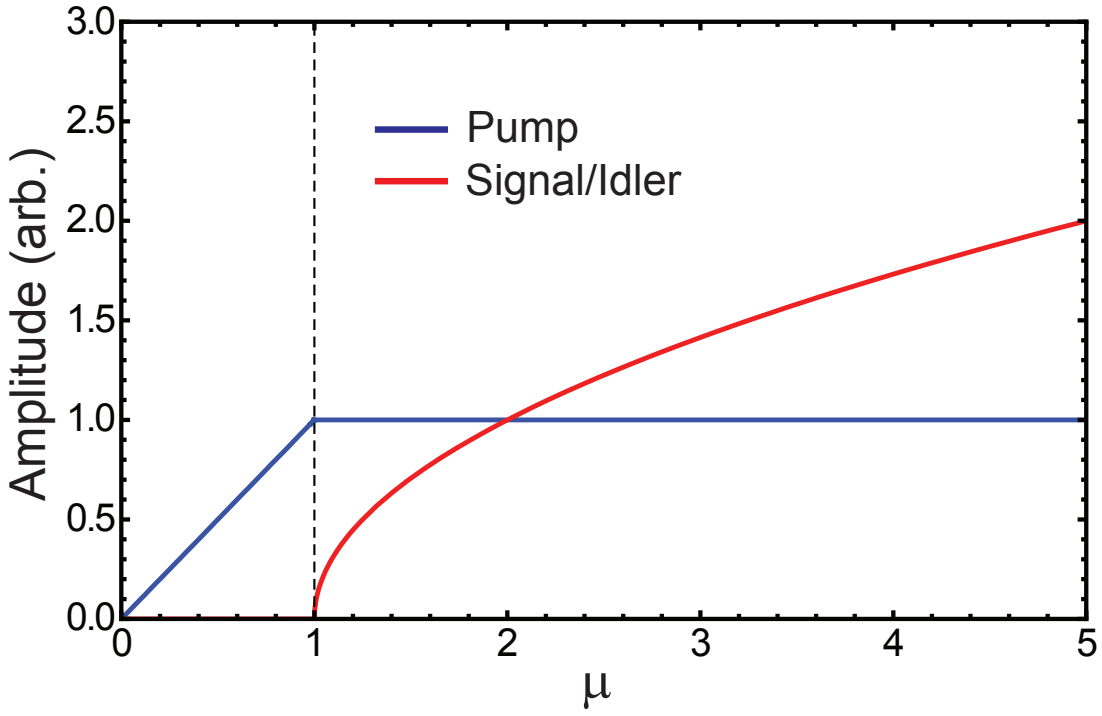


Figure 4.10: Signal/Idler (blue) and Pump (Substrate mode) (red) amplitudes as a function of the scaled drive parametric drive $\mu = \frac{F_S}{F_{S,th}}$ showing the functional dependence predicted by the model.

### 4.5.1 Threshold as a function of detuning

We now consider the case where the pump drive ($\nu_d$) is detuned from $\nu_i + \nu_j$. We assume for simplicity the case where the substrate mode is still on resonance with the sum of the membrane mode frequencies, i.e. $\nu_S = \nu_i + \nu_j$. Given the fact that modes of the substrate are much broader than modes of the membrane, this is a valid assumption.

We solve the same equations (Eqns.[4.12-4.14]), except that the drive at the pump, in Eqn.[4.14] is detuned from resonance and hence has a slow time dependence.

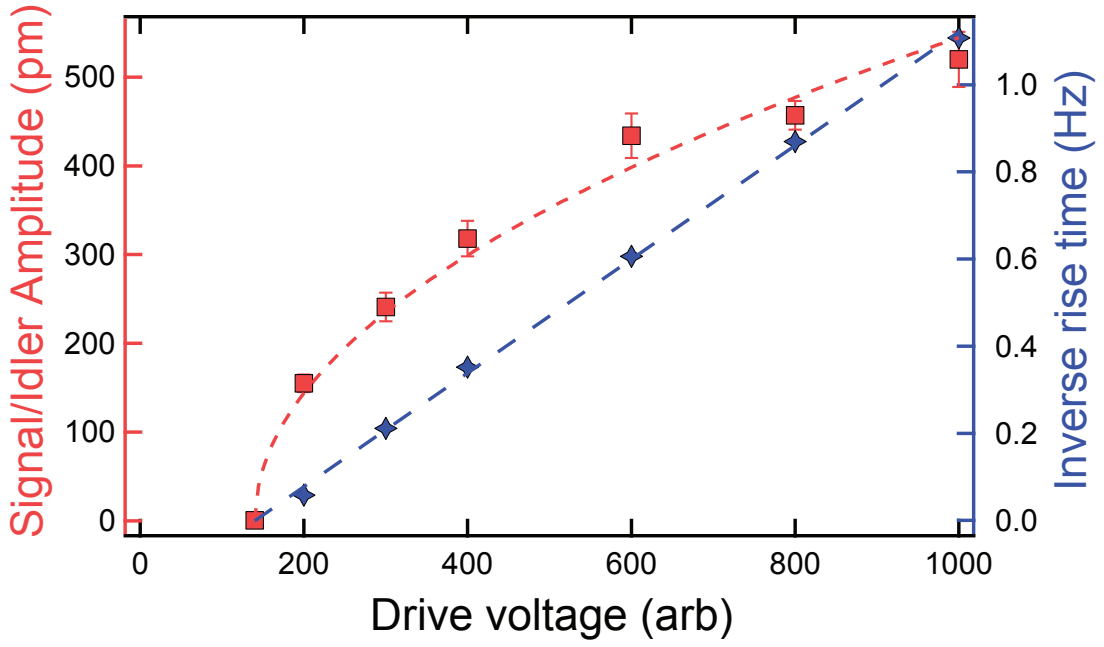


Figure 4.11: Saturation amplitude of the probe (red squares) fit to $f(V) = \alpha(V - V_{th})^{\frac{1}{2}}$ and growth rate (blue crosses) as a function of the drive voltage with linear fit.

We therefore make the following replacements in Eqn.[4.14],

$$v_S \rightarrow v_S e^{i\delta_S t} \tag{4.22}$$

$$F_S \rightarrow F_S e^{i\delta_S t} \tag{4.23}$$

$$\delta_S = \omega_d - \omega_i - \omega_j = \omega_d - \omega_S \tag{4.24}$$

The variables $v_S, F_S$ are now once again time independent. Since the pump drive is detuned from $\nu_i + \nu_j$, when driven above threshold, the probe modes will no longer oscillate at their natural frequencies. We therefore write the slowly varying complex amplitudes as

$$A_k = B_k e^{i\delta_k t}$$

$$k \in [i, j, S]$$

The equations of motion for the variables $B_i$ become,

$$2\dot{B}_i + \gamma_i B_i = -2i\delta_i B_i - i\left(v_i + \kappa_i B_j^* B_S\right) \tag{4.25}$$

$$2\dot{B}_j + \gamma_j B_j = -2i\delta_j B_j - i\left(v_j + \kappa_j B_i^* B_S\right) \tag{4.26}$$

$$2\dot{B}_S + \gamma_S B_S = -2i\delta_S B_S - i\left(v_S + \kappa_S B_i B_j\right) \tag{4.27}$$

Note that in the above, we have once again defined,

$$v_k = \frac{F_k}{m_k\omega_k}; \quad \kappa_k = \frac{g}{2m_k\omega_k} = \frac{g\gamma_k\chi_k}{2}; \quad k \in [i, j, S]$$

We once again obtain the steady-state solutions by setting the time-derivatives in Eqn.[4.25-4.27] to zero. Doing so and substituting Eqn.[4.26] into Eqn.[4.25] gives,

$$\kappa_i\kappa_j B_i|B_S|^2 = B_i(\gamma_i + 2i\delta_i)(\gamma_j - 2i\delta_j) \tag{4.28}$$

$$= B_i\left(\gamma_i\gamma_j + 4\delta_i\delta_j + 2i(\delta_i\gamma_j - \delta_j\gamma_i)\right) \tag{4.29}$$

The reality of $|B_S|^2$ in Eqn.[4.29] results in the following relation between the detunings of the probe modes for the case of a pump drive detuned from resonance.

$$\frac{\delta_i}{\delta_j} = \frac{\gamma_i}{\gamma_j} \tag{4.30}$$

The extent of frequency pulling of each the probe modes is therefore predicted to be proportional to their respective damping rates. This does not always bear out with what is observed experimentally (See Fig.4.12).

The critical pump mode amplitude above which there exists a non trivial self oscillating solution, with $B_{i,j} \neq 0$ is also obtained from Eqn.[4.29] and noting that

$$\frac{\delta_i}{\gamma_i} = \frac{\delta_j}{\gamma_j} = \frac{\delta_i + \delta_j}{\gamma_i + \gamma_j} = \frac{\delta_S}{\gamma_{tot}} \tag{4.31}$$

where $\gamma_{tot} = \gamma_i + \gamma_j$. The critical pump amplitude for onset of self-oscillation is therefore,

$$|B_S| = \sqrt{\frac{\gamma_i\gamma_j}{\kappa_i\kappa_j}\left(1 + \frac{4\delta_S^2}{\gamma_{tot}^2}\right)} \tag{4.32}$$

$$= \frac{2}{g\sqrt{\chi_i\chi_j}}\left(1 + \frac{4\delta_S^2}{\gamma_{tot}^2}\right)^{\frac{1}{2}} \tag{4.33}$$

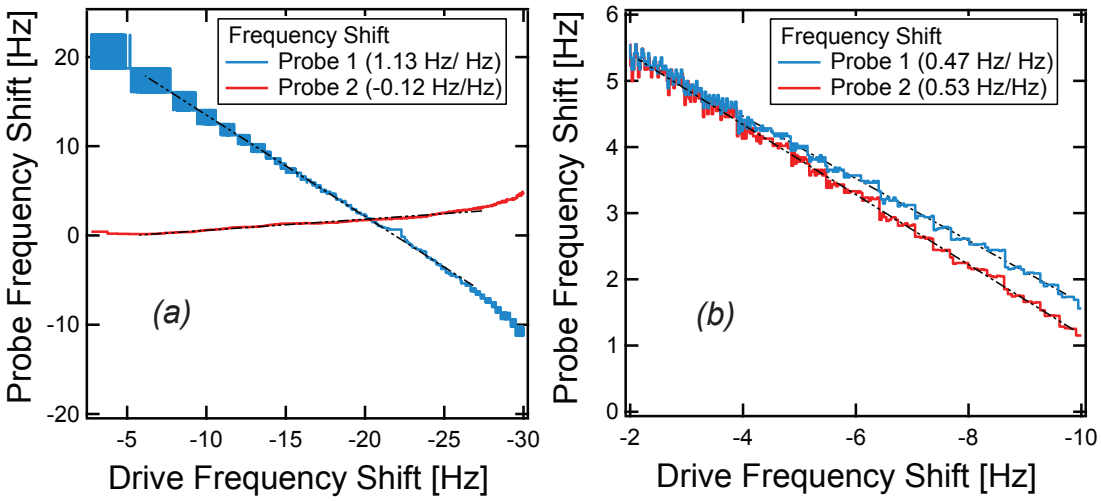


Figure 4.12: Frequency shift of probe modes as a function of drive frequency shift for two different parametric resonances (a) Measured ratio of frequency shifts $(\frac{\delta\nu_i}{\delta\nu_j}) = -9.4$ ; $\frac{\gamma_i}{\gamma_j} = 15.6$ (b) Measured ratio of frequency shifts (Probe1/Probe2) $= 0.89$; $\frac{\gamma_i}{\gamma_j} = 0.9$.

The threshold force for parametric oscillation as a function of drive detuning is in turn obtained by substituting Eqn.[4.32] into Eqn.[4.27] and is given by,

$$F_{S,th} = \frac{2}{g\chi_S\sqrt{\chi_i\chi_j}}\left(1+\frac{4\delta_S^2}{\gamma_{tot}^2}\right)^{\frac{1}{2}}\left(1+\frac{4\delta_S^2}{\gamma_S^2}\right)^{\frac{1}{2}} \tag{4.34}$$

which reduces to,

$$F_{S,th} \approx \frac{2}{g\chi_S\sqrt{\chi_i\chi_j}}\left(1+\frac{4\delta_S^2}{\gamma_{tot}^2}\right)^{\frac{1}{2}} \tag{4.35}$$

in the limit that the damping rate of the pump mode is much larger than damping rate of the signal and idler modes, and the drive detuning. The detuning dependence of the threshold voltage data fits the functional dependence predicted by the above formula. Furthermore the width of the instability tongue is in quantitative agreement with that expected from the measured signal mode damping rates. Fig.[4.13] show the instability tongues for two different parametric resonances, with the width of the tongues input using the measured quality factors and frequencies

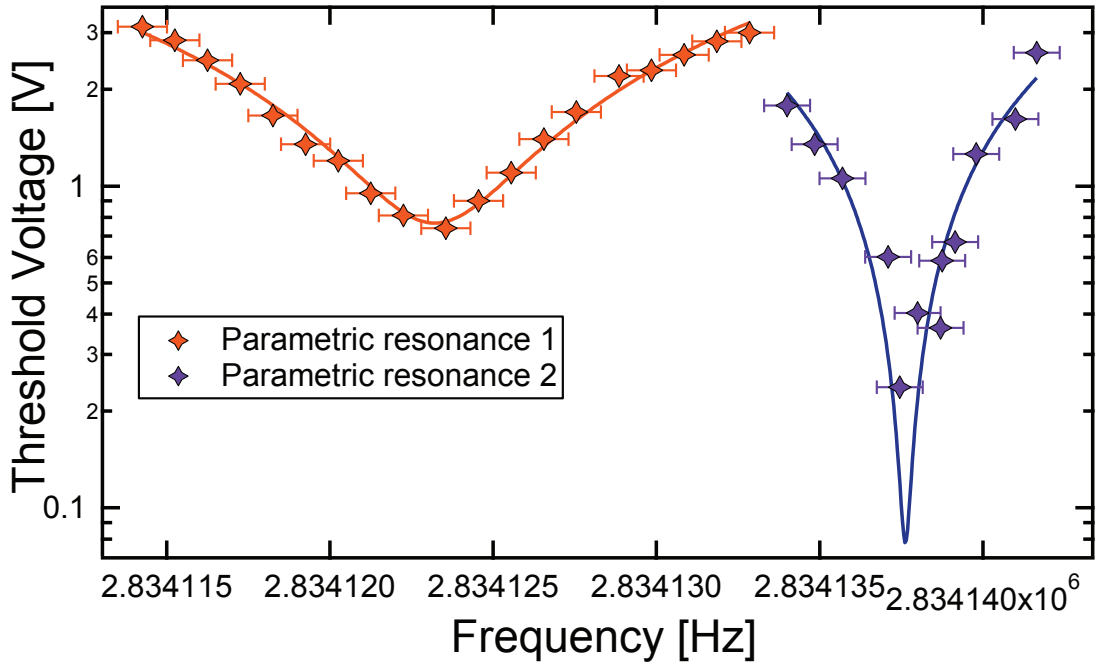


Figure 4.13: Frequency dependence of the threshold for different parametric resonances. The frequency dependence is fit to $V_{th} = V_0(\sqrt{1+\alpha\delta\nu^2})$ with $\alpha = 4/\left(\frac{\nu_i}{Q_i}+\frac{\nu_j}{Q_j}\right)^2$ input based on the measured quality factors and frequencies.

of the signal and idler modes.

### 4.5.2 Predicted quality factor shift

Lastly we consider the quality factor shifts occurring in one of the membrane modes (signal), when the other (idler) is driven to a large amplitude. This arises as a result of the mixing of the signal mode with the lossy substrate mode through the idler mode. In the experiments, the idler is driven to a large amplitude through an external drive thus freezing out its dynamics. The relevant equations of motion

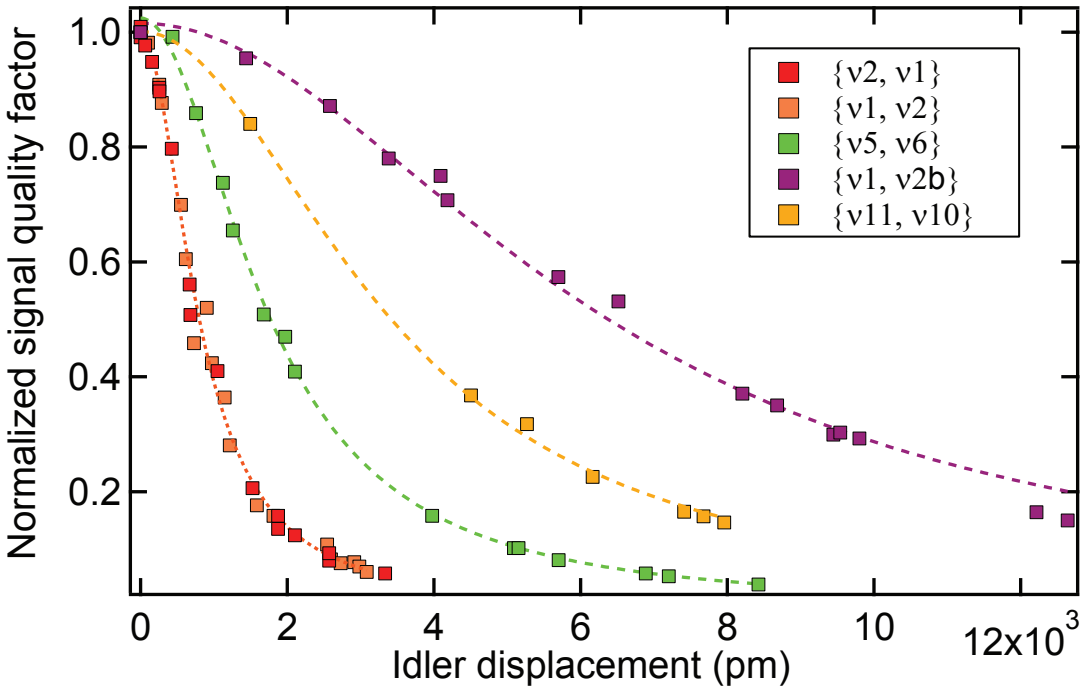


Figure 4.14: Q pulling of the signal mode as a function of the idler amplitude fit to functional form resulting from mixing with the substrate mode

are Eqn.[4.3,4.5] in the absence of applied forces, i.e.,

$$\ddot{x}_i + \gamma_i \dot{x}_i + \omega_i^2 x_i = \frac{g}{m_i} X_S x_j \tag{4.36}$$

$$\ddot{X}_S + \gamma_S \dot{X}_S + \omega_S^2 X_S = \frac{g}{m_S} x_i x_j \tag{4.37}$$

The quality factor pulling is most easily seen in the slow time scale approximation which gives the envelopes of the decay, which is what we are interested in anyway. We assume for simplicity that $A_j$ is purely imaginary, which we can do by choosing the phase of the idler drive. The EOM's for the slowly varying envelope are then,

$$2\dot{A}_i + \gamma_i A_i = \kappa_i |A_j| A_S \tag{4.38}$$

$$2\dot{A}_S + \gamma_S A_S = -\kappa_S A_i |A_j| \tag{4.39}$$

$$\kappa_k = \frac{g}{2 m_k \omega_k} = \frac{g \gamma_k \chi_k}{2} \quad k \in [i, j, S] \tag{4.40}$$

The mixing between the modes leads to a change in their respective quality factors, which are obtained by diagonalizing the above equations. This results in a modified signal mode (i) decay rate that is given by,

$$\gamma_i' = \frac{1}{2}\left(\gamma_i + \gamma_S - \sqrt{(\gamma_S - \gamma_i)^2 - 4\kappa_i\kappa_S A_j^2}\right) \tag{4.41}$$

$$= \frac{\gamma_S}{2}\left(1 + \frac{\gamma_i}{\gamma_S} - \sqrt{\left(1 - \frac{\gamma_i}{\gamma_S}\right)^2 - \frac{A_j^2}{\xi^2}}\right) \tag{4.42}$$

$$\Rightarrow \xi = \gamma_S \frac{(m_i m_S \omega_i \omega_S)^{\frac{1}{2}}}{g} \tag{4.43}$$

We note the limits of the above. When $A_j = 0$, $\gamma_i' = \gamma_i$, the bare damping rate of the signal mode. As $A_j$ increases, the signal mode hybridizes with the mode of the substrate, leading to an increase in the effective damping rate to $\gamma_i'$. In the opposite limit, when $A_j \to \xi$, $\gamma_i' \to \frac{\gamma_i+\gamma_S}{2} \approx \frac{\gamma_S}{2}$. At this point, the effective damping rate of the substrate $\gamma_S' \to \frac{\gamma_S}{2}$ and signal membrane mode and the pump substrate mode cannot be distinguished. Given that $\frac{\gamma_i}{\gamma_S} \sim 10^{-4}$, we may further simplify the expressions above, i.e.,

$$\gamma_i' \sim \frac{\gamma_S}{2}\left(1 + 2\frac{\gamma_i}{\gamma_S} - \sqrt{1 - \frac{A_j^2}{\xi^2}}\right) \tag{4.44}$$

The normalized quality factor shift is therefore given by,

$$\frac{Q_i(A_j)}{Q_i(0)} = \frac{\gamma_i}{\gamma_i'} \sim \frac{2\gamma_i}{\gamma_S\left(1 + \frac{2\gamma_i}{\gamma_S} - \sqrt{\left(1 - \frac{A_j^2}{\xi^2}\right)}\right)} \tag{4.45}$$

From Eqn.4.19 and Eqn.4.43, we obtain the following linear relationship between the length scale $\xi$, parametrizing the variation in the quality factor of the signal mode as a function of the amplitude of the idler, and the down-conversion threshold force.

$$\xi(g) = \frac{\sqrt{\chi_S \chi_j}}{2}\sqrt{\frac{\gamma_S}{\gamma_i}} F_{S,th}(g) \tag{4.46}$$

Obtaining $\xi$ assuming a constant value $Q_S$ for the pump mode quality factor, results in a correlation between $\xi$ and $V_{th}$ that is shown in Fig.4.8. The expected relationship between the $\xi$ and $F_{th}$ has an additional factor of $\gamma_i/\gamma_j$. Including this factor results in the corrected relation between the derived $\xi$ and $F_{th}$ does not change the qualitative trend of correlation between the coupling, as obtained from the quality factor shift and that obtained from the parametric instability threshold, suggesting that they are the result of the same two-mode coupling.

## 4.6 Conclusions

The proposed two-mode model proposed captures many of the observed parametric amplifier phenomena. These include:

(1) The linear dependence of the growth rate as a function of drive strength, above threshold.

(2) Functional dependence of the probe amplitude as a function of drive strength, above threshold.

(3) The dependence of the threshold drive amplitude on the drive detuning.

(4) The functional dependence of the quality factor shift (of signal) versus the amplitude of the idler, i.e., the two-mode control of dissipation.

(5) The correlation between the length scale parametrizing the quality factor shift versus amplitude and the parametric instability threshold.

This corroboration of the model with the experimental data is extremely good, over a large dynamic range in the displacement. The phenomena that as yet do not have a quantitative explanation are the two-mode frequency pulling (See Fig.[4.9]), and the bistability in the response to pump amplitude sweeps Fig.[4.4]. Both these

phenomena show variations across different mode pairs. Naively one might think that these phenomena might require the addition of extra nonlinear terms such as the cubic Duffing term. However, it is likely that these phenomena can also be explained by small changes to the two-mode model. For instance the introduction of a frequency mismatch between the substrate mode $\omega_S$, and the sum of the mode frequencies $\omega_i + \omega_j$ could explain the bistable response in analogy with the explanation of similar behavior seen in optical parametric oscillators [65].

In summary, we have realized a mechanical parametric amplifier in a platform that is compatible with ground state cooling, room temperature quantum control and quantum limited detection. Most of the observed parametric amplifier phenomena are explained using a simple two-mode model with a parametric coupling between the resonator modes mediated by a mode of the supporting substrate platform. The model agrees remarkably well with experiments, over several orders of magnitude in displacement. This opens up a powerful new tool for optomechanics, some of the applications of which will be explored in the next chapter.

CHAPTER 5

# THERMOMECHANICAL TWO-MODE SQUEEZING IN A HIGH Q RESONATOR

## 5.1 Introduction

The previous chapter reported on the realization of a nondegenerate parametric amplifier in an ultrahigh Q membrane resonator compatible with optomechanical cooling to the quantum regime and quantum limited detection. The observed dynamics of the parametric amplifier is well described by a two-mode model with a parametric coupling between the resonator modes mediated through an excitation of the silicon substrate platform on which the resonator is suspended. We focused on the experimental validation of the model and largely discussed the dynamics above the parametric instability threshold, focusing on the dynamics of the steady state or average amplitudes and paying no attention to thermal fluctuations and their correlations. In this chapter, we discuss amplitude fluctuations and correlations in the fluctuations of the mechanical modes arising in a nondegenerate mechanical parametric amplifier coupled to a thermal bath.

The parametric coupling that we have realized between distinct modes of the membrane is analogous to the nonlinear parametric coupling between optical fields in an optical parametric amplifier system and allows for a similar manipulation of phononic fields. Among the significant uses of optical parametric amplifiers are the generation of squeezed light[66], the demonstration of continuous variable EPR entanglement[67, 68] and metrology beyond the standard quantum limit[69]. The realization of an optomechanical system with strong two-mode mechanical para-

metric nonlinearities, compatible with ground state cooling holds promise for the realization of similar phenomena in mesescopic mechanical resonators, i.e., the creation of non classical mechanical states and the observation of entanglement between macroscopic mechanical degrees of freedom[70, 52] which are long standing goals in cavity optomechanics.

Additionally, the parametric coupling demonstrated here is of relevance for quantum non-demolition[71] and backaction evading measurement[72] protocols for the measurement of the position of the mechanical resonator and are therefore crucial for the realization of position measurements beyond the standard quantum limit[73].

Even in the classical regime, the exploration of analogies with optical parametric amplifiers suggests the possibility of interferometric schemes[74, 75] for metrology that beat the limitations set by thermal noise, resulting from the correlations between the signal and idler modes.

The first step towards this goal is thermomechanical noise squeezing[61], which in a nondegenerate parametric amplifier, manifests as two-mode squeezing of a composite quadrature formed from linear combinations of the quadratures of the individual resonator modes, the demonstration[13] of which is described in this chapter.

This chapter is organized as follows. We first study the coherent below threshold dynamics through the weak actuation of the membrane modes in the presence of the parametric drive. This results in a phase dependent gain in the nondegenerate parametric amplifier, described in Sec.[5.2] and experimentally demonstrated in Sec.[5.3], with close agreement with theoretical predictions providing further validation for the two-mode model (Sec.[4.5]). In the absence of coherent drive forces, i.e., in the presence only of thermal noise forces and with the pump driven

below the parametric instability threshold, the thermal fluctuations of the two mechanical modes become highly correlated. These correlations manifest as two-mode squeezing of a composite quadrature formed from linear combinations of the quadratures of the individual resonator modes. This thermomechanical analogue of two-mode squeezing seen in optical parametric amplifiers[68] is demonstrated in Sec.[5.4]. The degree of squeezing closely follows the predictions of the two-mode model (cf. Sec.[4.5]) with the addition of thermomechanical noise forces. Sec.[5.5] describes the formalism for the calculation of fluctuation spectra in the presence of thermal noise and Sec.[5.6] presents the results of this calculation for thermomechanical noise squeezing below threshold. In Sec.[5.7], we discuss the behavior of the fluctuations of membrane modes with the pump driven above the parametric instability threshold. Here, we observe noise squeezing of a different kind, viz., amplitude difference squeezing, with the observed behavior analogous to intensity difference squeezing seen in optical parametric oscillators[76] and contrast this squeezing with what is observed below threshold.

## 5.2 Phase dependent amplification: Model predictions

In this section, we consider the coherent dynamics of a nondegenerate parametric amplifier with the pump field driven below the instability threshold for self oscillation. In this regime, the weak actuation of a membrane mode (idler, i), in the presence of the pump drive results in the phase coherent production of phonons in the other membrane mode (signal, j). The coherent dynamics observed in this case is a result of the interference of the downconverted signal field, which has a well defined phase relationship between the pump and the idler field and any preexisting signal field arising from the weak actuation of the signal. This results

in the gain of the signal field having a strong dependence on the phase of the pump field ($\phi$).

This behavior, and the expected phase dependent gain, is obtained by the analysis of the slow time equations Eqn.[4.12-4.14] of Sec.[4.5], describing the temporal variation of the envelopes of mode displacements ($A_i$), reproduced below:

$$2\dot{A}_i = \gamma_i \left[ -A_i + i\frac{g}{2}\chi_i A_j^* A_S + i\chi_i \tilde{F}_i(t) \right] \tag{5.1}$$

$$2\dot{A}_j = \gamma_j \left[ -A_j + i\frac{g}{2}\chi_j A_i^* A_S + i\chi_j \tilde{F}_j(t) \right] \tag{5.2}$$

$$2\dot{A}_S = \gamma_S \left[ -A_S + i\frac{g}{2}\chi_S A_i A_j + i\chi_S \tilde{F}_S(t) \right] \tag{5.3}$$

In the above $g$ is the strength of the two-mode coupling, given by Eqn.[4.2], i.e., $H_{ij} = -g x_i x_j X_S$, and $\chi_k = \frac{1}{m_k \omega_k \gamma_k}$ are the on resonant susceptibilities of the mechanical modes. $\tilde{F}_{i,j}$ are the slowly varying (complex) amplitudes of the external forces on the individual membrane modes. Even in the absence of external forces $\tilde{F_{i,j}}$, these coupled equations allow for non-zero steady state amplitudes, i.e., parametric self-oscillation, above a threshold substrate amplitude and corresponding force given by

$$X_{S,th} = \frac{2}{g\sqrt{\chi_i \chi_j}}; \quad F_{S,th} = \frac{2}{g\chi_S \sqrt{\chi_i \chi_j}} \tag{5.4}$$

In the presence of external actuation of the individual membrane modes and the substrate ('pump') mode, i.e., $\tilde{F_{i,j}} \neq 0, A_S \neq 0$, the amplitude of each mode is a coherent superposition of its individual response to the external force and the down-converted phonons arising from the two-mode nonlinearity. The complex amplitudes in the steady state are obtained by solving Eqn.[5.1-5.3] with time derivatives set to zero. These are:

$$A_i = \frac{e^{i(\phi_i - \pi/2)}}{1-\mu^2} \left( \chi_i |\tilde{F}_i| + \mu \sqrt{\chi_i \chi_j} |\tilde{F}_j| e^{i\delta\phi} \right) \tag{5.5}$$

$$A_j = \frac{e^{i(\phi_j - \pi/2)}}{1-\mu^2} \left( \chi_j |\tilde{F}_j| + \mu \sqrt{\chi_i \chi_j} |\tilde{F}_i| e^{i\delta\phi} \right) \tag{5.6}$$

where $\mu = X_S/X_{S,th}$ is the pump amplitude normalized to the threshold for parametric instability and $\delta\phi = \phi_S - \phi_i - \phi_j$ with $\phi_{i,j,S}$ being the various phases associated with the external forces. The above equation can be recast in terms of a phase-dependent gain $G_{i,j}(\delta\phi) = |A_{i,j}|/|A^0_{i,j}|$ where $A^0_{i,j}$ are the steady state amplitudes of the respective modes in the absence of down-conversion. This phase-dependent gain is then given by

$$\begin{aligned} G_j(\delta\phi) &= \frac{1}{1-\mu^2} \\ &\times \sqrt{1 + \mu^2 \frac{\chi_i}{\chi_j}\left(\frac{|\tilde{F}_i|}{|\tilde{F}_j|}\right)^2 - 2\mu\left(\frac{\chi_i}{\chi_j}\right)^{1/2}\frac{|\tilde{F}_i|}{|\tilde{F}_j|}\cos(\delta\phi)} \\ &= \frac{1}{1-\mu^2}\sqrt{1 + \mu^2\eta_{ji}^2 - 2\mu\eta_{ji}\cos(\delta\phi)} \end{aligned} \tag{5.7}$$

where $\eta_{ji} = (\chi_j/\chi_i)^{1/2} \times (\bar{x}_i/\bar{x}_j)$ and $\bar{x}_{i,j}$ are the amplitudes of the membrane modes in the absence of the pump. We note that the gain diverges at the instablity threshold, $\mu = 1$ . This gives us the predicted functional dependence of the gain as a function of the amplitudes of the signal and idler modes and the amplitude of the pump mode.

## 5.3 Experimental demonstration of phase dependent amplification

The phase dependent gain of a nondegenerate amplifier is demonstrated by monitoring the amplitudes of the signal and idler modes while directly driving them, with the parametric pump drive on. The signal and idler drive amplitudes and phases and the pump drive amplitude are fixed while the pump phase is changed slowly, to avoid transient effects.

For simplicity of analysis of experimental results, one of the modes is driven much

more strongly than the other. The signal mode is driven to $35 \times (k_B T/m\omega_j^2)^{1/2}$, while the idler mode was actuated to an amplitude of $400 \times (k_B T/m\omega_i^2)^{1/2}$. The

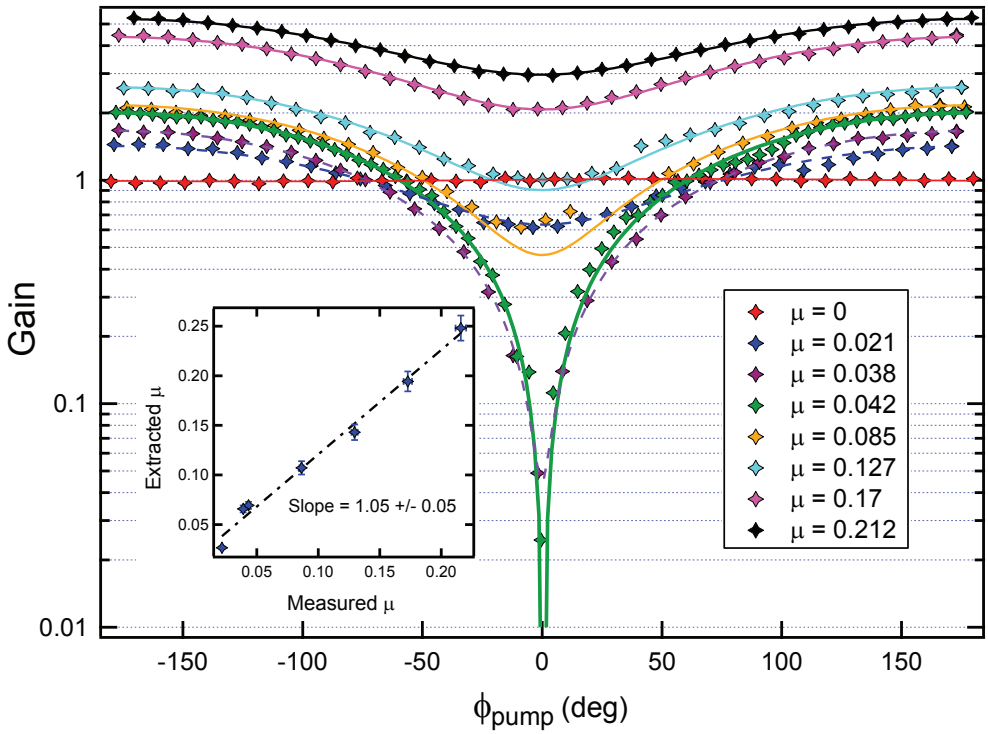


Figure 5.1: Parametric gain verus the phase of the pump excitation. The data is fit to Eqn.[5.7] and the known values of the signal and idler amplitude used to extract the pump amplitude $\mu$. (Inset) Normalized pump amplitude $\mu$ extracted from the fits, as a function of the measured normalized pump amplitude.

phase dependent gain of the signal mode for different values of the normalized pump amplitude $\mu$ and pump phase $\phi$ is shown in Fig.[5.1] (This data was obtained courtesy Yogesh Patil). The parametric drive strengths extend from $\mu = 0.02 \rightarrow 0.2$. We fit the data in Fig.[5.1] to the functional form given by Eqn.[5.7], where both $\eta_{ji}$ and $\mu$ are independently measured quantities. $\eta_{ji}$ is extracted from the measured displacements of the membrane modes in the absence of the pump drive and $\mu$ is the ratio of the pump drive amplitude and the independently measured threshold drive amplitude. We fit the phase dependent gain curves using Eqn.[5.7],

and use the measured probe displacements to make an independent measurement of $\mu$. The inset of Fig.[5.1] shows a plot of the $\mu$'s extracted from the fits as a function of the $\mu$'s calculated directly using the drive voltages and the measured threshold drive voltage. They agree to within 5% providing further credence to the two-mode model.

There is an important distinction between the phase-dependent gain as seen in our system and that observed in a degenerate parametric amplifier. In the latter case, the maximal deamplification is limited to 0.5 (3 dB) before the onset of parametric instability[61]. In contrast, the additional degree of freedom in a nondegenerate parametric amplifier (the idler field), allows for an arbitrarily large degree of deamplification of the signal mode.

## 5.4 Experimental demonstration of two-mode thermomechanical squeezing

With the parametric pump driven below the instability threshold and in the presence of coherent drive forces acting on the signal and idler modes, their amplitudes, are a function of the pump phase. This resulted in the phase dependent gain discussed in the previous section. In the absence of coherent actuation and in the presence only of thermomechanical noise forces acting on the resonator modes, the phase dependent gain feature gets washed out. In this case, with the pump field driven below threshold, the motion of the membrane modes become highly correlated. These correlations manifest as the squeezing of a composite quadrature formed from linear combinations of quadratures of the individual membrane modes. To quantify the degree of two-mode squeezing, we construct

cross-quadratures from the displacements of the membrane modes, according to the relations $x_{\pm} = (\alpha_i \pm \alpha_j)/\sqrt{2}, y_{\pm} = (\beta_i \pm \beta_j)/\sqrt{2}$ where $\{\alpha_i, \beta_i\}$ are the respective quadratures of the individual membrane modes normalized to thermomechanical amplitudes. Phase-space distributions of these quadratures, accumulated over typ-

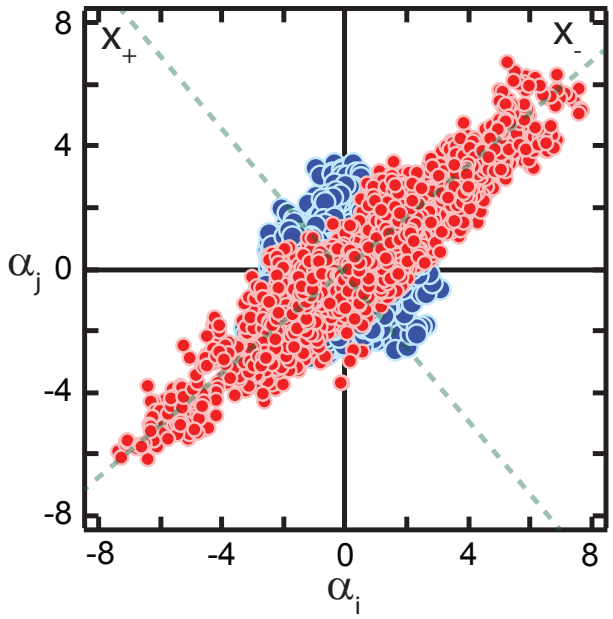


Figure 5.2: Phase space distributions of the quadratures $\alpha_i, \alpha_j$ in the absence (blue) and presence (red) of the pump field, showing the emergence of correlations, i.e., thermemechanical two-mode squeezing, due to nondegenerate parametric amplification.

ical durations of 300 s ($\sim$ 100 decay periods), are shown in Fig.[5.2](This data was obtained courtesy Yogesh Patil). The phase space distributions are symmetric (blue filled circles) in the absence of down-conversion, with the pump drive off. In the presence of the pump drive, these phase space distributions acquire a large ellipticity (red filled circles) for increasing amplitudes of the pump field ($\mu = 0.95$). The variances and standard deviations of the amplified ($x_-$) and squeezed ($x_+$) quadratures are extracted from such distributions. These standard deviations, for

various values of the normalized pump drive, are plotted in Fig.[5.3]. Here the y

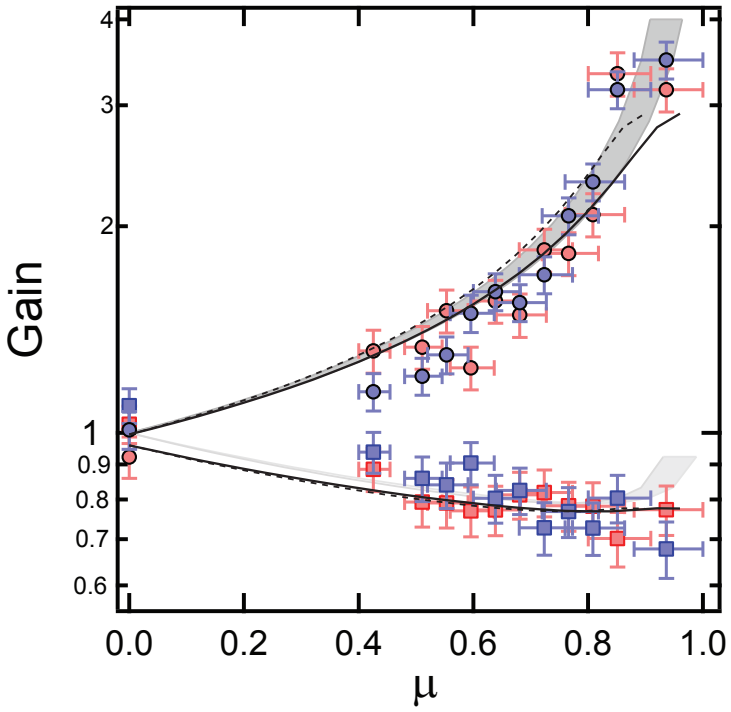


Figure 5.3: The standard deviations of the cross-quadratures $x_-, y_+$ (amplified) and $x_+, y_-$ (squeezed) *vs* pump amplitude. The shaded curves indicate the no-free-parameter steady prediction of the two-model with added thermal noise (Sec.[5.5,5.6]), based on independently measured frequencies and damping rates of the mechanical mode. The solid and dashed black lines indicate the bounds for the predictions of the noise model after accounting for the finite observation time.

error bars in the data points reflect the variation in the standard deviations across different iterations of the experiment, for the same value of the normalized pump drive ($\mu$). The x error bars are errors in the normalized drive, arising from temporal variations of the threshold voltage due to frequency fluctuations. The gray shaded curves indicate the no-free-parameter prediction of the two-mode model with added thermal noise (Sec.[5.5,5.6]), based on independently measured fre-

quencies and damping rates of the mechanical mode. These shaded curves are the predicted standard deviations from the noise squeezing model in the steady state, i.e., assuming infinite sampling time. The agreement with the model predictions becomes even closer once the finite time of measurement is taken into account (See Sec.[5.6.4]) as indicated by the black solid and dashed curves. The noise squeezing model predicts that the maximal degree of steady state thermomechanical squeezing is limited by thermal averaging across all possible phases between the fields, to a peak noise squeezing (variance reduction) of $\frac{1}{2}$ or 3 dB (See Sec.[5.6]). Since an arbitrarily large degree of squeezing may be obtained for specific phase relationships between the signal, idler and pump fields, we estimate that mechanical squeezing of more than 40 dB may be obtained with our demonstrated parameters by harnessing weak measurements and feedback[77].

In the sections that follow, we describe the noise squeezing model, elaborate on the reason for 3 dB noise reduction in the steady state and study the dependence of the degree of squeezing on asymmetries in the frequencies, loss rates of the two mechanical modes and pump detuning which are all detrimental to squeezing. We then discuss the manifestations of squeezing above threshold, where quadrature squeezing gives way to amplitude difference squeezing, akin to intensity difference squeezing seen in optical parametric oscillators and discuss the crossover of correlations between the two limits.

## 5.5 Solving for fluctuation spectra in the presence of thermal noise

We obtain the correlations that develop between the resonator modes in the presence of the pump drive, by analyzing the coupled equations for the resonator modes under the influence of a classical actuation of the pump/substrate mode along with thermomechanical Langevin noise forces acting on the membrane and substrate modes.

We distinguish between the mean displacement and its fluctuations by writing $z_{i,j} = (\bar{A}_{i,j} + \delta A_{i,j})e^{-i\omega_{i,j}t}$ where $\langle \delta A_{i,j} \rangle = 0$. The coupled equations for the fluctuations can be written as,

$$\begin{aligned} 2\begin{pmatrix} \delta\dot{A}_i \\ \delta\dot{A}_j \\ \delta\dot{A}_S \end{pmatrix} &= \begin{pmatrix} -\gamma_i & 0 & i\kappa_i\bar{A}_j^* \\ 0 & -\gamma_j & i\kappa_j\bar{A}_i^* \\ i\kappa_S\bar{A}_j & i\kappa_S\bar{A}_i & -\gamma_S \end{pmatrix}\begin{pmatrix} \delta A_i \\ \delta A_j \\ \delta A_S \end{pmatrix} \\ &+ \begin{pmatrix} 0 & i\kappa_i\bar{A}_S & 0 \\ i\kappa_j\bar{A}_S & 0 & 0 \\ 0 & 0 & 0 \end{pmatrix}\begin{pmatrix} \delta A_i^* \\ \delta A_j^* \\ \delta A_S^* \end{pmatrix} + i\begin{pmatrix} \gamma_i\chi_i F_i \\ \gamma_j\chi_j F_j \\ \gamma_S\chi_S F_S \end{pmatrix} \end{aligned} \tag{5.8}$$

where we have defined coupling parameters,

$$\kappa_k \;=\; \frac{g\gamma_k\chi_k}{2} = \frac{g}{2m_k\omega_k}; \quad k \in [i, j, S] \tag{5.9}$$

for notational simplicity. The thermomechanical noise forces are assumed to be white noise correlated and obey,

$$\langle F_i(t) \rangle = \langle F_i(t)F_j(t') \rangle = 0, \tag{5.10}$$

$$\langle F_i(t)F_j^*(t+\tau) \rangle = 8\gamma_i m_i k_B T \delta_{ij}\delta(\tau) \tag{5.11}$$

We decompose the complex displacements into real quadratures according to $\delta\mathbf{A} = \delta\vec{\alpha} + i\delta\vec{\beta}$ and where $\delta\mathbf{A} = (\delta A_i, \delta A_j, \delta A_S)^T$. Correspondingly the noise, $\mathbf{v} =$

$i(\gamma_i\chi_i F_i, \gamma_j\chi_j F_j, \gamma_S\chi_S F_S)^T$is also decomposed into real and imaginary parts, $\mathbf{v} = \mathbf{v}_\alpha + i\mathbf{v}_\beta$ . Expressing Eqn.[5.8] in terms of these quantities gives,

$$\delta\dot{\vec{\alpha}} = \mathbf{M}_\alpha\delta\vec{\alpha} + \mathbf{v}_\alpha \tag{5.12}$$

$$\delta\dot{\vec{\beta}} = \mathbf{M}_\beta\delta\vec{\beta} + \mathbf{v}_\beta \tag{5.13}$$

For the general case, valid both above and below threshold,

$$\mathbf{M}_{\alpha,\beta} = \frac{1}{2}\begin{pmatrix} -\gamma_i & \mp\kappa_i|\bar{A}_S| & \kappa_i|\bar{A}_j| \\ \mp\kappa_j|\bar{A}_S| & -\gamma_j & \kappa_j|\bar{A}_i| \\ -\kappa_S|\bar{A}_j| & -\kappa_S|\bar{A}_i| & -\gamma_S \end{pmatrix} \tag{5.14}$$

and the elements of $\mathbf{v}_{\alpha,\beta}$ satisfy $\langle v_i\rangle = 0$, $\langle v_k(t)v_l(t+\tau)\rangle = \frac{\gamma_l k_B T}{m_l\omega_l^2}\delta_{kl}\delta(\tau)$. In writing Eqn.[5.14], we have made a choice for the pump drive phase ($\phi_S = 0$) and the resonator mode detection phases ($\phi_{i,j} = 0$). In general, these phases can also be chosen such that there is a coupling between the $\delta\vec{\alpha}$ and $\delta\vec{\beta}$ quadratures, as they have been defined. When the pump drive phase is not fixed, but evolving in time, for instance with the pump drive detuned, this coupling is physical and does not vanish through a suitable choice of detection phases.

The spectrum in the steady state is obtained by taking the expectation value after Fourier transforming and inverting Eqns.[5.42,5.43], and are given by the matrix equation,

$$\mathbf{S}_{\alpha,\beta}(\omega) = \frac{1}{2\pi}(\mathbf{M}_{\alpha,\beta} + i\omega\mathbf{I})^{-1}\mathbf{D}(\mathbf{M}_{\alpha,\beta}^T - i\omega\mathbf{I})^{-1} \tag{5.15}$$

where $\mathbf{I}$ is the identity and

$$\mathbf{D} = \langle\mathbf{v}\mathbf{v}^T\rangle = k_B T\begin{pmatrix} \frac{\gamma_i}{m_i\omega_i^2} & 0 & 0 \\ 0 & \frac{\gamma_j}{m_j\omega_j^2} & 0 \\ 0 & 0 & \frac{\gamma_S}{M_S\omega_S^2} \end{pmatrix} \tag{5.16}$$

is a matrix characterizing the diffusion due to thermal forces. The variances in the steady state can be obtained from the spectrum using the Wiener-Khintchine

theorem, by integrating the fluctuations over frequency, i.e.,

$$\boldsymbol{\sigma}_{\alpha,\beta} = \int_{-\infty}^{\infty} \mathbf{S}_{\alpha,\beta}(\omega) d\omega \tag{5.17}$$

The formalism described, is valid both above and below the parametric instability threshold. We first discuss the squeezing bound arising for the case where the pump is driven below the instability threshold, the case that was experimentally explored in Sec.[5.4].

## 5.6 Thermomechanical two-mode squeezing: below threshold predictions

When the pump is driven below the instability threshold, correlations develop between the displacements of the two mechanical modes, as we have seen, resulting in two-mode squeezing, i.e., squeezing of a combined quadrature of the individual oscillators. In this regime, the fluctuations of the individual quadratures, $\delta\vec{\alpha}$ and $\delta\vec{\beta}$ are given by Eqns.[5.42,5.43] with $\mathbf{M}_{\alpha,\beta}$ given by Eqn.[5.14], setting the average signal and idler amplitudes, $\bar{A}_{i,j} = 0$. As the pump drive force increases, the increase in the pump amplitude results in greater correlations between the two modes. These correlations, as before, are quantified by defining cross-quadratures constructed from $\{\alpha_{i,j}, \beta_{i,j}\}$, here normalized to their respective thermomechanical amplitudes, according to the relations,

$$x_{\pm} = (\alpha_i \pm \alpha_j)/\sqrt{2} \tag{5.18}$$

$$y_{\pm} = (\beta_i \pm \beta_j)/\sqrt{2} \tag{5.19}$$

The correlations between the two modes manifest as amplification and squeezing of these collective quadratures. We represent the fluctuations in these cross-

quadratures, along with the fluctuation of the pump substrate mode, through the column vectors $\mathbf{X} = (\delta x_+, \delta x_-, \delta x_S)^T$, $\mathbf{Y} = (\delta y_+, \delta y_-, \delta y_S)^T$, related to the original quadrature fluctuations $\delta\vec{\alpha}$,$\delta\vec{\beta}$ via,

$$\mathbf{X} = \mathbf{R}\delta\tilde{\alpha}; \quad \mathbf{Y} = \mathbf{R}\delta\tilde{\beta}; \quad \mathbf{R} = \frac{1}{\sqrt{2}} \begin{pmatrix} 1 & 1 & 0 \\ 1 & -1 & 0 \\ 0 & 0 & 1 \end{pmatrix} \tag{5.20}$$

with the correlations of the cross quadratures obtained through a corresponding transformation of $\mathbf{S}_{\alpha,\beta}(\omega)$,

$$\mathbf{S}_X(\omega) = \left\langle \mathbf{X}(\omega)\mathbf{X}(\omega)^\dagger \right\rangle = \mathbf{R}\mathbf{S}_\alpha\mathbf{R}^T \tag{5.21}$$

along with the analogous equation for $\mathbf{Y}$ ($X \to Y \quad \& \quad \alpha \to \beta$ in the above). The degree of squeezing/amplification is measured through the variances of these cross quadratures, obtained by integrating the spectra in Eqn.[5.21] over frequency.

The variances obtained depend on the frequencies and loss rates of the two modes, with unequal frequencies and loss rates reducing the degree of peak squeezing in the steady state, i.e., for infinite measurement time. The degree of squeezing for a given value of the normalized drive $\mu$ is independent of the mean loss rate ($\bar{\gamma} = (\gamma_i+\gamma_j)/2$) and frequency ($\bar{\omega} = (\omega_i + \omega_j)/2$), which only affect the absolute value of the threshold force. The degree of two-mode squeezing depends on the loss rates and the frequencies of the individual resonator modes through a dimensionless loss asymmetry parameter $\delta = (\gamma_i - \gamma_j)/(\gamma_i + \gamma_j)$ and frequency asymmetry parameter $\delta_\omega = (\omega_i - \omega_j)/(\omega_i + \omega_j)$. To build an understanding of quadrature squeezing below threshold, we first consider the simplest case of distinct resonator modes with identical frequencies ($\delta_\omega = 0$) identical losses ($\delta = 0$).

### 5.6.1 Symmetric losses and frequencies: Thermomechanical squeezing bound

We first consider the simplest case of distinct resonator modes with identical frequencies ($\delta_\omega = 0$) identical losses ($\delta = 0$). For this case, the evolution matrices in Eqn.[5.14] reduce to,

$$\mathbf{M}_{\alpha,\beta} = \frac{1}{2}\begin{pmatrix} -\gamma & \mp\gamma\mu & 0 \\ \mp\gamma\mu & -\gamma & 0 \\ 0 & 0 & -\gamma_S \end{pmatrix} \tag{5.22}$$

where in the above $\gamma$ is the damping rate of the membrane modes, $\mu$ is the normalized parametric drive strength and $\gamma_S$ is the decay rate of the substrate mode. Calculating the spectrum of fluctuations using Eqn.[5.15] and Eqn.[5.21] results in the following spectra for the collective quadratures.

$$\mathbf{S}_{\mathbf{X},\mathbf{Y}} = \frac{2}{\pi}\begin{pmatrix} \frac{\gamma}{(\gamma^2(1\pm\mu)^2+4\omega^2)} & 0 & 0 \\ 0 & \frac{\gamma}{(\gamma^2(1\mp\mu)^2+4\omega^2)} & 0 \\ 0 & 0 & \frac{\gamma_S}{\left(\gamma_S^2+4\omega^2\right)} \end{pmatrix} \tag{5.23}$$

The variances of the collective quadratures of the mechanical modes, normalized to thermal motion are, through Eqn.[5.17], given by,

$$\sigma_{x_\pm,x_\pm} = \frac{1}{1\pm\mu} = \sigma_{y_\mp,y_\mp} \tag{5.24}$$

We see that $x_-, y_+$ are amplified quadratures with variances that grow as $\mu \to 1$, while $x_+, y_-$ are squeezed quadratures showing reduction in the variance and hence a peak noise squeezing of $\frac{1}{2}$ (3 dB) as $\mu \to 1$, as can be seen from the solid black curves in Fig.[5.4], showing the variances of amplified and squeezed quadratures as a function $\mu$ for $\delta = \delta_\omega = 0$.

The reason for the bound for the peak noise squeezing is transparent when we

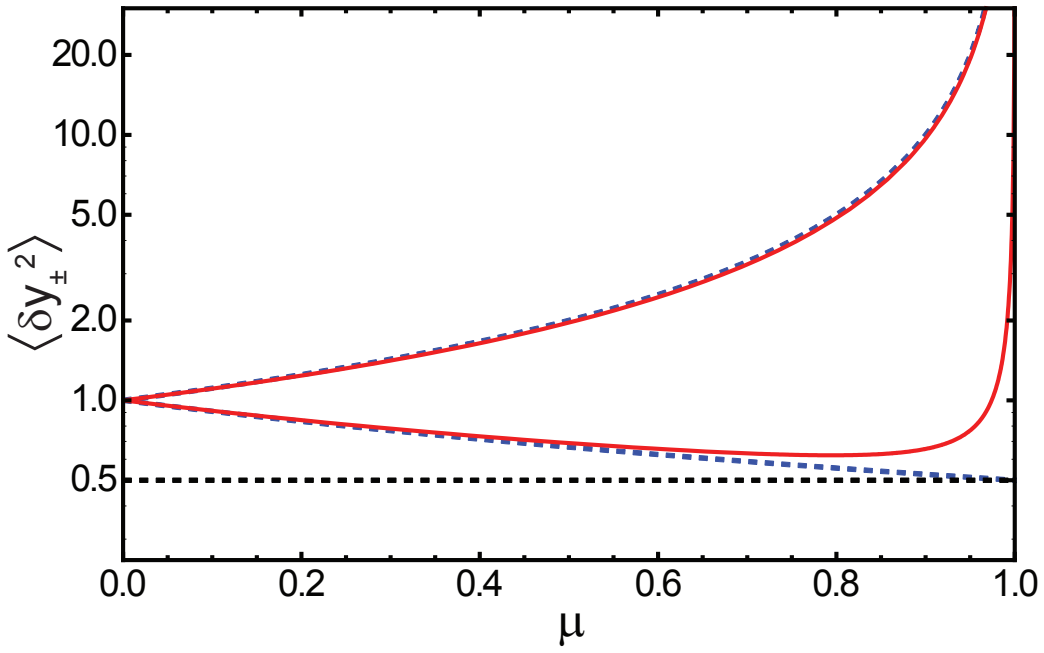


Figure 5.4: Normalized variances of amplified and squeezed collective quadratures as a function of the normalized parametric drive, the dashed blue lines indicate the variances for oscillators with identical frequencies ($\delta_\omega = 0$) and loss rates ($\delta = 0$). Solid red lines indicate the amplified and squeezed variances for $\delta = 0.31$, $\delta_\omega = 0.09$.

look at the equations of motion for the collective quadratures, through a rotation of $\mathbf{M}_{\alpha,\beta}$, i.e.,

$$\dot{\mathbf{X}} = \mathbf{M}_X \mathbf{X} + \mathbf{v'}_X \tag{5.25}$$

$$\dot{\mathbf{Y}} = \mathbf{M}_Y \mathbf{Y} + \mathbf{v'}_Y \tag{5.26}$$

where,

$$\mathbf{M}_{X,Y} = \mathbf{R}\mathbf{M}_{\alpha,\beta}\mathbf{R}^T = -\frac{1}{2}\begin{pmatrix} \gamma(1 \pm \mu) & 0 & 0 \\ 0 & \gamma(1 \mp \mu) & 0 \\ 0 & 0 & \gamma_s \end{pmatrix}$$

and $\mathbf{v}' = \mathbf{R}\mathbf{v}$ results in noise with the same diffusion matrix $\mathbf{D}$ as before, with $\mathbf{D}_{XX} = \mathbf{D}_{YY} = \gamma \frac{k_B T}{m\omega^2}$, as the baths of the two modes are uncorrelated.

The squeezing arises from the fact that while the thermal forces (fluctuations) remain the same in the presence/absence of the parametric drive, as $\mu \to 1$, the dissipation of the squeezed quadrature goes to twice its bare value, resulting in a reduction in the variance by a factor of 2. Simultaneously, the decay rate of the amplified quadrature goes to zero, signaling the onset of the parametric instability. The onset of the instability thus explains the 3 dB bound for squeezing. This is generically true for squeezing through parametric processes, in the absence of feedback.

We note that in the above, we have assumed that the bandwidth of detection is large enough that all the thermal noise is measured, i.e., the variances described above were calculated by integrating the noise over all frequencies, i.e., they are as measured with a lock-in amplifier with an infinite bandwidth ($BW$). As $BW \to 0$,

$$\frac{S_{x_+,x_+}(\omega = 0, \mu)}{S_{x_+,x_+}(\omega = 0, \mu = 0)} = \frac{1}{(1+\mu)^2} \to \frac{1}{4} \tag{5.27}$$

resulting in a peak noise squeezing approaches 6 dB. The above analysis was for the simplest case of symmetric frequencies and loss rates. The introduction of asymmetries in the frequencies and loss rates is detrimental to squeezing, as we will see in the next section.

### 5.6.2 Effect of asymmetric frequencies and loss rates

We now consider the case where the frequencies and the damping rate of the two resonators are not the same, i.e., $\delta, \delta_\omega \neq 0$. In this situation, the collective quadratures $x_+, x_-$ and correspondingly $y_+, y_-$, defined as per Eqns.[5.18,5.19],

are no longer decoupled from each other, as they were for the symmetric case previously considered. This coupling between collective quadratures, resulting from non-zero loss and frequency asymmetry has been noted to be detrimental to entanglement[70], and backaction evasion[72] protocols involving two coupled modes, coupled either mechanically or through a mode of an optical cavity. It also results in a degradation of peak two-mode thermomechanical squeezing, from the 3 dB limit. This is a result of the coupled quadratures $x_+, x_-$ and $y_-, y_+$ being respectively, amplified and squeezed in the presence of the parametric drive, as can be seen from Eqn.[5.24].

The variances of the collective quadratures are obtained using Eqn.[5.15], subsequent rotation using Eqn.[5.21] and integration over frequency, and are,

$$\begin{aligned} \sigma_{y_\pm, y_\pm} &= \sigma_{x_\mp, x_\mp} \\ &= \frac{1}{1-\mu^2}\left\{1 + \mu^2 \frac{\delta_\omega(\delta_\omega - \delta)}{1-\delta_\omega^2} \pm \mu\sqrt{\frac{1-\delta^2}{1-\delta_\omega^2}}\right\} \end{aligned} \tag{5.28}$$

with the cross correlation between $(x_+, x_-)$, $(y_+, y_-)$ given by,

$$\sigma_{y_+, y_-} = \sigma_{x_+, x_-} = \frac{\mu^2(\delta_\omega - \delta)}{2(1-\mu^2)(1-\delta_\omega^2)} \tag{5.29}$$

The variances of the amplified(blue, solid) and squeezed (red, solid) collective quadratures for the case where ($\delta \neq 0, \delta_\omega \neq 0$, $\delta \neq \delta_\omega$), are shown in Fig.[5.4], showing a peak noise squeezing of the squeezed quadrature of greater than $\frac{1}{2}$ the thermal variance, and with the maximum squeezing occurring for $\mu < 1$. We find that any coupling between the amplified and squeezed quadratures leads to a divergence of the squeezed quadrature at the instability threshold, in the steady state. The dependence of the peak squeezing on the loss and frequency asymmetry parameters are shown in Fig.[5.5]. Fig.[5.5(a)] shows a plot of the peak squeezing as a function of the loss asymmetry for the case of distinct mechanical modes with the same frequency ($\delta_\omega = 0$), showing a linear dependence of peak squeezing versus

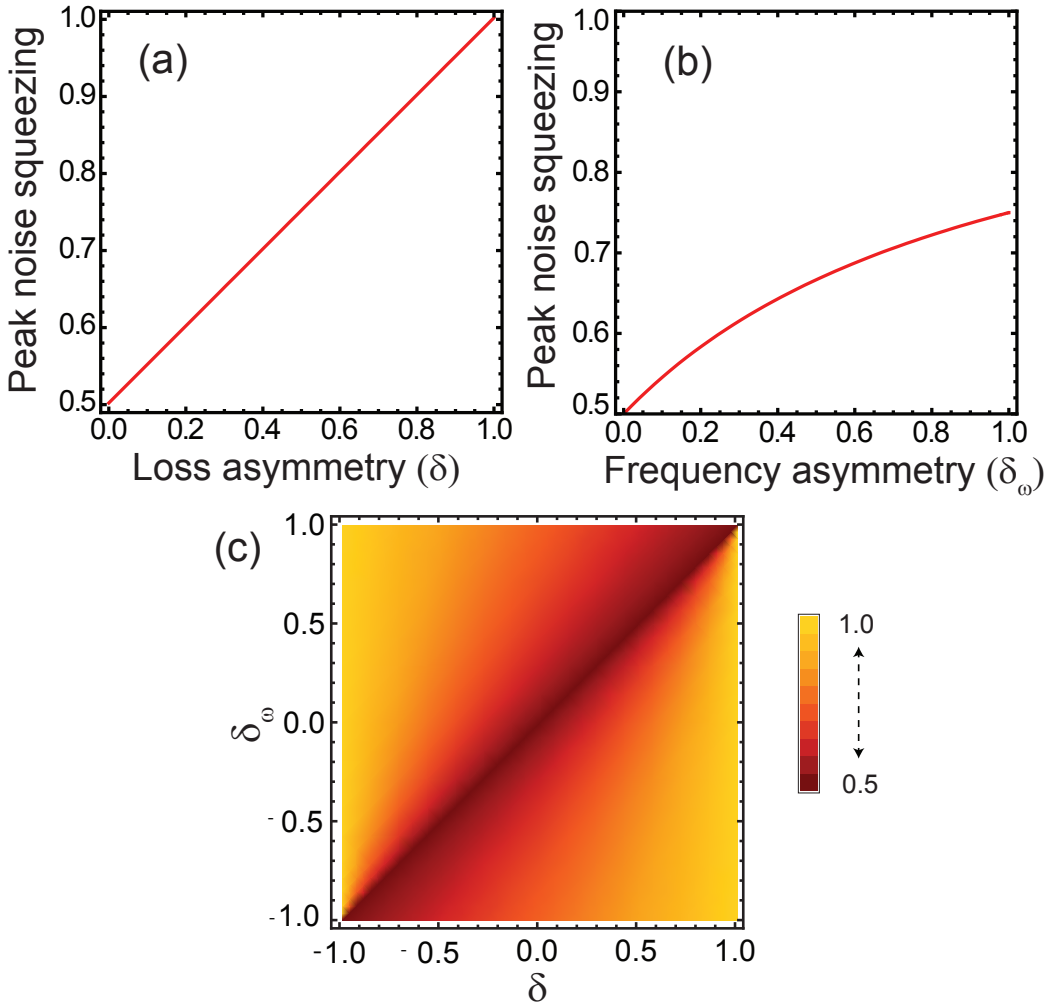


Figure 5.5: (a) Peak noise squeezing as a function of loss asymmetry $\delta$ for $\delta_\omega = 0$ with the squeezing going linearly from $\frac{1}{2} \rightarrow 1$ as $\delta = 0 \rightarrow 1$. (b) Peak squeezing as a function of the frequency asymmetry $\delta_\omega$, for $\delta = 0$. (c) Plot of peak squeezing as a function $\delta$ and $\delta_\omega$

the loss asymmetry. Correspondingly, Fig.[5.5(b)] shows the peak squeezing as a function of the frequency mismatch parameter ($\delta_\omega$) for the case of no loss asymmetry ($\delta = 0$), while Fig.[5.5(c)] shows a density plot of the minimum squeezing as a function of $\delta$ and $\delta_\omega$.

As can be seen in Fig.[5.5(c)], we find that the minimum squeezing of $\frac{1}{2}$ can be attained whenever $\delta = \delta_\omega$. For this case, the normalized cross correlations be-

tween amplified and squeezed collective quadratures, still vanish and Eqn.[5.28] reduces to Eqn.[5.24], resulting in a squeezing as a function of the parametric drive strength that is identical to that for $\delta = \delta_\omega = 0$, the case of symmetric losses and frequencies.

### 5.6.3 Effect of pump detuning

Before proceeding to the above threshold case, we consider the thermomechanical squeezing bound for the case where the pump drive is detuned from parametric resonance, with the drive frequency given by $\omega_d = \omega_S + \Delta$, where $\Delta$ is the drive detuning. Apart from our interest in checking the robustness of two-mode squeezing as a function of the detuning, this case is of interest since a detuned parametric drive introduces dynamic correlations between the $\delta\vec{\alpha}$ and $\delta\vec{\beta}$ quadratures, which in turn lead to correlations between the amplified and squeezed $x_\pm$ and $y_\pm$ quadratures. These correlations are different from those arising as a result of the asymmetry in loss rates/frequencies on account of the fact that, the correlations are between quadratures that exert a back action on each other, i.e., $x_\pm, y_\pm$ are observables that do not commute with each other, unlike $(x_+, x_-)$, $(y_+, y_-)$, which commute with each other. These correlations allow for enhanced squeezing in the presence of feedback, since the correlations in the amplified quadrature now have information about the squeezed quadrature which can be used for enhanced localization through estimation[77]. Additionally in the detuned two-mode case, like the one we consider, special choices of the drive detuning lead to some of the collective quadratures becoming quantum non-demolition observables[70]. The bound for the two-mode squeezing is calculated by similar means as before, and is detailed the Appendix of the chapter, with time independent equations (Eqn.[5.41]) for the

mechanical motion obtained by going to a frame rotating at $\Delta/2$ for each mode. As is shown there, the correlations between the $x_\pm$ and $y_\pm$ are proportional to the drive detuning. Note that $x_+$ and $y_-$ are amplified quadratures while $x_-$ and $y_+$ are squeezed. Again non zero detuning introduces correlations between $(x_+, y_+)$

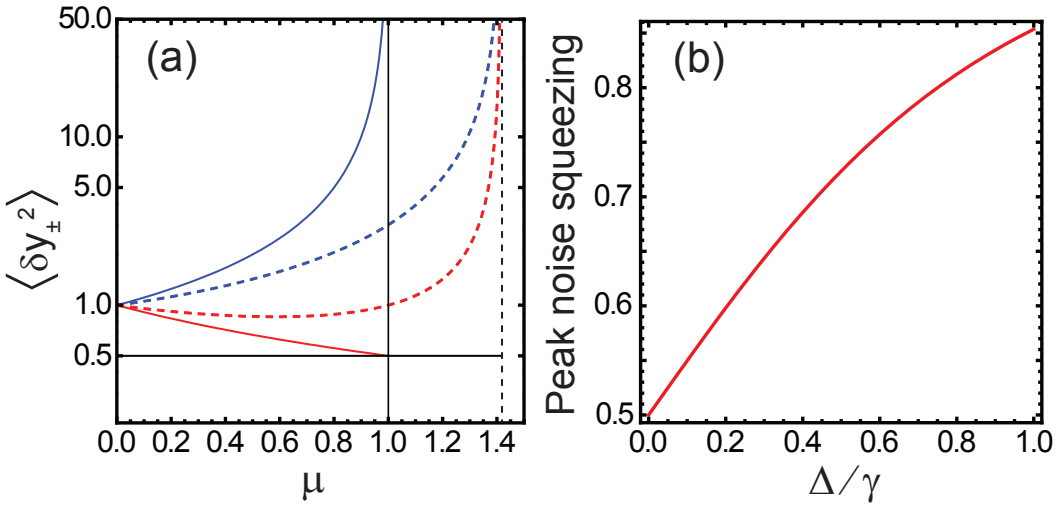


Figure 5.6: (a) Normalized $y_+$ (amplified,blue) and $y_-$ (squeezed,red) quadratures for the case of zero detuning (solid lines) and a detuning of $\Delta = \gamma$ (dashed lines). The amplified quadrature diverges at the instability threshold. For $\Delta = 0$, this occurs at $\mu = 1$ (solid black vertical line). For $\Delta/\gamma$, this occurs at $\mu = \sqrt{1 + (\Delta/\gamma)^2} = \sqrt{2}$ (dashed black vertical line). The black horizontal line is at 1/2. (b) Peak noise squeezing as a function of normalized detuning $\frac{\Delta}{\gamma}$, below threshold for the case of no loss/frequency asymmetry.

and $(x_-, y_-)$, i.e., between amplified and squeezed quadratures. This is distinct from the case of loss/frequency asymmetry, which introduced correlations between $(x_+, x_-)$ and $(y_+, y_-)$. This coupling between amplified and squeezed quadratures also results in a decrease in the peak squeezing at non-zero detunings, as can be seen in Fig.[5.6(a)]. Here, the solid lines correspond to amplified (blue) and squeezed (red) quadratures for $\Delta = 0$, with the squeezed quadrature showing a peak noise squeezing of 3 dB (infinite bandwidth), as $\mu \to 1$. The dashed lines correspond to

amplified (blue) and squeezed (red) quadratures for a detuning of $\Delta = \gamma$. For the detuned case, the amplified quadrature diverges at $\mu = \sqrt{1 + (\Delta/\gamma)^2}$, the instability threshold for $\Delta \neq 0$, as expected.

The peak squeezing as a function of the detuning, normalized with respect to the decay rate (for no loss/frequency asymmetry) is shown in Fig.[5.6(b)]. We see that squeezing is almost completely lost by the time the detuning equals to the linewidth of the signal and idler modes.

### 5.6.4 Corrections arising from finite measurement time

The discussion of the preceding sections predicts an upturn in the variance of the squeezed quadrature, for the case of non-zero and unequal loss and frequency asymmetry, as the drive approaches the parametric instability threshold, i.e., $\mu \rightarrow 1$. This predicted upturn in the steady state variances of the squeezed quadrature is not seen in the experimental data presented in Sec.[5.4](See Fig.[5.3]). The reason for this arises from considerations of the time scale of measurement, which is large enough that the measured variances of the thermal motion, in the absence of the parametric drive, are within 5% of the steady state thermal variance(see Fig.[5.3] as $\mu \rightarrow 0$).

As was seen in Sec.[5.6.1], the gain of the amplified quadrature, and the steady state variance resulting from the gain in the amplified quadrature diverges as $\mu \rightarrow 1$. This is a result of the effective damping rate of the amplified quadrature, $\gamma(1-\mu)$, going to zero, as the drive approaches the parametric instability threshold. This is the quality factor enhancement seen in parametric amplifiers[78], which results in the increased sensitivity of the amplifier to a narrow bandwidth coherent force

at the mechanical frequency.

This vanishing of effective damping rate however, also results in a divergence in the response time. The divergence in the response time results in deviations of the measured variances from the steady state variance for a finite measurement time ($\tau_m$). results in a smoothing out of the divergence of the amplified quadrature. The variances measured over a finite time are extracted by truncating the integral in Eqn.[5.17], by the time of measurement, i.e.,

$$\boldsymbol{\sigma}_{\alpha,\beta} = 2\int_{\frac{2\pi}{\tau_m}}^{\infty} \mathbf{S}_{\alpha,\beta}(\omega)d\omega \tag{5.30}$$

The variances of the amplified (blue) and squeezed(red) quadratures extracted using Eqn.[5.30], for the parameters in Fig.[5.2] are shown in Fig.[5.7](a) as a function of the normalized drive, for various times of measurement. Fig.[5.7](b) shows the

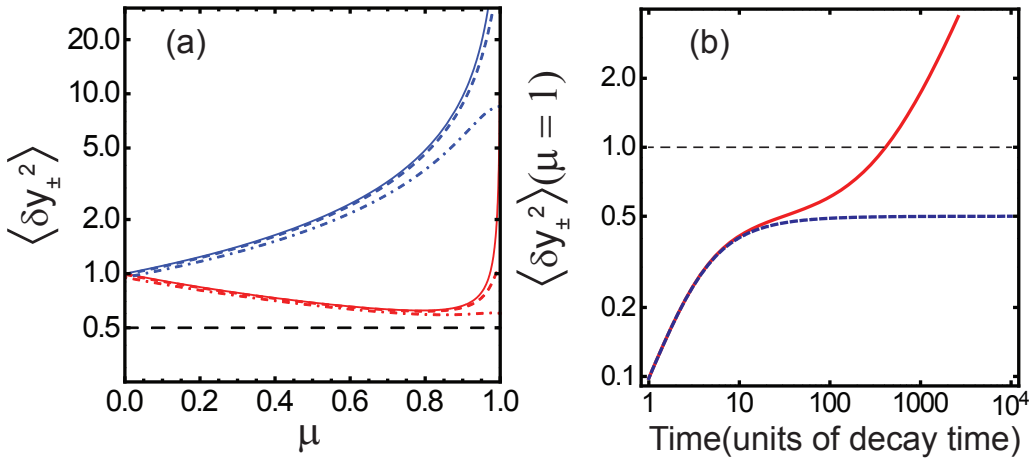


Figure 5.7: (a) Variance of amplified (blue) and squeezed (red) quadratures as a function of the normalized parametric drive ($\mu$) for steady state (solid lines), $\tau_m = 100\tau$ (dot-dashed lines) and $\tau_m = 500\tau$ (dashed lines) (b) Variance of the squeezed quadrature as a function of time (normalized to the decay time) for the experimental parameters of Fig.[5.2] (solid red curve) and corresponding variance for the case, $\delta = \delta_\omega = 0$ (where there is no coupling to the amplified quadrature).

variance of the squeezed quadrature at ($\mu = 1$) as a function of the measurement time. We see that in the absence of coupling to the amplified quadrature, the squeezed quadrature variance approaches the steady state value within a period of $\sim 100\tau$, where $\tau$ is the decay time of the mechanical mode (dashed blue curves). In contrast, for the case of asymmetric frequencies and losses (experimental parameters of Fig.[5.2]), the coupling to the amplified quadrature leads to an increase in the variance of the squeezed quadrature over a longer time scale as a result of the enhanced decay/response time of the amplified quadrature. We note that for corresponding two-mode squeezing experimental data in [57], loss and frequency asymmetries predict an upturn in the squeezed quadrature, which is realized in the experiment because of the orders of magnitude smaller decay time (and quality factors), and a similar measurement time.

In the preceding sections, we calculated the degree of two-mode quadrature squeezing, for the case of of a parametric drive below the instability threshold, paying attention to dependence on loss and frequency asymmetries, drive detuning and effects arising from finite measurement time. We were motivated in doing so in order to obtain a quantitative understanding of our experimental demonstration of two-mode thermomechanical squeezing described in Sec.[5.4]. A significant, but not the entire reason for interest in two-mode squeezing is the extension of such two-mode squeezing to the quantum regime[52], a realistic possibility given the current status of cavity optomechanics. Our demonstration of a strong two-mode nonlinearity, in a platform compatible with ground state cooling of the mechanical modes is a step in this direction. In the quantum regime, two-mode squeezing with a variance of half the quantum variance will lead to an entangled state of the macroscopic mechanical modes. It is straightforward to extend the calculations performed here to that case, with thermal noise now replaced by quantum noise.

The thermomechanical squeezing calculations were themselves inspired by analysis of quantum two-mode squeezing in optical parametric amplifiers[79, 80].

The other reason for interest in squeezing is for metrology in the classical regime. A naive explanation for the increased sensitivity afforded by thermomechanical squeezing might be the transduction of a smaller force resulting from the reduction of the thermal noise floor. However, as we have seen, the squeezing arose from the increased damping of the squeezed quadrature. This actually renders the squeezed quadrature less sensitive to the force. Taking advantage of squeezing for metrology, as in the optical case, requires interferometric measurements, mechanical analogues of which have been recently proposed[74]. With the possibility of such interferometric schemes in mind, we proceed to look at two-mode squeezing, above the parametric instability threshold.

## 5.7 Amplitude difference squeezing above threshold

An optical parametric oscillator, with the pump driven above the parametric instability threshold produces entangled signal and idler photons. This entanglement results in the signal and idler beams having shot noise that is exactly correlated. This results in intensity difference squeezing, where the intensity difference of the signal and idler modes is below shot noise [80].

We here discuss analogous above threshold behavior seen in a mechanical nondegenerate parametric amplifier, where now, the difference in the amplitudes of the signal and idler modes above threshold has a variance that is below thermal variance, i.e., the amplitude difference is squeezed. In addition to amplitude difference squeezing another interesting feature of this is system concerns the fluctuations of the phases of the membrane modes. Above threshold, the sum of the phases of

the membrane modes, is locked to the phase of the pump drive. This can be seen from Eqn.[5.3], which in steady state can be rewritten in terms of the normalized drive $\mu$ and the drive force phase $\phi_S$ ($F_S = |F_S|e^{i\phi_S}$) as,

$$-(\mu-1)e^{i\phi_S} = \frac{g}{2}\frac{\chi_S}{|A_{S,th}|}A_iA_j \tag{5.31}$$

Defining the phases of the resonator modes as $A_{i,j} = i|A_{i,j}|e^{i\phi_{i,j}}$, we have,

$$\phi_i + \phi_j = \phi_S \tag{5.32}$$

Note that the difference in the phases is however not constrained by these equations and is free to fluctuate.

We obtain the fluctuations in the amplitudes and phases about the steady state values by decomposing the complex amplitude fluctuations $\delta\vec{A}$ into $\delta\alpha_i$ and $\delta\beta_i$ quadratures, i.e $\delta\vec{A} = \delta\vec{\alpha} + i\delta\vec{\beta}$, with the equations of motion of $\delta\vec{\alpha}$ and $\delta\vec{\beta}$ given by Eqns.[5.42, 5.43], with the evolution matrices $\mathbf{M}_{\alpha,\beta}$ given by Eqn.[5.14], after substituting $|\bar{A}_S| = \sqrt{\frac{\gamma_i\gamma_j}{\kappa_i\kappa_j}}$ and $\bar{A}_{i,j} = \sqrt{\frac{\gamma_i\gamma_S}{\kappa_i\kappa_S}}\sqrt{\mu-1}$, the mean amplitude of the pump substrate mode and the probe modes above threshold.

We have chosen the drive and detection phases such that $\bar{\phi}_{i,j} = \phi_S = 0$. Given this choice of phases, the complex mean amplitudes $\bar{A}_i$ and the fluctuations are as shown in the inset of Fig.[5.8]. $\delta\beta_{i,j} = \delta R_{i,j}$ give the amplitude fluctuations. The fluctuations in the phase are obtained from $\delta\alpha_{i,j}$through $\delta\phi_{i,j} = \frac{\delta\alpha_{i,j}}{\bar{A}_{i,j}}$.

As for the below threshold case, the correlations of the signal and idler modes resulting from the pump drive are manifest in combined quadratures,

$$x_\pm = \frac{1}{\sqrt{2}}(\delta\alpha_i \pm \delta\alpha_j) \propto \delta\phi_\pm \tag{5.33}$$

$$y_\pm = \frac{1}{\sqrt{2}}(\delta\beta_i \pm \delta\beta_j) = \delta R_\pm \tag{5.34}$$

where $\delta R_\pm$ are the amplitude sum and difference quadratures and $\delta\phi_\pm$ are the phase sum and difference quadratures. The spectrum of fluctuations of $\delta\alpha_\pm$ and

$\delta\beta_{\pm}$ are given by Eqn.[5.15] in Sec.[5.5].

For the above threshold case, the non-zero amplitudes of the signal and idler membrane modes cause the fluctuations of the pump mode to now affect their correlations, unlike in the below threshold case. Given that the damping rate of the

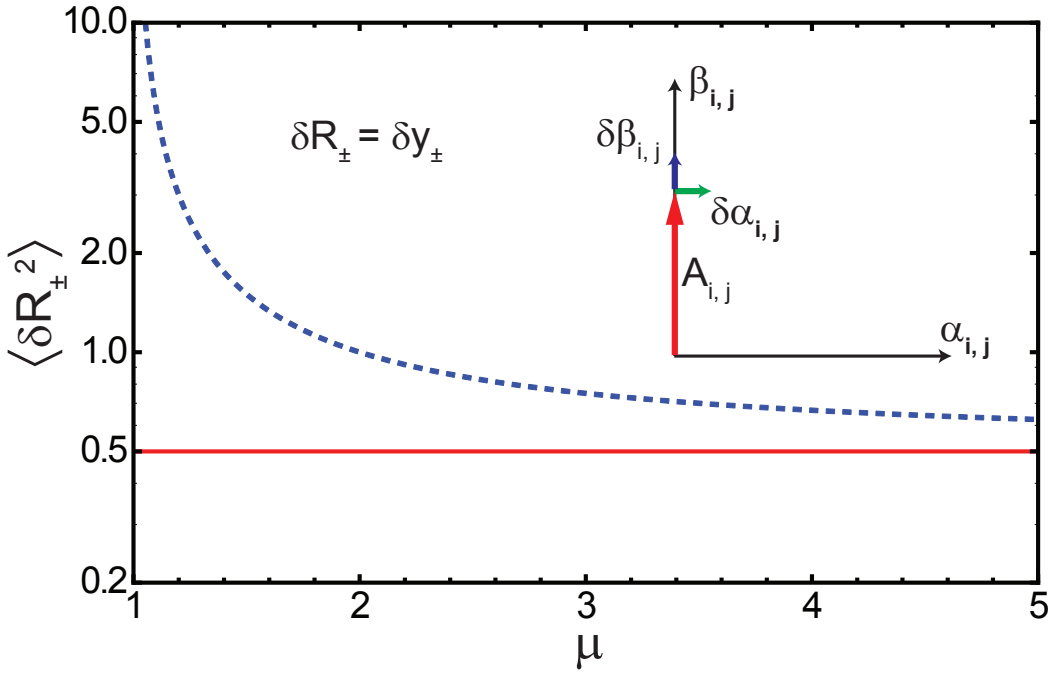


Figure 5.8: Variance of the difference ($\delta R_-$) (red, solid) and sum ($\delta R_+$) (blue, dashed) of the normalized amplitude fluctuations of the signal and idler modes, as a function of the parametric drive strength $\mu$, for $\delta = \delta_\omega = 0$. The variances are scaled to the thermal motion. The amplitude difference is squeezed for all values above threshold to a value of $\frac{1}{2}$ the thermal variance. (Inset) Schematic showing the mean value of the membrane mode amplitude and the fluctuations $\delta\alpha_i$ and $\delta\beta_i$. $\delta\vec{\beta}$ represent amplitude fluctuations while $\delta\vec{\alpha}$ are related to fluctuations of the phase.

substrate mode is 4-5 orders of magnitude larger than that of the modes of the mechanical resonator, the pump fluctuations responds instantaneously to those of the membrane modes and can be adiabatically eliminated. We use this to simplify the analysis, through ignoring the time derivative of the pump fluctuations

($\delta \dot{A}_S$) in Eqn.[5.8]. Apart from this change, we extract the fluctuations of the cross quadratures of the signal and idler modes, using the methods of Sec.[5.5], using Eqn.[5.15] and subsequent rotation through Eqn.[5.21].

We consider for simplicity the case where the damping rates and the frequencies are symmetric. In this limit, we obtain the following spectra for the collective quadratures, normalized with respect to the thermal motion amplitude.

$$\mathbf{S}_Y(\omega) = \frac{1}{2\pi} \begin{pmatrix} \frac{\gamma\mu}{(\gamma^2(-1+\mu)^2+\omega^2)} & 0 \\ 0 & \frac{\gamma}{(\gamma^2+\omega^2)} \end{pmatrix} \tag{5.35}$$

$$\mathbf{S}_X(\omega) = \frac{1}{2\pi} \begin{pmatrix} \frac{\gamma\mu}{(\gamma^2\mu^2+\omega^2)} & 0 \\ 0 & \frac{\gamma}{\omega^2} \end{pmatrix} \tag{5.36}$$

We obtain the variances of the fluctuations by integrating the spectra. For the $Y$ quadrature, which relates to amplitude fluctuations, these evaluate to

$$\sigma_{y_+,y_+} = \sigma_{R_+,R_+} = \frac{\mu}{2\,(\mu-1)} \tag{5.37}$$

$$\sigma_{y_-,y_-} = \sigma_{R_-,R_-} = \frac{1}{2} \tag{5.38}$$

These variances are plotted as a function of the parametric drive strength in Fig.[5.8] (Sum; dashed blue, Difference; solid red).

We see that above threshold, the amplitude difference of the signal and idler modes is always $\frac{1}{2}$ the thermal variance, which is the mechanical analogue of intensity difference squeezing seen in optical parametric oscillators. We find that while the individual amplitudes are sensitive to fluctuations of the pump mode, the amplitude difference is insensitive to pump mode fluctuations, and the degree of squeezing is independent of the pump drive. The variance of the amplitude sum on the other hand diverges as $\mu \to 1^+$ and decreases with increasing drive, approaching $\frac{1}{2}$ the thermal variance as $\mu \to \infty$.

Having discussed the fluctuations in the amplitude, we now consider the other dis-

tinguishing feature of above threshold behavior, the fluctuations in the phase. As has been discussed earlier, the phase difference between the signal and idler modes, above threshold, is unspecified and therefore free to fluctuate. This fluctuation in the phase difference is given by,

$$\begin{aligned} S_{\phi_-,\phi_-}(\omega) &= \left(\frac{x_{th}^2}{A(\mu)^2}\right) S_{x_-,x_-}(\omega) \\ &= \left(\frac{x_{th}^2}{A(\mu)^2}\right)\left(\frac{\gamma}{2\pi\omega^2}\right) \end{aligned}$$

where $A(\mu)$ is the amplitude of the membrane modes (identical for the case of symmetric loss), $x_{th}^2$ is the thermal variance. We see that the integral of the fluctuation spectrum diverges as $\omega^{-2}$, indicating that the difference phase diffuses. The time scale for this diffusion can be estimated by calculating the variance while imposing a low frequency cut off ($\frac{2\pi}{\tau_m}$) to the integral of the power spectrum, i.e.,

$$\begin{aligned} \langle \delta\phi_-^2 \rangle &= 2\int_{\frac{2\pi}{\tau_m}}^{\infty} S_{\phi_-,\phi_-}(\omega) d\omega \\ &= \left(\frac{x_{th}^2}{A(\mu)^2}\right)\frac{\gamma\tau_m}{2\pi^2} \end{aligned}$$

If the thermal motion amplitude were 0.1 pm and the two-mode nonlinearity were used to excite the membrane mode to $\sim$ 1 nm, a difference phase fluctuation of $\sqrt{\langle \delta\phi_-^2 \rangle} \sim 1\ mrad$ would require $\sim$ 1000 ringdown periods. Therefore, while $S_{\phi_-,\phi_-}(\omega)$ diverges, it does not necessary lead to large fluctuations of the difference phase over experimental time scales.

### 5.7.1 Distinction between squeezing above and below threshold

Both below and above threshold, the squeezing is manifested in a quadrature formed from the linear combination of those of the individual mechanical resonators

$(x_\pm, y_\pm)$. However, below threshold, this manifests as quadrature squeezing, while above threshold, this manifests as amplitude difference squeezing. Additionally, there is no analogue of the phase diffusion phenomenon discussed in the previous section, below threshold.

The fluctuations of the quadratures of the individual resonators are symmetric below threshold. Above threshold, the non zero amplitude of the signal and idler mode breaks this symmetry, leading to amplitude and phase fluctuations with different correlations.

This is reminiscent of behavior seen at a phase transition, the complex amplitude of the signal and idler mode being like an order parameter[81]. The difference in the fluctuations between the below and above threshold cases is akin to the difference in the nature of the fluctuations about a disordered phase, and those about an ordered phase. Much as in the case of a phase transition with a complex order parameter, where there are fluctuations in the ordered phase which cost no energy, here, above threshold, the difference phase between the signal and idler mode is unspecified and free to fluctuate, with its fluctuations costing no energy.

We show the fluctuations in the quadrature $\delta y_\pm$, which becomes the amplitude difference quadrature in the above threshold case, as a function of the parametric drive for both the below and above threshold cases, in Fig.[5.9]. We see that for the case of symmetric losses and frequencies, the variance of the squeezed quadrature approached half at the threshold and remains there (dashed red curve). At $\mu = 1$, the susceptibility of the amplified quadrature diverges, this divergence in the susceptibility is associated also with a divergence in the response time, which leads to a similar divergence of the squeezed quadrature in case of coupling between amplified and squeezed quadratures (solid red and blue curves); as in the case with non zero loss and frequency asymmetry. For finite measurement time, the divergence

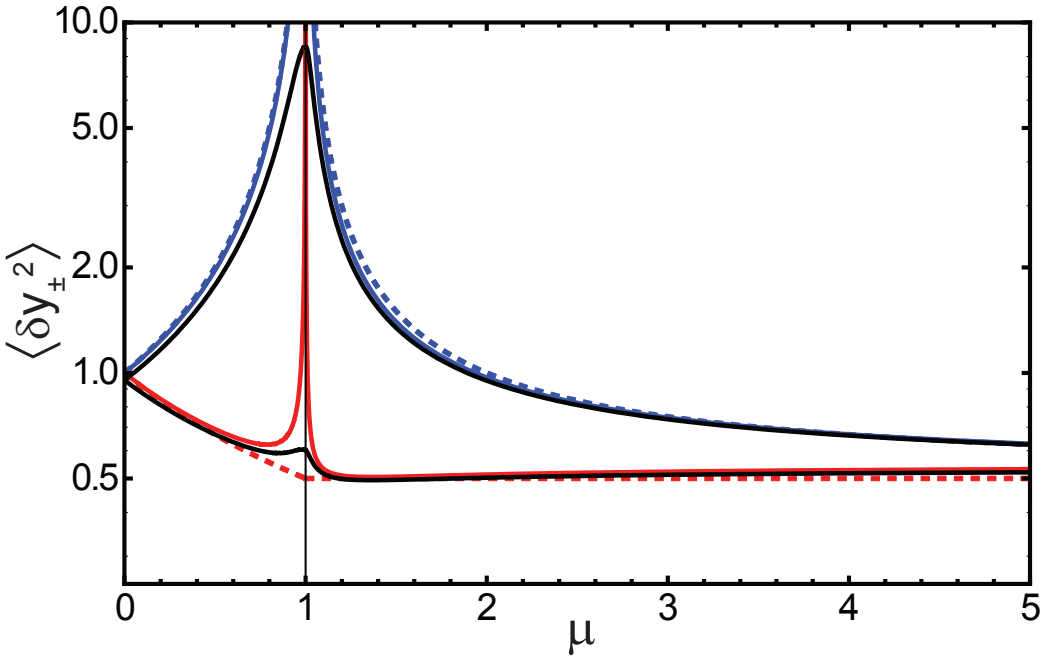


Figure 5.9: Variance of the fluctuations of the normalized difference ($y_-$) and sum ($y_+$) quadratures above and below threshold, as a function of the normalized parametric drive strength $\mu$. For the case of no loss and frequency asymmetry these are represented by the dashed red ($y_-$) and blue curves($y_+$). For the experimental parameters of Fig.[5.3] ($\delta = 0.31, \delta_\omega = 0.09$), these are represented by the solid red ($y_-$) and blue curves($y_+$). The black solid lines are the corrections to the variances arising from a finite measurement time of $300s$ ($\sim 100\tau$) for this case.

of the amplified quadrature is washed out (Black curve; $\tau_m = 100\tau$).

The above discussion described the fluctuations of a mechanical parametric amplifier, and their correlations for the case where the parametric drive is above threshold. We saw that there is a manifestation of squeezing in this case as well, with the amplitude difference of the mechanical modes being reduced to half the thermal variance; the analogue of intensity difference squeezing in optical parametric oscillators[76].

## 5.8 Conclusions

We have demonstrated strong two-mode parametric nonlinearities in an ultrahigh-Q membrane resonator, realizing nondegenerate parametric amplification and two-mode thermomechanical noise squeezing. Our experimental observations are in agreement with a two-mode model attributing the nonlinear interaction to a substrate mediated coupling between the mechanical modes.

The realization of this strong nonlinear interaction in a mechanical platform that is compatible with optomechanical cooling, room temperature quantum control and quantum limited detection is an important step towards the realization of non-classical mechanical states, the observation of entanglement between macroscopic mechanical degrees of freedom and quantum enhanced metrology.

The parametric coupling demonstrated here is of relevance for quantum non-demolition[71] and backaction evading measurement[72] protocols for the measurement of the position of the mechanical resonator and is therefore crucial for the realization of position measurements beyond the standard quantum limit[73].

Even in the classical regime, this work is of relevance for nonlinear approaches to metrology. The correlated production of down-converted phonons above the parametric instability threshold holds promise for interferometric measurement schemes capable of beating the limitations set by thermal noise[74, 75].

Furthermore, the regime near the parametric instability threshold is characterized by a diverging response time and mechanical bistability. Here the system realizes a mechanical analog of a second-order phase transition. In this regime, compatibility with optomechanical cooling allows access to studies of the quantum-classical transition[82] and out-of-equilibrium quantum dynamics.

## 5.9 Appendix: Effect of pump detuning

We calculate here the thermomechanical squeezing bound for the case where the pump drive is detuned from parametric resonance, with the drive frequency given by $\omega_d = \omega_S + \Delta$, where $\Delta$ is the drive detuning. The equations satisfied by the slowly varying complex amplitudes ($A_{i,j,S}$) are again given by Eqns.[5.1-5.3], with the only difference now being that the pump drive force $\tilde{F}_S(t)$ is a slowly varying function of time, $\tilde{F}_S(t) = |\tilde{F}_S|e^{-i\Delta t}$. The pump amplitude resulting from this drive force, $\bar{A}_S(t)$ is given by,

$$\bar{A}_S = i\chi_S \tilde{F}_S(t) = i\chi_S |\tilde{F}_S| e^{-i\Delta t} = i|\bar{A}_S|e^{-i\Delta t} \tag{5.39}$$

We have made the approximation that $\Delta << \gamma_S$, given that we are interested in detunings that are comparable to $\gamma_{i,j}$ and $\gamma_{i,j} \approx 10^{-4}\gamma_S$ as a result of which the pump amplitude is related to the instantaneous force through the on resonant susceptibility.

Linearizing about the steady state amplitude, i.e., $A_k = \bar{A}_k + \delta A_k(t)$ where $k \in [i, j, S]$, with $\bar{A}_{i,j} = 0$, and defining the vectors $\delta\vec{A} = (\delta A_i, \delta A_j)^T$ and $\delta\vec{v} = (v_i, v_j)^T$, the relevant equations of motion for the fluctuations of the resonator modes reduce to,

$$\begin{aligned} 2\delta\dot{\vec{A}} &= -\begin{pmatrix} \gamma_i & 0 \\ 0 & \gamma_j \end{pmatrix} \delta\vec{A} \\ &- \begin{pmatrix} 0 & \kappa_i|\bar{A}_S|e^{-i\Delta t} \\ \kappa_j|\bar{A}_S|e^{-i\Delta t} & 0 \end{pmatrix} \delta\vec{A}^* + 2\vec{v} \end{aligned} \tag{5.40}$$

We get rid of this time dependence in the matrix above by going to a frame rotating at $\frac{\Delta}{2}$, i.e., we rewrite $\delta\vec{A} = \delta\vec{B}e^{\frac{i\Delta t}{2}}$ in terms of which Eqn.[5.40] becomes,

$$\begin{aligned} 2\dot{\delta\vec{B}} &= -\begin{pmatrix} \gamma_i & 0 \\ 0 & \gamma_j \end{pmatrix}\delta\vec{B} - i\Delta\delta\vec{B} \\ &- \begin{pmatrix} 0 & \kappa_i|\bar{A}_S| \\ \kappa_j|\bar{A}_S| & 0 \end{pmatrix}\delta\vec{B}^* + 2\vec{v}e^{-\frac{\Delta t}{2}} \end{aligned} \tag{5.41}$$

where $\delta\vec{B}$ are the complex amplitudes, measured using lock-in frequencies that are detuned from the individual mechanical modes $\omega_{i,j}$ by $\frac{\Delta}{2}$. We rewrite the complex amplitudes in terms of the real quadratures $\alpha_{i,j}, \beta_{i,j}$ and decompose the noise term into real and imaginary parts, i.e., $\delta\vec{B} = \delta\vec{\alpha} + i\delta\vec{\beta}$ and $\vec{v} = \vec{v}_\alpha + i\vec{v}_\beta$, in terms of which the equations of motion become,

$$\dot{\delta\vec{\alpha}} = \mathbf{M}_\alpha\delta\vec{\alpha} - \frac{\Delta}{2}\delta\vec{\beta} + \vec{v}_\alpha \tag{5.42}$$

$$\dot{\delta\vec{\beta}} = \mathbf{M}_\beta\delta\vec{\beta} + \frac{\Delta}{2}\delta\vec{\alpha} + \vec{v}_\beta \tag{5.43}$$

where

$$\mathbf{M}_{\alpha,\beta} = \frac{1}{2}\begin{pmatrix} -\gamma_i & \mp\kappa_i|\bar{A}_S| \\ \mp\kappa_j|\bar{A}_S| & -\gamma_j \end{pmatrix} \tag{5.44}$$

and the elements of $\vec{v}_{\alpha,\beta}$ satisfy $\langle v_{k,\eta}\rangle \quad \eta \in [\alpha,\beta]; k \in [i,j]$ and $\langle v_{k,\eta}(t)v_{l,\eta'}(t+\tau)\rangle = \frac{\gamma_l k_B T}{m_l\omega_l^2}\delta_{kl}\delta_{\eta,\eta'}\delta(\tau)$. The coupling between the $\delta\vec{\alpha}$ and $\delta\vec{\beta}$ quadratures of the individual oscillators resulting from the detuned drive is apparent in Eqns.[5.42,5.43]. The steady state correlations between these quadratures can be obtained using the methods of Sec.[5.5] by forming the following 4 dimensional vectors; $\mathbf{Z} = (\delta\alpha_i, \delta\alpha_j, \delta\beta_i, \delta\beta_j)^T = (\delta\vec{\alpha}, \delta\vec{\beta})^T$ and $\mathbf{v} = (\vec{v}_\alpha, \vec{v}_\beta)^T$, in terms of which the

equations of motion become,

$$\dot{\mathbf{Z}} = \mathbf{M}\mathbf{Z} + \mathbf{v} \tag{5.45}$$

$$\mathbf{M} = \begin{pmatrix} \mathbf{M}_\alpha & -\frac{\Delta}{2}\mathbf{I}_2 \\ \frac{\Delta}{2}\mathbf{I}_2 & \mathbf{M}_\beta \end{pmatrix} \tag{5.46}$$

and $\mathbf{I}_2$ is the $2 \times 2$ identity matrix.

The noise spectral densities are now obtained by solving Eqn.[5.45] in fourier space, as before. The spectrum in the steady state is,

$$\begin{aligned} \mathbf{S}(\omega) &= \left\langle \mathbf{Z}(\omega)\mathbf{Z}(\omega)^\dagger \right\rangle \\ &= \frac{1}{2\pi}(\mathbf{M} + i\omega\mathbf{I})^{-1}\mathbf{D}(\mathbf{M}^T - i\omega\mathbf{I})^{-1} \end{aligned} \tag{5.47}$$

where $\mathbf{I}$ is the identity and

$$\mathbf{D} = \langle \mathbf{v}\mathbf{v}^T \rangle = k_B T \begin{pmatrix} \frac{\gamma_i}{m_i\omega_i^2} & 0 & 0 & 0 \\ 0 & \frac{\gamma_j}{m_j\omega_j^2} & 0 & 0 \\ 0 & 0 & \frac{\gamma_i}{m_i\omega_i^2} & 0 \\ 0 & 0 & 0 & \frac{\gamma_j}{m_j\omega_j^2} \end{pmatrix} \tag{5.48}$$

is now a $4 \times 4$ matrix, as is $\mathbf{S}(\omega)$, which contains the correlations between all the quadratures of the two modes.

We construct composite quadratures $x_\pm = (\alpha_i \pm \alpha_j)/\sqrt{2}$, $y_\pm = (\beta_i \pm \beta_j)/\sqrt{2}$ as before and represent the fluctuations in these quadratures by the column matrix, $\mathbf{Z}_c = (\delta x_+, \delta x_-, \delta y_+, \delta y_-)^T$, which is related to $\mathbf{Z}$ by

$$\mathbf{Z}_c = \mathbf{R}\mathbf{Z}; \quad \mathbf{R} = \frac{1}{\sqrt{2}} \begin{pmatrix} 1 & 1 & 0 & 0 \\ 1 & -1 & 0 & 0 \\ 0 & 0 & 1 & 1 \\ 0 & 0 & 1 & -1 \end{pmatrix} \tag{5.49}$$

The correlations of the composite quadratures are therefore given by,

$$\mathbf{S}_c(\omega) = \left\langle \mathbf{Z}_c(\omega)\mathbf{Z}_c(\omega)^\dagger \right\rangle = \mathbf{R}\mathbf{S}\mathbf{R}^T \tag{5.50}$$

We consider the case where the frequencies of the resonator modes are identical and the losses are symmetric ($\gamma_i = \gamma_2 = \gamma$, i.e., $\delta = 0$). For this case, the diffusion matrix $\mathbf{D} = k_B T \frac{\gamma}{m\omega^2}\delta_{ij}$.

The correlations between the composite quadratures in this case are given by,

$$\mathbf{S}_c(\omega) = \begin{pmatrix} S_{x_+,x_+} & 0 & S_{x_+,y_+} & 0 \\ 0 & S_{x_-,x_-} & 0 & S_{x_-,y_-} \\ S_{y_+,x_+} & 0 & S_{y_+,y_+} & 0 \\ 0 & S_{y_-,x_-} & 0 & S_{y_-,y_-} \end{pmatrix} \tag{5.51}$$

where the non zero correlations are indicated in the matrix above. There are no correlations between ($x_+$, $x_-$) and ($y_+$, $y_-$), given our choice of detection phases and the fact that we consider the case $\delta = \delta_\omega = 0$. The correlations in Eqn.[5.51] evaluate to,

$$\begin{aligned} S_{x_\pm,x_\pm}(\omega) &= S_{y_\mp,y_\mp}(\omega) \\ &= \frac{2d\left(\Delta^2 + \gamma^2(1 \mp \mu)^2 + 4\omega^2\right)}{\pi\left(4\omega^2 + \lambda_+^2\right)\left(4\omega^2 + \lambda_-^2\right)} \end{aligned} \tag{5.52}$$

$$\begin{aligned} S_{x_+,y_+}(\omega) &= S_{y_+,x_+}(\omega) \\ &= \frac{4d\Delta\left(\gamma\mu + 2i\omega\right)}{\pi\left(4\omega^2 + \lambda_+^2\right)\left(4\omega^2 + \lambda_-^2\right)} \\ &= S_{x_-,y_-}(-\omega) = S_{y_-,x_-}(-\omega) \end{aligned} \tag{5.53}$$

where $\lambda_\pm^2 = \gamma^2\left(1 + \mu^2\right) - \Delta^2 \pm 2\gamma\sqrt{\gamma^2\mu^2 - \Delta^2}$. The variances in the steady state obtained using the Weiner-Khinchtine theorem are,

$$\begin{aligned} \sigma_{x_\pm,x_\pm} &= \left(\frac{k_B T\gamma}{m\omega^2}\right)\left[\frac{\left(\Delta^2 + \gamma^2(1 \mp \mu)^2 - \lambda_-^2\right)}{\lambda_+\lambda_-\left(\lambda_+ + \lambda_-\right)} + \frac{1}{\lambda_+}\right] \\ &= \sigma_{y_\mp,y_\mp} \end{aligned} \tag{5.54}$$

Unlike the case of zero detuning, we obtain non-zero steady state correlations between the $x$ and $y$ quadratures,

$$\sigma_{x_\pm,y_\pm} = \left(\frac{k_B T\gamma}{m\omega^2}\right)\frac{2\Delta\gamma\mu}{\lambda_+\lambda_-\left(\lambda_+ + \lambda_-\right)} = \sigma_{y_\pm,x_\pm} \tag{5.55}$$

CHAPTER 6

# ACOUSTIC PHONONS AS PROBE OF ELECTRONIC NEMATICITY IN CUPRATE SUPERCONDUCTORS

## 6.1 Introduction

In the past decade, experimental evidence has been mounting for the existence of orientational symmetry broken phases in strongly correlated electronic systems [83]. The most clear cut evidence for such electronic nematic phases comes from temperature dependent transport anisotropies in high Landau level quantum hall systems [84], in the metallic regime of $Sr_3Ru_2O_7$ [85] and in the recently discovered iron pnictide superconductors [86],[87].

There is now also increasing evidence for nematic ordering in the pseudogap phase of underdoped cuprate high temperature superconductors. This has been seen through measurements of anisotropies in transport [88], the Nernst coefficient [89] and in spin modulations seen in neutron scattering experiments [90]. Additionally signatures of nematic ordering have also been seen in scanning tunneling microscopy [91],[92]. There is however still, a need for new probes of nematic order and nematic quantum criticality particularly when coexisting with superconductivity, which renders typical bulk probes for nematicity such as electrical and thermal transport unavailable.

This chapter discusses work done along with Prof. Eun-Ah Kim and Prof. Michael Lawler concerning using the underlying elastic medium as a probe for electronic nematic order and nematic quantum criticality inside the d-wave superconducting dome of cuprate superconductors.

This chapter is organized as follows. In section 6.2 we discuss the model for ne-

matic order inside a d-wave superconductor followed by a description of our model for coupling between the nematic d-wave superconductor and the underlying lattice in section 6.3. In sections 6.4 and 6.5, we proceed to evaluate the effect of the nematic d-wave superconductor on the lattice through the calculation of the effective elastic theory using the random phase approximation. In section 6.6, we calculate the spectrum of acoustic phonon dispersion and decay and discuss the signatures for nodal nematicity in the resulting decay pattern in section 6.7.

## 6.2 Nodal nematic quantum criticality inside a d-wave superconductor

In this section we review the model for nematic order inside a d-wave superconductor as described in Ref.[93]. The nematic phase is one where the four-fold rotational symmetry of the crystal ($C_{4v}$) is broken to a two-fold symmetry ($C_{2v}$), while retaining translational symmetry. In a d-wave superconductor the superconducting order opens a gap in the quasiparticle excitation spectrum except at four nodal points. In a nematic d-wave superconductor, coupling to an Ising nematic order parameter ($\phi$) leads to the nodes shifting from their $C_{4v}$ symmetric locations to one that is $C_{2v}$ symmetric. The shift is by an amount that is proportional to $\langle\phi\rangle$.

The relevant degrees of freedom describing the low energy physics of the system are thus nodal fermions and the Ising nematic order parameter $\phi$. The effective Lagrangian describing the coupled system is $\mathcal{L} = \mathcal{L}_\psi + \mathcal{L}_\phi + \mathcal{L}_{\psi-\phi}$. $\mathcal{L}_\psi$ is the nodal quasiparticle Lagrangian in a $d_{x^2-y^2}$ superconductor obtained by linearizing the

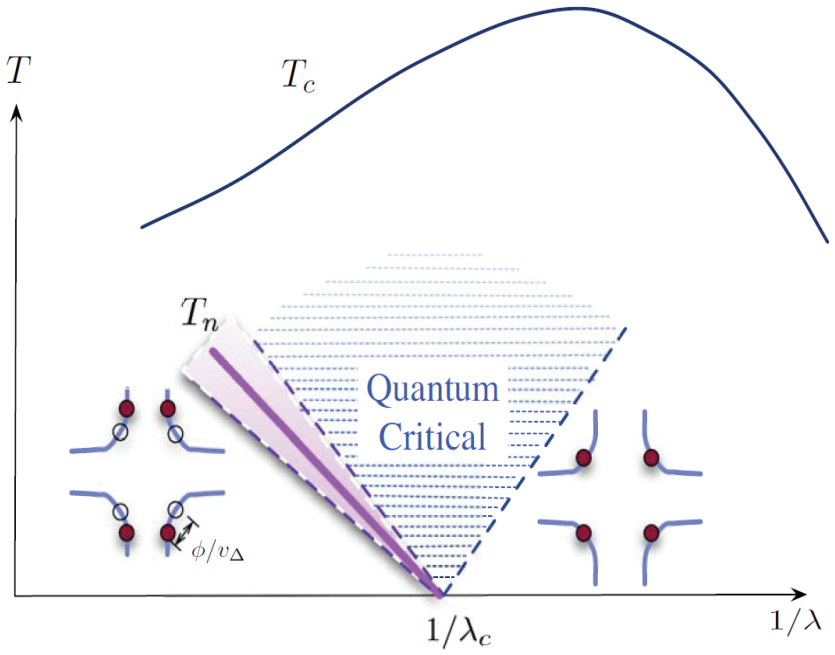


Figure 6.1: Schematic of nodal nematic quantum criticality (adapted from [92]). Quantum critical point at $\lambda = \lambda_c$, separating the nodal nematic phase for $\lambda^{-1} < \lambda_c^{-1}$ from the symmetric phase, and its quantum critical fan. $T_c$ and $T_n$ are the superconducting and nematic critical temperatures and the (purple) wedge corresponds to the thermal critical regime.

Bogoliubov-de Gennes Hamiltonian about the nodes.

$$\mathcal{L}_\psi = \sum_{n,\alpha} \overline{\psi}_{n,\alpha}(i\partial_t - i\tau_3 \vec{v}_F^n.\vec{\nabla} - i\tau_1 \vec{v}_\Delta^n.\vec{\nabla})\psi_{n,\alpha}. \tag{6.1}$$

Here,

$$\psi_{n,\alpha}(\vec{q}) = \begin{pmatrix} c_{\vec{K}_n+\vec{q},\alpha} \\ \epsilon_{\alpha\beta} c^\dagger_{-(\vec{K}_n+\vec{q}),\beta} \end{pmatrix} \tag{6.2}$$

are two component Nambu spinors representing the nodal quasiparticles. Conversion from the nodal quasiparticle representation $c_{\vec{k}}$ to the Nambu spinor representation results in only two inequivalent nodes located at $\vec{K}_1 = (K, K)$ and $\vec{K}_2 = (K, -K)$, represented by the node indices, $n = 1, 2$. $\epsilon_{\alpha\beta}$ is a totally antisym-

metric matrix inserted to allow $\psi$ to transform as a spinor under rotation, $\tau_1$ and $\tau_3$ are standard $2 \times 2$ Pauli matrices acting on the Nambu spinors. $v_F^n$ and $v_\Delta^n$ are the fermi and gap velocities which are in turn given by

$$\vec{v}_F^n = \vec{\nabla}_{\vec{k}} \epsilon_{\vec{k}}|_{\vec{k}=\vec{K}_n}; \vec{v}_\Delta^n = \vec{\nabla}_{\vec{k}} \Delta_{\vec{k}}|_{\vec{k}=\vec{K}_n} \tag{6.3}$$

Typically $v_F$ and $v_\Delta$ are very different $\frac{v_\Delta}{v_F} \approx 0.05 - 0.1$ and the effective Dirac fermion Lagrangian describing the low energy physics of the nodal fermions is not *Lorentz invariant*.

The Lagrangian for the nematic order parameter is

$$\mathcal{L}_\phi = \frac{1}{2}\left[(\partial_t \phi)^2 - (\nabla \phi)^2\right] - \frac{m^2}{2}\phi^2 - \frac{u}{4N}\phi^4 \tag{6.4}$$

The interaction term coupling the nodal fermions and the nematic order parameter is an additional s-wave term in the superconducting gap and is of the form

$$\mathcal{L}_{\psi-\phi} = -\frac{\lambda}{\sqrt{2N}} \sum_{n,\alpha} \phi \overline{\psi}_{n,\alpha} \tau_1 \psi_{n,\alpha} \tag{6.5}$$

In Ref.[93], the behavior of this model is studied in the large $N$ limit, with $N = 2$ corresponding to the physical case of two spin states. The model is analyzed by evaluating the effective theory of the nematic order parameter by integrating out the nodal fermions using the random phase approximation (RPA). This results in a negative correction to the mass of the nematic field and hence a quantum critical point at finite coupling $\lambda = \lambda_c$. Above this critical coupling $\lambda_c$, the nematic order parameter acquires an expectation value

$$m^2 \langle \phi \rangle = -\frac{\lambda}{\sqrt{2N}} \sum_{n,\alpha} \left\langle \overline{\psi}_{n,\alpha} \tau_1 \psi_{n,\alpha} \right\rangle \tag{6.6}$$

$$\propto (\lambda - \lambda_c)^{\frac{1}{2}} \tag{6.7}$$

## 6.3 Model: Elastic theory coupled to nematic d-wave superconductor

We now describe the model for long wavelength acoustic phonons coupled to nodal quasiparticles in a $C_{4v}$ symmetric d-wave superconductor or a nematic ($C_{2v}$ symmetric) d-wave superconductor.

The model Lagrangian we consider is $\mathcal{L} = \mathcal{L}_{\vec{u}} + \mathcal{L}_{\vec{u}-\psi} + \mathcal{L}_{\psi} + \mathcal{L}_{\vec{u}-\phi}$ where $\mathcal{L}_{\vec{u}}$ accounts for free in-plane displacement fields $\vec{u}(\vec{r})$ within linearized elasticity, $\mathcal{L}_{\psi}$ the nodal quasiparticle Lagrangain introduced in the previous section, $\mathcal{L}_{\vec{u}-\psi}$ the coupling between the nodal quasiparticles and the displacement field, and $\mathcal{L}_{\vec{u}-\phi}$ the symmetry-allowed direct coupling between the nematic field and the elastic field of the lattice.

### 6.3.1 $C_{4v}$ symmetric linearized elastic theory

We describe the acoustic phonons associated with long wavelength distortions of the copper-oxide unit cell using a general elastic theory with the $C_{4v}$ point group symmetry. The Lagrangian for an elastic theory with $C_{4v}$ symmetry is

$$\mathcal{L}_{\vec{u}} = \frac{1}{2}\left[\rho \partial_t u_a \partial_t u_a - B(\epsilon_{xx} + \epsilon_{yy})^2 - \mu\left((\epsilon_{xx} - \epsilon_{yy})^2 + 4\epsilon_{xy}^2\right) - \kappa \epsilon_{xx}\epsilon_{yy}\right]$$

where the linearized strain $\epsilon_{ab}$ for $\{a, b\} = \{x, y\}$ is related to the displacement fields by[1]

$$\epsilon_{ab} = \frac{1}{2}(\partial_a u_b + \partial_b u_a). \tag{6.8}$$

In the above, $B$ and $\mu$ are the bulk and shear moduli for the general elastic theory in continuum and $\kappa$ is an additional bulk modulus present in a $C_{4v}$ symmetric

[1] Since we ignore the nonlinear terms in the strain, phonon decay within the model is only due to coupling to the electronic degrees of freedom

theory[2].

It is convenient to describe the displacements in the basis of the longitudinal and transverse phonon fields, $\vec{u}_{\vec{q}} = u^l_{\vec{q}}\hat{p}^{\parallel}_{\vec{q}} + u^t_{\vec{q}}\hat{p}^{\perp}_{\vec{q}}$, where $\hat{p}_{\parallel,\vec{q}} = \hat{q}$ and $\hat{p}_{\perp,\vec{q}} = R_{\frac{\pi}{2}}(\hat{q})$ are respectively the polarizations parallel and perpendicular to the direction of propagation. In this basis the Lagrangian for the linearized elastic theory becomes,

$$\mathcal{L}_{\vec{u}}(q) = \frac{1}{2}(u^l_{-q}u^t_{-q})\mathbf{K}(q)\begin{pmatrix} u^l_q \\ u^t_q \end{pmatrix} \tag{6.9}$$

where the kernel in the above expression is,

$$\mathbf{K}(q) = \begin{pmatrix} \rho\omega^2 - (B+\mu)|\vec{q}|^2 - \kappa\frac{q_x^2 q_y^2}{|\vec{q}|^2} & -\frac{\kappa}{2}\frac{q_x q_y}{|\vec{q}|^2}(q_x^2 - q_y^2) \\ -\frac{\kappa}{2}\frac{q_x q_y}{|\vec{q}|^2}(q_x^2 - q_y^2) & \rho\omega^2 - \mu|\vec{q}|^2 + \kappa\frac{q_x^2 q_y^2}{|\vec{q}|^2} \end{pmatrix} \tag{6.10}$$

As can be seen in the above equation, the additional elastic modulus $\kappa$ in a $C_{4v}$ symmetric theory result in off-diagonal terms that couple the longitudinal and transverse phonons.

### 6.3.2 Coupling between acoustic phonons and nodal quasiparticles

For the phonon-nodal quasiparticle coupling, we take the usual local Coulomb interaction between electron and ion densities. This when rewritten in the Nambu basis has the following form.

$$\mathcal{L}_{\vec{u}-\psi} = -\gamma\sum_n \overline{\psi}_{n,\alpha}\tau_3\psi_{n,\alpha}\nabla\cdot\vec{u}. \tag{6.11}$$

This form of the coupling is naturally $C_{4v}$ symmetric. The $\nabla\cdot\vec{u}$ term in the above is expected and is associated with a change in volume of the elastic medium and hence a change in the ion density. The form of the coupling implies that it is

[2]An isotropic theory has only two elastic constants, $B$ and $\mu$

only the longitudinal phonon that couples to the nodal quasiparticles. The decay of the transverse phonon within this model is a result of a non-zero $\kappa$ in the $C_{4v}$ symmetric elastic theory.

### 6.3.3 Coupling between the nematic and the elastic degrees of freedom

In addition to the coupling between the nodal quasiparticles and the phonons, we also include $C_{4v}$ symmetric terms coupling the nematic and elastic fields.[3]This term takes the form of an additional nematic order parameter dependent elastic modulus

$$\mathcal{L}_{\vec{u}-\phi} = +\theta\phi(\epsilon_{xx}^2 - \epsilon_{yy}^2) \tag{6.12}$$

which in the nematic phase results in a tetragonal-to-orthorhombic symmetry reduction of the elastic theory for the phonons. While allowed by $C_{4v}$ symmetry, the strength of this term depends on the microscopic nature of the electronic nematic degree of freedom. In the iron pnictides, the coupling between the emergent nematic degrees of freedom and the lattice is large [94], and the nematic phase is associated with an orthorhombic structural distortion. However, the strength of such a coupling in the cuprates is unknown.

[3]such a term is distinct from similar terms that arise resulting from an effective interaction between the nematic field and the elastic theory, mediated by the nodal fermions.

## 6.4 Effective theory: integrating out the nodal fermion field

We proceed by evaluating the effective theory for the phonons and the nematic order parameter field within the random phase approximation (RPA). This involves the evaluation of the Feynman diagrams shown in Fig.[6.2]. These diagrams result in the effective nodal fermion mediated coupling between the nematic order parameter (a)[4], between the nematic field and the acoustic phonons (b) and between the acoustic phonons (c). We discuss the effect of the latter, which results in an additional quadratic term in the elastic theory given by

$$\delta\mathcal{L}_{\vec{u}} = \Pi(\vec{q},\omega)(\vec{q}\cdot\vec{u}_q)^2 \tag{6.13}$$

where $\vec{u}_q$ is the Fourier component of the displacement field $\vec{u}(\vec{r})$ and $\Pi(\vec{q},\omega)$ is the RPA polarization which evaluates to[5] :

$$\Pi(\vec{k},\omega) = \frac{\gamma^2}{32 v_F v_\Delta}\Bigg[\sqrt{-\omega^2+E_1(\vec{k})^2}\left(1-\frac{v_F^2k_x^2}{-\omega^2+E_1(\vec{k})^2}\right) + \sqrt{-\omega^2+E_2(\vec{k})^2}\left(1-\frac{v_F^2k_y^2}{-\omega^2+E_2(\vec{k})^2}\right)\Bigg] \tag{6.14}$$

where $E_1(\vec{k})$ and $E_2(\vec{k})$ are two energy scales associated with a given momentum $\vec{k}$:

$$E_1(\vec{k}) \equiv \sqrt{v_F^2k_x^2+v_\Delta^2k_y^2}, E_2(\vec{k}) \equiv \sqrt{v_F^2k_y^2+v_\Delta^2k_x^2}. \tag{6.15}$$

These are the quasiparticle excitation energies of the *anisotropic* Dirac fermion Lagrangian describing the nodal fermions.

[4]The physical implications of this term are discussed in [93]

[5]Similar to the polarization in calculated in Ref.[93]. $v_F$ replaces $v_\Delta$ in the analogous expression since the interaction is in the particle-hole channel ($V_{\text{int}} \propto \tau_3$) instead of the particle-particle channel ($V_{\text{int}} \propto \tau_1$)

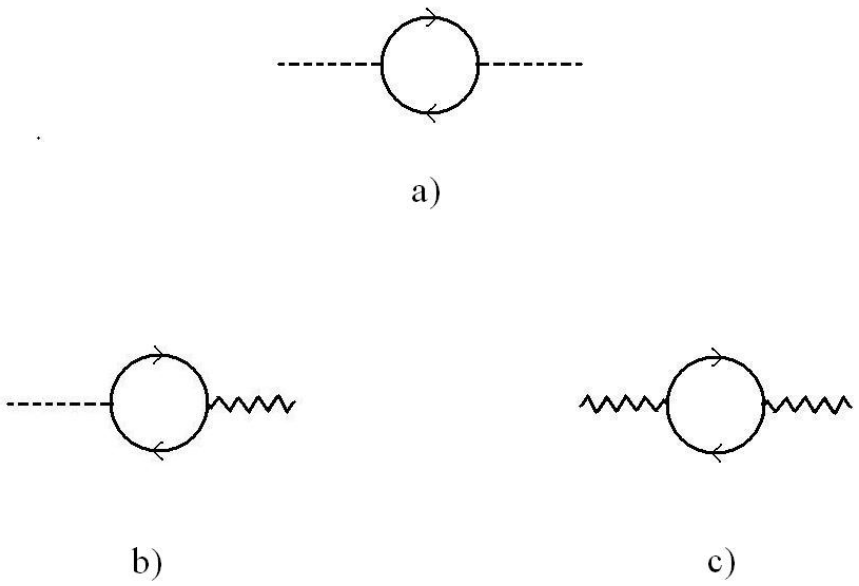


Figure 6.2: Diagrams evaluated to obtain the effective theory on *integrating out* nodal fermions. a) Coupling between the nematic order parameter field (dashed lines) mediated by nodal fermions b) nodal fermion mediated coupling between acoustic phonons (squiggly lines) and the nematic order parameter field. c) nodal fermion mediated coupling between acoustic phonons

## 6.5 Effective elastic theory

In order to find the effect of the nodal quasiparticles and the nematic order parameter on the elastic theory, we rewrite the quadratic effective Lagrangian in the basis of longitudinal and transverse displacements, which results in a modification of the bare kernel of the $C_{4v}$ symmetric elastic theory in Eqn.[6.10], into the form below :

$$\mathbf{K}(q) = \begin{pmatrix} \rho\omega^2 - (B+\mu - \Pi(q))|\vec{q}|^2 - \kappa\frac{q_x^2 q_y^2}{|\vec{q}|^2} + \theta\phi(q_x^2 - q_y^2) & -\frac{\kappa}{2}\frac{q_x q_y}{|\vec{q}|^2}(q_x^2 - q_y^2) - \theta\phi q_x q_y \\ -\frac{\kappa}{2}\frac{q_x q_y}{|\vec{q}|^2}(q_x^2 - q_y^2) - \theta\phi q_x q_y & \rho\omega^2 - \mu|\vec{q}|^2 + \kappa\frac{q_x^2 q_y^2}{|\vec{q}|^2} \end{pmatrix} \tag{6.16}$$

The nodal fermion mediated coupling results in a modification of the bulk modulus into one that is frequency and momentum dependent and of the form,

$$\tilde{B}(q,\omega) = B - \Pi(q,\omega) \tag{6.17}$$

The additional term in the modified kernel are $C_{2v}$ symmetric terms that are present in the nematic phase. To evaluate the modified phonon properties resulting from the coupling to the nematic d-wave superconductor, we first diagonalize the matrix $\mathbf{K}(q)$ in Eqn.[6.16] to find the new eigenvectors $\tilde{u}^l$ and $\tilde{u}^t$, which are each adiabatically connected to longitudinal and transverse modes of isotropic elastic theory. In this eigenbasis, the effective Lagrangian takes the following simple form:

$$\mathcal{L}_{\text{eff}} = \frac{1}{2}\left[(\omega^2 - \tilde{\omega}_l(\vec{q},\omega)^2)|\tilde{u}^l_q|^2 + (\omega^2 - \tilde{\omega}_t(\vec{q},\omega)^2)|\tilde{u}^t_q|^2\right]. \tag{6.18}$$

In the above expression the explicit functional form for the renormalized frequencies are as given below, with the subscript $l, t$ describing longitudinal or transverse phonons respectively.

$$\omega_\ell(q,\omega)^2 = \frac{1}{2}((\tilde{B}+2\mu)q^2 + \theta\phi(q_y^2 - q_x^2) + \sqrt{k^2 q_x^2 q_y^2 + (\tilde{B}^2 + \theta^2\phi^2)q^4 + 2\tilde{B}(2kq_x^2 q_y^2 + \theta\phi(q_y^4 - q_x^4))}) \tag{6.19}$$

$$\omega_t(q,\omega)^2 = \frac{1}{2}((\tilde{B}+2\mu)q^2 + \theta\phi(q_y^2 - q_x^2) - \sqrt{k^2 q_x^2 q_y^2 + (\tilde{B}^2 + \theta^2\phi^2)q^4 + 2\tilde{B}(2kq_x^2 q_y^2 + \theta\phi(q_y^4 - q_x^4))}) \tag{6.20}$$

## 6.6 Phonon dispersion and lifetime

In the absence of coupling to nodal quasiparticles, the longitudinal and transverse phonons do not decay within this model and the phonon propagators associated

with the Lagrangian in Eq.(6.18) have simple poles at $\omega = \pm\omega_l^0(\vec{q})$ and $\omega = \pm\omega_t^0(\vec{q})$ respectively, which define their bare dispersions. However, due to the scattering off of nodal quasiparticles encoded in the polarization $\Pi(q)$, $\tilde{\omega}_{\ell/t}(\vec{q},\omega)$ is a non-trivial function of $\vec{q}$ and takes on complex values.

To find the lifetime and dispersion renormalization, we need to solve for the poles of the propogator in the presence of the coupling, i.e., solve for $\omega^2 = \omega_{\ell/t}(\vec{q},\omega)^2$. In order to obtain an analytic solution, we expand in the coupling $\gamma^2$. When $\gamma^2 = 0$, we simply obtain $\omega = \pm\omega^0(\vec{q})$. We let $\omega = \pm\omega_{l/t}^0(\vec{q}) + \delta\varepsilon_{l/t}^{\pm} + i\gamma_{l/t}^{\pm}$ and solve for the dispersion renormalization $\delta\varepsilon_{l/t}^{\pm}(\vec{q})$ and the decay rate $\gamma_{l/t}^{\pm}(\vec{q})$ to first order in $\gamma^2$. This results in the following expressions,

$$\delta\varepsilon_{\ell/t}^{\pm} = \gamma^2 \mathrm{Re}\frac{\partial\omega_{\ell,t}}{\partial\gamma^2}\bigg|_{\omega=\pm\omega_{\ell/t}^0,\gamma^2=0}, \tag{6.21}$$

$$\gamma_{\ell/t}^{\pm} = \gamma^2 \mathrm{Im}\frac{\partial\omega_{\ell,t}}{\partial\gamma^2}\bigg|_{\omega=\pm\omega_{\ell/t}^0,\gamma^2=0} \tag{6.22}$$

As expected the decay rate is proportional to the $\mathrm{Im}[\tilde{\Pi}(\vec{q})]$[6] which explicitly evaluates to

$$\gamma_{\ell/t}(\vec{q}) = -\frac{\mathrm{Im}(\tilde{\Pi}(\vec{q},\omega_{\ell/t}^0(\vec{q})))}{2\omega_{\ell/t}^0(\vec{q})}\frac{1}{2}\Bigg(q^2 \pm \frac{Bq^4 + 2\kappa q_x^2 q_y^2 + \theta\phi(q_y^4 - q_x^4)}{\sqrt{\kappa^2 q_x^2 q_y^2 + (B^2+\theta^2\phi^2)q^4 + 4B\kappa q_x^2 q_y^2 + 2B\theta(q_y^4 - q_x^4)}}\Bigg) \tag{6.23}$$

In the limit of the elastic constants $\kappa = \theta = 0$, there is no coupling between the transverse phonon and nodal quasiparticles and the transverse phonon does not decay, as can also be seen in the expression above.

[6]The nodal fermion momenta are defined about an axis along the nodal directions. The coordinates used for the elastic theory are along the crystal axes. For the phonon decay calculation, the polarization is given by $\tilde{\Pi}(q_x,q_y,\omega) = \Pi(\frac{q_x-q_y}{\sqrt{2}},\frac{q_x+q_y}{\sqrt{2}},\omega)$

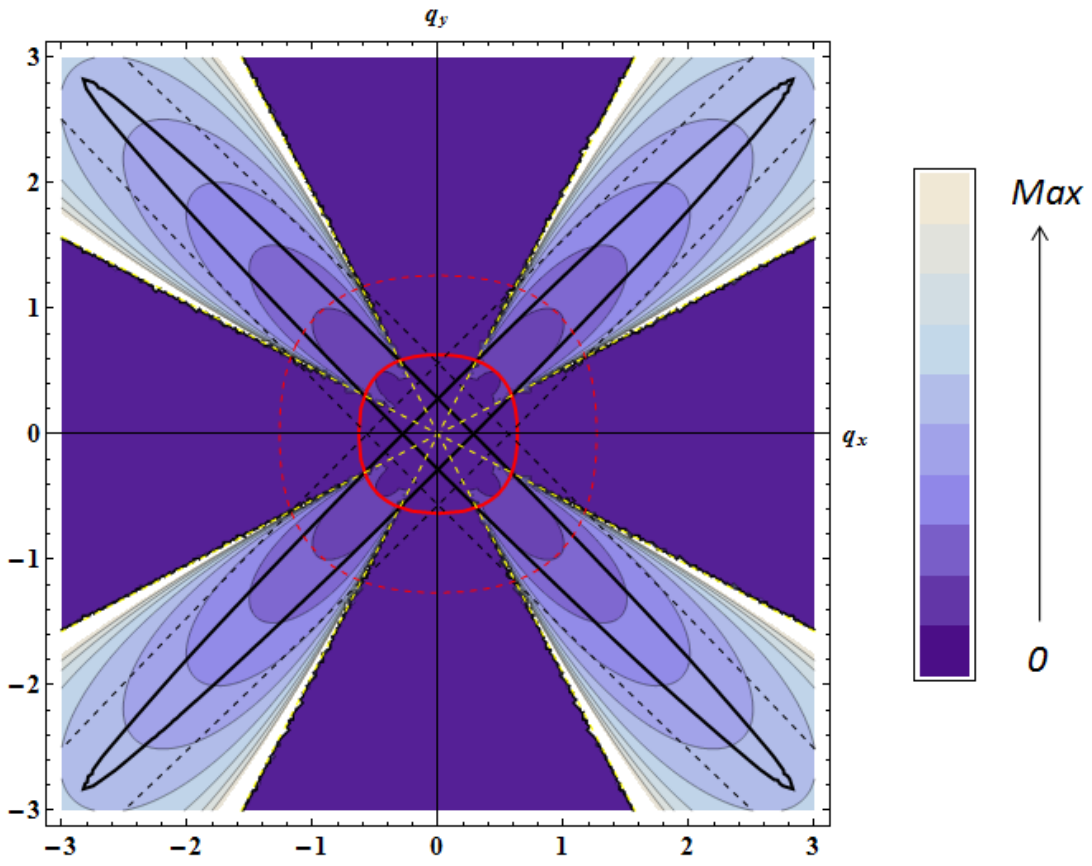


Figure 6.3: Contour plot of the imaginary part of the nodal fermion polarization bubble for the transverse phonon ($\mathrm{Im}\tilde{\Pi}(\vec{q}, \omega_t(\vec{q}))$). Black solid and dashed ellipses indicate contours of constant energy for nodal quasiparticles, while red solid and dashed curves indicate the contours of corresponding constant transverse phonon energy. The curves intersect on the dashed yellow lines, which indicate directions where the phonon energy equals the nodal fermion excitation energy. Phonon decay is maximal (singular) along these special directions. Toward the nodal directions, in the region bounded by the dashed yellow lines, the phonon can decay in into the nodal fermion continuum.

## 6.7 Acoustic phonon decay rate as a probe of nematic order

The coupling between the phonons and the nodal fermions leads to a non-trivial momentum dependent decay pattern for the acoustic phonons with a characteristic

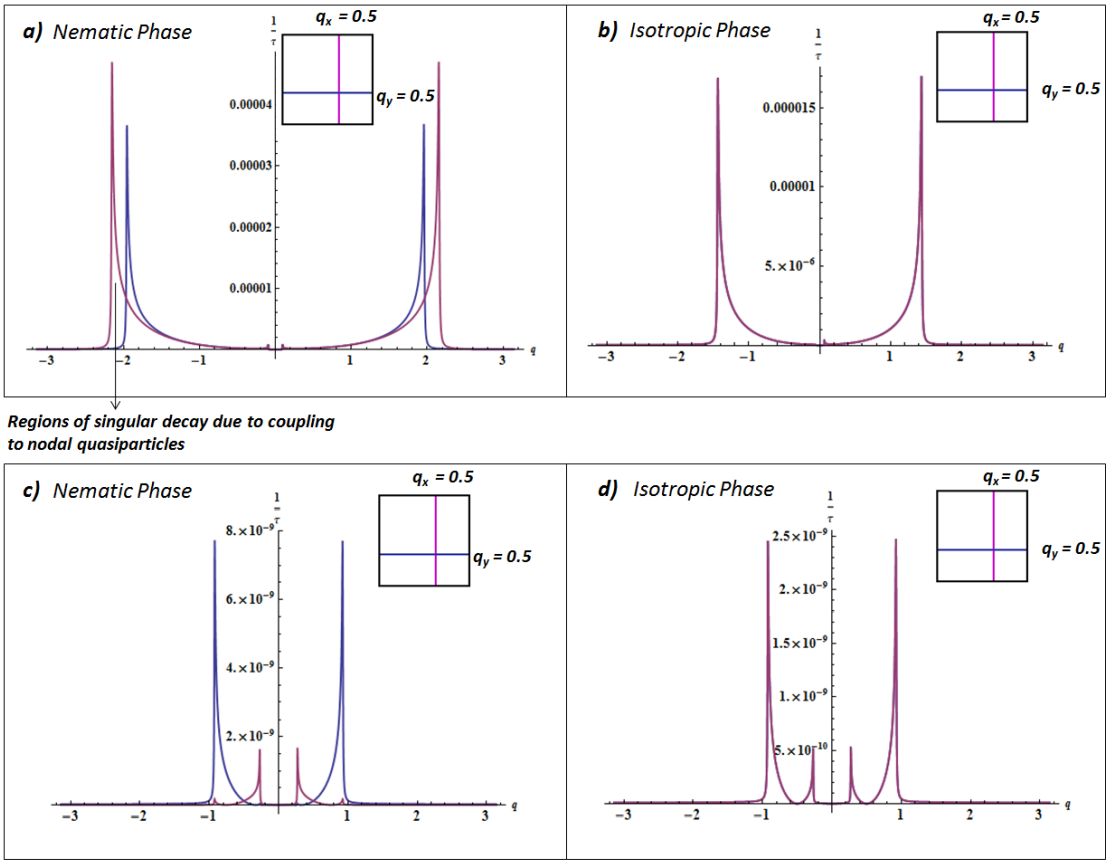


Figure 6.4: Line cuts of the decay rate of the longitudinal phonon along $\vec{q} = (0.5, 0)$ and $\vec{q} = (0, 0.5)$ inside a) the nematic phase and b) the isotropic phase. c) Line cuts of the decay rate of the transverse phonon along $\vec{q} = (0.5, 0)$ and $\vec{q} = (0, 0.5)$ inside the nematic phase and d) the isotropic phase. Regions of singular decay due to coupling to nodal fermions are indicated. Elastic constants are chosen such that $v_F > v_l > v_t > v_\Delta$, with the nematic order parameter induced elastic constant $\theta\phi = 0.05B$

*cross shaped pattern* of special directions along which there is a large decay rate. This pattern can be understood in terms of the dispersions of the phonons and nodal fermions. The nodal fermions have a highly anisotropic dispersion with contours of constant energy ($E_{1,2}(\vec{k}) = E_0$) being ellipses oriented along the two nodal directions (See Fig.[6.3]). In comparison the dispersion of the phonons is more isotropic. As a result, when the phonon velocity is between $v_\Delta$ and $v_F$, which is the case for the cuprates, there are special directions in momentum space along which the phonon energy is resonant with the nodal quasiparticles and where the phonon decay is singular. As we move away from these lines and toward the nodal directions, the nodal quasiparticles have lower energy than a phonon of the same wave vector resulting in phonon decay into the nodal quasiparticle continuum being energetically favored. As we go away from these lines and towards the crystal axis, scattering of phonons with nodal quasi particles is energetically disallowed and there is no phonon decay.[7]

Inside the nematic phase, coupling to the nematic order parameter breaks the $C_{4v}$ symmetry of the phonon dispersion. As a result, the pattern of phonon decay also becomes $C_{2v}$ symmetric. This can be seen by the difference in the decay pattern along $C_{4v}$ symmetry equivalent line cuts (Fig.[6.4a],[6.4c]). Inside the nematic phase, therefore, the pattern of acoustic phonon decay can be used as a *probe for nematic order*. This is of interest since acoustic phonon decay rates are now experimentally accessible through recent advancements in triple-axis spin-echo neutron scattering [95].

[7]The topology of this decay pattern remains the same as long as $v_\Delta < v_{ph} < v_F$. If on the other hand $v_\Delta < v_F < v_{ph}$, phonon decay through coupling to nodal quasiparticles would occur everywhere in the Brillouin zone.

# BIBLIOGRAPHY


[1] K. F. Y. Braginsky, V. B., *Quantum Measurements*. Cambridge University Press, 1995.

[2] C. Caves, "Quantum-mechanical radiation-pressure fluctuations in an interferometer," *Phys. Rev. Lett.*, vol. 45, pp. 75–79, Jul 1980.

[3] M. Aspelmeyer, T. J. Kippenberg, and F. Marquardt, "Cavity Optomechanics," Mar 2013.

[4] J. Chan, T. M. Alegre, A. H. Safavi-Naeini, J. T. Hill, A. Krause, S. Gröblacher, M. Aspelmeyer, and O. Painter, "Laser cooling of a nanomechanical oscillator into its quantum ground state," *Nature*, vol. 478, no. 7367, pp. 89–92, 2011.

[5] J. Teufel, T. Donner, D. Li, J. Harlow, M. Allman, K. Cicak, A. Sirois, J. Whittaker, K. Lehnert, and R. Simmonds, "Sideband cooling of micromechanical motion to the quantum ground state," *Nature*, vol. 475, no. 7356, pp. 359–363, 2011.

[6] A. D. OConnell, M. Hofheinz, M. Ansmann, R. C. Bialczak, M. Lenander, E. Lucero, M. Neeley, D. Sank, H. Wang, M. Weides, *et al.*, "Quantum ground state and single-phonon control of a mechanical resonator," *Nature*, vol. 464, no. 7289, pp. 697–703, 2010.

[7] W. H. Zurek, "Decoherence, einselection, and the quantum origins of the classical," *Reviews of Modern Physics*, vol. 75, no. 3, p. 715, 2003.

[8] S. Chakram, Y. S. Patil, L. Chang, and M. Vengalattore, "Dissipation in Ultrahigh Quality Factor SiN Membrane Resonators," *Phys. Rev. Lett.*, vol. 112, p. 127201, Mar 2014.

[9] B. M. Zwickl, W. E. Shanks, A. M. Jayich, C. Yang, A. C. Bleszynski Jayich, J. D. Thompson, and J. G. E. Harris, "High quality mechanical and optical properties of commercial silicon nitride membranes," *Applied Physics Letters*, vol. 92, no. 10, pp. –, 2008.

[10] J. Thompson, B. Zwickl, A. Jayich, F. Marquardt, S. Girvin, and J. Harris, "Strong dispersive coupling of a high-finesse cavity to a micromechanical membrane," *Nature*, vol. 452, no. 7183, pp. 72–75, 2008.

[11] I. Wilson-Rae, "Intrinsic dissipation in nanomechanical resonators due to phonon tunneling," *Phys. Rev. B*, vol. 77, p. 245418, Jun 2008.

[12] P. Rabl, A. Shnirman, and P. Zoller, "Generation of squeezed states of nanomechanical resonators by reservoir engineering," *Physical Review B*, vol. 70, no. 20, p. 205304, 2004.

[13] Y. Patil, S. Chakram, L. Chang, and M. Vengalattore, "Thermomechanical two-mode squeezing in an ultrahigh Q membrane resonator," *arXiv preprint arXiv:1410.7109*, 2014.

[14] F. Marquardt, J. P. Chen, A. A. Clerk, and S. M. Girvin, "Quantum Theory of Cavity-Assisted Sideband Cooling of Mechanical Motion," *Phys. Rev. Lett.*, vol. 99, p. 093902, Aug 2007.

[15] I. Wilson-Rae, N. Nooshi, W. Zwerger, and T. Kippenberg, "Theory of ground state cooling of a mechanical oscillator using dynamical backaction," *Physical Review Letters*, vol. 99, no. 9, p. 093901, 2007.

[16] S. S. Verbridge, J. M. Parpia, R. B. Reichenbach, L. M. Bellan, and H. G. Craighead, "High quality factor resonance at room temperature with nanostrings under high tensile stress," *Journal of Applied Physics*, vol. 99, no. 12, pp. –, 2006.

[17] D. J. Wilson, C. A. Regal, S. B. Papp, and H. J. Kimble, "Cavity Optomechanics with Stoichiometric SiN Films," *Phys. Rev. Lett.*, vol. 103, p. 207204, Nov 2009.

[18] D. J. Wilson, *Cavity optomechanics with high-stress silicon nitride films*. 2012.

[19] L. D. Landau and E. M. Lifshitz, *Course of Theoretical Physics Vol 7: Theory and Elasticity*. Pergamon Press, 1959.

[20] G. Anetsberger, O. Arcizet, Q. P. Unterreithmeier, R. Rivière, A. Schliesser, E. M. Weig, J. P. Kotthaus, and T. J. Kippenberg, "Near-field cavity optomechanics with nanomechanical oscillators," *Nature Physics*, vol. 5, no. 12, pp. 909–914, 2009.

[21] H. Seok, L. Buchmann, E. Wright, and P. Meystre, "Multimode strong-coupling quantum optomechanics," *Physical Review A*, vol. 88, no. 6, p. 063850, 2013.

[22] M. Bao, H. Yang, H. Yin, and Y. Sun, "Energy transfer model for squeeze-film air damping in low vacuum," *Journal of Micromechanics and Microengineering*, vol. 12, no. 3, p. 341, 2002.

[23] D. Southworth, R. Barton, S. Verbridge, B. Ilic, A. Fefferman, H. Craighead, and J. Parpia, "Stress and silicon nitride: A crack in the universal dissipation of glasses," *Physical review letters*, vol. 102, no. 22, p. 225503, 2009.

[24] I. Wilson-Rae, R. Barton, S. Verbridge, D. Southworth, B. Ilic, H. Craighead, and J. Parpia, "High-q nanomechanics via destructive interference of elastic waves," *Physical review letters*, vol. 106, no. 4, p. 047205, 2011.

[25] P.-L. Yu, T. P. Purdy, and C. A. Regal, "Control of Material Damping in High-Q Membrane Microresonators," *Phys. Rev. Lett.*, vol. 108, p. 083603, Feb 2012.

[26] S. Schmid, K. Jensen, K. Nielsen, and A. Boisen, "Damping mechanisms in high-q micro and nanomechanical string resonators," *Physical Review B*, vol. 84, no. 16, p. 165307, 2011.

[27] Q. P. Unterreithmeier, T. Faust, and J. P. Kotthaus, "Damping of nanomechanical resonators," *Physical review letters*, vol. 105, no. 2, p. 027205, 2010.

[28] C. Zener, "Internal Friction in Solids II. General Theory of Thermoelastic Internal Friction," *Phys. Rev.*, vol. 53, pp. 90–99, Jan 1938.

[29] R. Lifshitz and M. L. Roukes, "Thermoelastic damping in micro- and nanomechanical systems," *Phys. Rev. B*, vol. 61, pp. 5600–5609, Feb 2000.

[30] A. N. Norris and D. M. Photiadis, "Thermoelastic relaxation in elastic structures, with applications to thin plates," *The Quarterly Journal of Mechanics and Applied Mathematics*, vol. 58, no. 1, pp. 143–163, 2005.

[31] A. H. Nayfeh and M. I. Younis, "Modeling and simulations of thermoelastic damping in microplates," *Journal of Micromechanics and Microengineering*, vol. 14, no. 12, p. 1711, 2004.

[32] B. M. Zwickl, *Progress Toward Observation of Radiation Pressure Shot Noise*. 2011.

[33] A. Akhiezer *J. Phys. (Moscow)*, vol. 1, no. 277, 1939.

[34] K. Kunal and N. Aluru, "Akhiezer damping in nanostructures," *Physical Review B*, vol. 84, no. 24, p. 245450, 2011.

[35] S. Vengallatore *Private Communication*.

[36] J. Jäckle, "On the ultrasonic attenuation in glasses at low temperatures," *Zeitschrift für Physik*, vol. 257, no. 3, pp. 212–223, 1972.

[37] W. Phillips, "Two-level states in glasses," *Reports on Progress in Physics*, vol. 50, no. 12, p. 1657, 1987.

[38] A. Jöckel, M. T. Rakher, M. Korppi, S. Camerer, D. Hunger, M. Mader, and P. Treutlein, "Spectroscopy of mechanical dissipation in micro-mechanical membranes," *Applied Physics Letters*, vol. 99, no. 14, p. 143109, 2011.

[39] D. Tielbürger, R. Merz, R. Ehrenfels, and S. Hunklinger, "Thermally activated relaxation processes in vitreous silica: An investigation by Brillouin scattering at high pressures," *Phys. Rev. B*, vol. 45, pp. 2750–2760, Feb 1992.

[40] M. Cross and R. Lifshitz, "Elastic wave transmission at an abrupt junction in a thin plate with application to heat transport and vibrations in mesoscopic systems," *Physical Review B*, vol. 64, no. 8, p. 085324, 2001.

[41] D. M. Photiadis and J. A. Judge, "Attachment losses of high Q oscillators," *Applied Physics Letters*, vol. 85, no. 3, pp. 482–484, 2004.

[42] J. A. Judge, D. M. Photiadis, J. F. Vignola, B. H. Houston, and J. Jarzynski, "Attachment loss of micromechanical and nanomechanical resonators in the limits of thick and thin support structures," *Journal of Applied Physics*, vol. 101, no. 1, pp. –, 2007.

[43] Y.-H. Park and K. Park, "High-fidelity modeling of mems resonators. part i. anchor loss mechanisms through substrate," *Microelectromechanical Systems, Journal of*, vol. 13, no. 2, pp. 238–247, 2004.

[44] G. D. Cole, I. Wilson-Rae, K. Werbach, M. R. Vanner, and M. Aspelmeyer, "Phonon-tunnelling dissipation in mechanical resonators," *Nature communications*, vol. 2, p. 231, 2011.

[45] A. H. Safavi-Naeini and O. Painter, "Design of optomechanical cavities and waveguides on a simultaneous bandgap phononic-photonic crystal slab," *Optics express*, vol. 18, no. 14, pp. 14926–14943, 2010.

[46] P.-L. Yu, K. Cicak, N. Kampel, Y. Tsaturyan, T. Purdy, R. Simmonds, and C. Regal, "A phononic bandgap shield for high-q membrane microresonators," *Applied Physics Letters*, vol. 104, no. 2, p. 023510, 2014.

[47] M. Maldovan, "Sound and heat revolutions in phononics," *Nature*, vol. 503, no. 7475, pp. 209–217, 2013.

[48] T. P. Purdy, R. W. Peterson, and C. A. Regal, "Observation of Radiation Pressure Shot Noise on a Macroscopic Object," *Science*, vol. 339, no. 6121, pp. 801–804, 2013.

[49] Y. Tsaturyan, A. Barg, A. Simonsen, L. G. Villanueva, S. Schmid, A. Schliesser, and E. S. Polzik, "Demonstration of suppressed phonon tunneling losses in phononic bandgap shielded membrane resonators for high-q optomechanics," *Optics express*, vol. 22, no. 6, pp. 6810–6821, 2014.

[50] J. C. Sankey, C. Yang, B. M. Zwickl, A. M. Jayich, and J. G. Harris, "Strong and tunable nonlinear optomechanical coupling in a low-loss system," *Nature Physics*, vol. 6, no. 9, pp. 707–712, 2010.

[51] H. Tan, G. Li, and P. Meystre, "Dissipation-driven two-mode mechanical squeezed states in optomechanical systems," *Physical Review A*, vol. 87, no. 3, p. 033829, 2013.

[52] M. Woolley and A. Clerk, "Two-mode squeezed states in cavity optomechanics via engineering of a single reservoir," *arXiv preprint arXiv:1404.2672*, 2014.

[53] A. D. OConnell, M. Hofheinz, M. Ansmann, R. C. Bialczak, M. Lenander, E. Lucero, M. Neeley, D. Sank, H. Wang, M. Weides, *et al.*, "Quantum ground state and single-phonon control of a mechanical resonator," *Nature*, vol. 464, no. 7289, pp. 697–703, 2010.

[54] A. D. Armour, M. P. Blencowe, and K. C. Schwab, "Entanglement and Decoherence of a Micromechanical Resonator via Coupling to a Cooper-Pair Box," *Phys. Rev. Lett.*, vol. 88, p. 148301, Mar 2002.

[55] R. B. Karabalin, R. Lifshitz, M. C. Cross, M. H. Matheny, S. C. Masmanidis, and M. L. Roukes, "Signal Amplification by Sensitive Control of Bifurcation Topology," *Phys. Rev. Lett.*, vol. 106, p. 094102, Feb 2011.

[56] T. Faust, J. Rieger, M. Seitner, J. Kotthaus, and E. Weig, "Coherent control

of a classical nanomechanical two-level system," *Nature Physics*, vol. 9, no. 8, pp. 485–488, 2013.

[57] I. Mahboob, H. Okamoto, K. Onomitsu, and H. Yamaguchi, "Two-mode thermal-noise squeezing in an electromechanical resonator," *Phys. Rev. Lett.*, vol. 113, p. 167203, Oct 2014.

[58] R. Lifshitz and M. Cross, "Nonlinear dynamics of nanomechanical and micromechanical resonators," *Review of nonlinear dynamics and complexity*, vol. 1, pp. 1–52, 2008.

[59] D. W. Carr, S. Evoy, L. Sekaric, H. Craighead, and J. Parpia, "Parametric amplification in a torsional microresonator," *Applied Physics Letters*, vol. 77, no. 10, pp. 1545–1547, 2000.

[60] R. Baskaran and K. L. Turner, "Mechanical domain coupled mode parametric resonance and amplification in a torsional mode micro electro mechanical oscillator," *Journal of Micromechanics and Microengineering*, vol. 13, no. 5, p. 701, 2003.

[61] D. Rugar and P. Grütter, "Mechanical parametric amplification and thermomechanical noise squeezing," *Phys. Rev. Lett.*, vol. 67, pp. 699–702, Aug 1991.

[62] V. Natarajan, F. DiFilippo, and D. E. Pritchard, "Classical squeezing of an oscillator for subthermal noise operation," *Physical review letters*, vol. 74, no. 15, p. 2855, 1995.

[63] H. Okamoto, A. Gourgout, C.-Y. Chang, K. Onomitsu, I. Mahboob, E. Y. Chang, and H. Yamaguchi, "Coherent phonon manipulation in coupled mechanical resonators," *Nature Physics*, vol. 9, no. 8, pp. 480–484, 2013.

[64] E. Gavartin, P. Verlot, and T. J. Kippenberg, "Stabilization of a linear nanomechanical oscillator to its thermodynamic limit," *Nature communications*, vol. 4, 2013.

[65] L. Lugiato, C. Oldano, C. Fabre, E. Giacobino, and R. Horowicz, "Bistability, self-pulsing and chaos in optical parametric oscillators," *Il Nuovo Cimento D*, vol. 10, no. 8, pp. 959–977, 1988.

[66] L.-A. Wu, M. Xiao, and H. Kimble, "Squeezed states of light from an optical parametric oscillator," *JOSA B*, vol. 4, no. 10, pp. 1465–1475, 1987.

[67] Z. Ou, S. Pereira, H. Kimble, and K. Peng, "Realization of the Einstein-Podolsky-Rosen paradox for continuous variables," *Phys. Rev. Lett.*, vol. 68, pp. 3663–3666, Jun 1992.

[68] M. D. Reid and P. D. Drummond, "Quantum Correlations of Phase in Nondegenerate Parametric Oscillation," *Phys. Rev. Lett.*, vol. 60, pp. 2731–2733, Jun 1988.

[69] F. Hudelist, J. Kong, C. Liu, J. Jing, Z. Ou, and W. Zhang, "Quantum metrology with parametric amplifier-based photon correlation interferometers," *Nature communications*, vol. 5, 2014.

[70] A. Szorkovszky, A. A. Clerk, A. C. Doherty, and W. P. Bowen, "Mechanical entanglement via detuned parametric amplification," *arXiv preprint arXiv:1402.6392*, 2014.

[71] A. Szorkovszky, A. A. Clerk, A. C. Doherty, and W. P. Bowen, "Detuned mechanical parametric amplification as a quantum non-demolition measurement," *New Journal of Physics*, vol. 16, no. 4, p. 043023, 2014.

[72] M. J. Woolley and A. A. Clerk, "Two-mode back-action-evading measurements in cavity optomechanics," *Phys. Rev. A*, vol. 87, p. 063846, Jun 2013.

[73] C. M. Caves, K. S. Thorne, R. W. Drever, V. D. Sandberg, and M. Zimmermann, "On the measurement of a weak classical force coupled to a quantum-mechanical oscillator. i. issues of principle," *Reviews of Modern Physics*, vol. 52, no. 2, p. 341, 1980.

[74] M. Woolley, G. Milburn, and C. M. Caves, "Nonlinear quantum metrology using coupled nanomechanical resonators," *New Journal of Physics*, vol. 10, no. 12, p. 125018, 2008.

[75] J. Kong, Z. Ou, and W. Zhang, "Phase-measurement sensitivity beyond the standard quantum limit in an interferometer consisting of a parametric amplifier and a beam splitter," *Phys. Rev. A*, vol. 87, p. 023825, Feb 2013.

[76] A. Heidmann, R. Horowicz, S. Reynaud, E. Giacobino, C. Fabre, and G. Camy, "Observation of quantum noise reduction on twin laser beams," *Physical review letters*, vol. 59, no. 22, p. 2555, 1987.

[77] A. Szorkovszky, G. A. Brawley, A. C. Doherty, and W. P. Bowen, "Strong ther-

momechanical squeezing via weak measurement," *Phys. Rev. Lett.*, vol. 110, p. 184301, May 2013.

[78] I. Mahboob and H. Yamaguchi, "Piezoelectrically pumped parametric amplification and Q enhancement in an electromechanical oscillator," *Applied Physics Letters*, vol. 92, no. 17, p. 173109, 2008.

[79] J. Martinez-Linares and P. Garcia-Fernandez, "Non-classical properties of non-degenerate parametric amplifiers and oscillators with pump depletion and non-homogeneous losses using the wigner representation," *Journal of Modern Optics*, vol. 41, no. 1, pp. 67–88, 1994.

[80] C. Fabre, E. Giacobino, A. Heidmann, and S. Reynaud, "Noise characteristics of a non-degenerate optical parametric oscillator-application to quantum noise reduction," *Journal de Physique*, vol. 50, no. 10, pp. 1209–1225, 1989.

[81] J. P. Sethna, *Statistical mechanics: entropy, order parameters, and complexity*, vol. 14. Oxford University Press Oxford, 2006.

[82] I. Katz, A. Retzker, R. Straub, and R. Lifshitz, "Signatures for a classical to quantum transition of a driven nonlinear nanomechanical resonator," *Phys. Rev. Lett.*, vol. 99, p. 040404, Jul 2007.

[83] E. Fradkin, S. A. Kivelson, M. J. Lawler, J. P. Eisenstein, and A. P. Mackenzie, "Nematic fermi fluids in condensed matter physics," *arXiv preprint arXiv:0910.4166*, 2009.

[84] M. P. Lilly, K. B. Cooper, J. P. Eisenstein, L. N. Pfeiffer, and K. W. West, "Evidence for an Anisotropic State of Two-Dimensional Electrons in High Landau Levels," *Phys. Rev. Lett.*, vol. 82, pp. 394–397, Jan 1999.

[85] R. A. Borzi, S. A. Grigera, J. Farrell, R. S. Perry, S. J. S. Lister, S. L. Lee, D. A. Tennant, Y. Maeno, and A. P. Mackenzie, "Formation of a Nematic Fluid at High Fields in $Sr_3Ru_2O_7$," *Science*, vol. 315, no. 5809, pp. 214–217, 2007.

[86] J.-H. Chu, H.-H. Kuo, J. G. Analytis, and I. R. Fisher, "Divergent Nematic Susceptibility in an Iron Arsenide Superconductor," *Science*, vol. 337, no. 6095, pp. 710–712, 2012.

[87] T.-M. Chuang, M. P. Allan, J. Lee, Y. Xie, N. Ni, S. L. Budko, G. S. Boebinger, P. C. Canfield, and J. C. Davis, "Nematic Electronic Structure in the

Parent State of the Iron-Based Superconductor $Ca(Fe_{1-x}Co_x)_2As_2$," *Science*, vol. 327, no. 5962, pp. 181–184, 2010.

[88] Y. Ando, K. Segawa, S. Komiya, and A. N. Lavrov, "Electrical Resistivity Anisotropy from Self-Organized One Dimensionality in High-Temperature Superconductors," *Phys. Rev. Lett.*, vol. 88, p. 137005, Mar 2002.

[89] R. Daou, J. Chang, D. LeBoeuf, O. Cyr-Choiniere, F. Laliberté, N. Doiron-Leyraud, B. Ramshaw, R. Liang, D. Bonn, W. Hardy, *et al.*, "Broken rotational symmetry in the pseudogap phase of a high-tc superconductor," *Nature*, vol. 463, no. 7280, pp. 519–522, 2010.

[90] V. Hinkov, D. Haug, B. Fauqu, P. Bourges, Y. Sidis, A. Ivanov, C. Bernhard, C. T. Lin, and B. Keimer, "Electronic Liquid Crystal State in the High-Temperature Superconductor $YBa_2Cu_3O_{6.45}$," *Science*, vol. 319, no. 5863, pp. 597–600, 2008.

[91] M. Lawler, K. Fujita, J. Lee, A. Schmidt, K. Y., C. K. Kim, H. Eisaki, S. Uchida, J. C. Davis, J. P. Sethna, and E.-A. Kim, "Intra-unit-cell electronic nematicity of the high-Tc copper-oxide pseudogap states," *Nature*, vol. 466, no. 7304, pp. 347–351, 2010.

[92] A. Mesaros, K. Fujita, H. Eisaki, S. Uchida, J. C. Davis, S. Sachdev, J. Zaanen, M. J. Lawler, and E.-A. Kim, "Topological Defects Coupling Smectic Modulations to IntraUnit-Cell Nematicity in Cuprates," *Science*, vol. 333, no. 6041, pp. 426–430, 2011.

[93] E.-A. Kim, M. J. Lawler, P. Oreto, S. Sachdev, E. Fradkin, and S. A. Kivelson, "Theory of the nodal nematic quantum phase transition in superconductors," *Phys. Rev. B*, vol. 77, p. 184514, May 2008.

[94] R. M. Fernandes, L. H. VanBebber, S. Bhattacharya, P. Chandra, V. Keppens, D. Mandrus, M. A. McGuire, B. C. Sales, A. S. Sefat, and J. Schmalian, "Effects of Nematic Fluctuations on the Elastic Properties of Iron Arsenide Superconductors," *Phys. Rev. Lett.*, vol. 105, p. 157003, Oct 2010.

[95] P. Aynajian, T. Keller, L. Boeri, S. M. Shapiro, K. Habicht, and B. Keimer, "Energy gaps and Kohn anomalies in elemental superconductors," *Science*, vol. 319, no. 5869, pp. 1509–1512, 2008.